Electromagnetic Non Destructive Evaluation and Inverse Problems

Flavio Calvano

Dipartimento di Ingegneria Elettrica

Università di Napoli "Federico II"

Tutors:

prof Guglielmo Rubinacci

prof Antonello Tamburrino

A thesis submitted for the degree of

Doctorate in Electrical Engineering

December 2010

Abstract

This thesis is focused on Eddy Current Testing (ECT), a technique for the Non Destructive Testing of conductive materials. In particular we study the quantitative imaging (inverse problem) of defects in conductive materials. By quantitative imaging we means imaging methods based on numerical models of the interaction between the probe and the defect(s). The imaging methods attempt to provide an image of the defect at variance of commercial instruments that, generally, detect the defect and may have limited capabilities of extracting its major sizes by means of calibration curves obtained in predefined conditions. In addition, numerical models of the probe-defect interaction (direct problem) play a relevant role for the computer aided design of the probe, where commercial codes typically fail to treat this kind of problems. In this thesis we present methods for the solution of both the direct and the inverse problems in ECT. The methods have been developed ad-hoc for ECT and have been optimized for accuracy and speed in view of real-time applications.

The thesis is organized as follow. In **Chapter 1** the main techniques in Non Destructive Testing are presented. In **Chapter 2** two numerical formulations to solve the electromagnetic direct problem of the interaction probe-defect are illustrated. The first exploits for the first time the differential geometry to solve this kind of numerical problems, and the second is based on an efficient integral formulation. In **Chapter 3** a topology based iterative imaging method to reconstruct the shape of inclusions with ECT data is illustrated. Its performances are compared with a genetic algorithm and an extensive experimental validation is presented. In **Chapter 4** a non-iterative imaging method based on monotonicity property of the measured impedance matrix (Monotonicity imaging method) is presented and its performances are compared with other two methods (Factorization

method and MUSIC method) which represent the State-of-the-Art of the non-iterative methods. In **Chapter 5** the first experimental validation of the Monotonicity imaging method is presented. We show that with a designed measurement system the algorithm is able reconstruct in real time the conductivity profile of Printed Circuits Boards (PCB). Finally the **Conclusions** are drawn.

To my parents, Pasquale and Rosa,
to my brothers Gennaro and Ciro.

Acknowledgements

I would like to acknowledge my tutors prof Guglielmo Rubinacci of University of Naples "Federico II" and prof Antonello Tamburrino of University of Cassino for their precious teachings, spreading from numerical electromagnetism to advanced mathematics and inverse problems.
I would like to acknowledge prof Salvatore Ventre of University of Cassino for all his precious teachings in the development of numerical codes.
I would like to thank prof Lauri Kettunen and prof Saku Suuriniemi of Tampere University of Technology (Finland) for the hospitality and the precious teachings they gave to me on differential geometry applied to electromagnetism during my study period of ten months in their department.
Special thanks go to my colleagues Teresa Bellizio and Carlo Forestiere. During the doctoral studies we really supported with one another every day.

Contents

List of Figures

LIST OF FIGURES

List of Tables

LIST OF TABLES

1

Introduction

1.1 Non Destructive Testing

NON-DESTRUCTIVE TESTING is a group of techniques aimed to investigate the materials properties without causing the damage. In the last years the main industries have invested a lot in non-destructive testing to guarantee for their products:

- high quality;
- high reliability;
- economical competitiveness.

In order to be competitive, the industries have to produce high quality and reliability products to protect against eventual defects that can compromise both the performances and the properties of the products. In this scenery Non destructive Testing (NDT) is very important to guarantee the reliability of a product without causing the damage during the testing. NDT techniques are used a lot when a continuous testing of the process cycle is required specially in those engineering fields as nuclear fusion, petrochemical , aeronautical applications where the quality product check is very important for the people security. The NDT techniques can be applied to both conductive and non conductive materials and several way to execute the test can be adopted. A first classification of the NDT experiments is based on the subdivision in active and passive tests. The active techniques are based on an increasing in the system energy if a defect is present in the device. The methods based on eddy current, ultrasounds and

X-ray, belong to this category. On the other hand the passive techniques reveal the presence of a defect evaluating the reaction of the device under test to some external agent. Liquid penetrant and magnetic particles methods belong to passive category. Another classification is the subdivision of the tests in surface and volumetric. The surface techniques are adapt to reveal surface defects localised near the surface interested by the analysis. The methods belonging to this category are the liquid penetrant and the eddy current inspection that is able to reveal also the sub-surface defect, but there are limits related to the penetration depth that is the main difference with the volumetric methods like ultrasonic and X-ray which are able to detect deeper defects.

1.1.1 Applications of Non destructive Testing

In order to completely inspect an object it is important to combine more types of non destructive testing techniques. The choosen inspection is strictly related to the applications:

- dimensions measurement. It regularly obtained with optical techniques, ultrasounds and eddy current specially to measure the thickness of the metals or dialectic covering thickness on metal substrate;

- material properties measurement. It reveals the material properties as the impurity content, elasticity, permeability, conductivity etc. The electric conductivity measurement is particular adapt to be measured with eddy current testing, while the magnetic properties are measured with magnetic particles inspection;

- internal defects analysis. The most common analysis field in non destructive evaluation is the internal defect analysis. The X-ray methods are particularly adapt to this end because they can provide an high resolution image of the region internal by respect the defect. The main drawback are the difficulties to execute the test and the dangers related to the exposition to the X-rays. In the last years new techniques less dangerous than the X-rays have been developed. Among these methods it is worth mentioning the ultrasonic methods, which are particularly adapt to locate the defect position;

- surface defects analysis. The surface defects analysis is obtained with penetrant liquid technique or with the electromagnetic particles technique. The first method

is not very good in sub-surface defect evaluation while the second one is used specially to evaluate the depth of the surface cracks in the metals, but they can be used only in magnetic materials and they require the application of an high magnetic field. For the metals the eddy current inspection is particularly adapt to reveal surface and sub-surface defects.

In the following the main methods used in Non Destructive Testing are illustrated.

1.1.2 Liquid penetrant inspection (LPI)

This non destructive technique exploits the property of some liquids to penetrate in surface defects thanks to their capillary action (low surface tension fluid penetrates into clean and dry surface-breaking discontinuities). When an adequate penetration time has been allowed, the excess penetrant is removed by water and a developer is applied. The developer helps to draw penetrant out of the flaw where a visible indication becomes visible to the inspector. The defect is then revealed by directly observing the device and the contrast between the penetrant and the developer (see Fig.1.1). The liquid

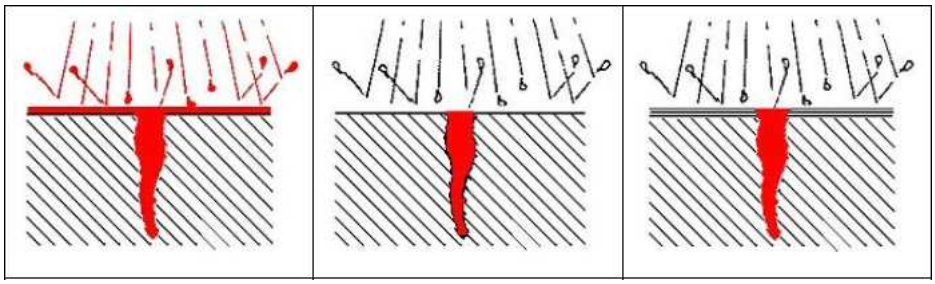

Figure 1.1: Liquid penetrant inspection.

penetrant inspection is adapt to reveal surface discontinuities in all the materials. It can be applied on each component of a device without taking into account the geometry and the material types. The main advantages of this technique are:

- It can be applied in all the materials;
- It is easy to perform the analysis and to analyze the results;
- It can be applied on components on which it can be difficult to access;
- It can be performed with a cost reduced by respect the available methods.

On the other hand the main drawbacks are:

- It reveals the surface inclusions;
- Materials different from the background are not revealed;
- The surface of the device under test has to be carefully prepared;

1.1.3 Magnetic particles inspection

The magnetic particles inspection is adapt to localise surface and sub-surface discontinuities in ferromagnetic materials. The test is based deviation of the magnetic field lines in presence of a discontinuity. In order to reveal the presence of a defect, magnetic particles of ferromagnetic materials are posed on the surface of the device under test, so that the trace of the anomaly profile is obtained. To efficiently perform the magnetic particles inspection it is important that the defect is not aligned with the force lines of the magnetic field; for this reason the device has to be magnetised in two orthogonal directions (see Fig.1.2). The main advantages of this technique are:

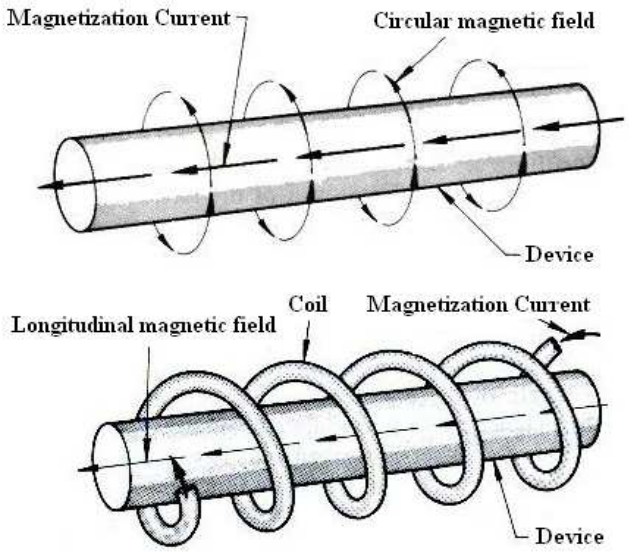

Figure 1.2: Device under test. Circular magnetization (top), longitudinal magnetization (bottom)

- It is a simple procedure;

- It is automatic;
- It can be very sensitive;
- The results analysis is simple.

On the other hand the main drawbacks are:

- It has to be performed on ferromagnetic materials;
- The test can be done on limited areas of the device;
- The demagnetization can be very difficult when low levels of residual magnetization are required.

1.1.4 Ultrasounds inspection

Ultrasounds inspection is a non-destructive testing method based on high frequency sound waves introduced in the device under test to reveal surface or internal defects, to reconstruct the shape and the position of the anomalies and finally to measure materials thickness. The ultrasounds inspection exploits the acoustic wave transmission in a material, evaluating the differences between the transmitted signal and the received signal. When a defect is present inside the device under test, the acoustic wave is deviated or reflected and this phenomena is revealed through the presence of additional peaks on the received signal (see Fig.1.3). The amplitude and the position of the peaks constitutes an indication of the type, the shape and the position of the defect inside the device under test.

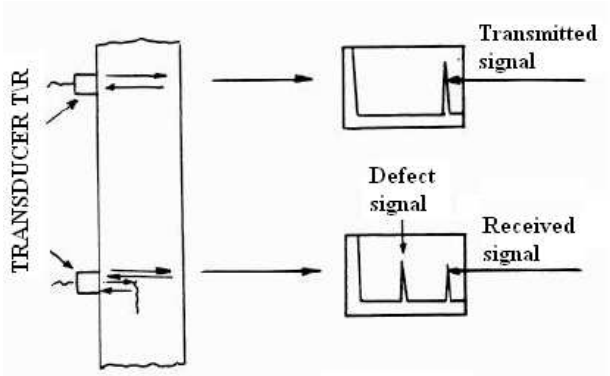

Figure 1.3: Ultrasounds inspection

The main advantages of the ultrasounds inspection are:

- It is a simple procedure;

On the other hand the main drawbacks are:

- It is difficult to test objects with a difficult geometry;
- It is difficult to test devices with an high acoustic attenuation;
- It is difficult to analyze the results.

1.1.5 X-ray inspection

This technique is based on the high frequency (and high energy) electromagnetic radiations properties. When an X-ray passes through the device under test, it is absorbed

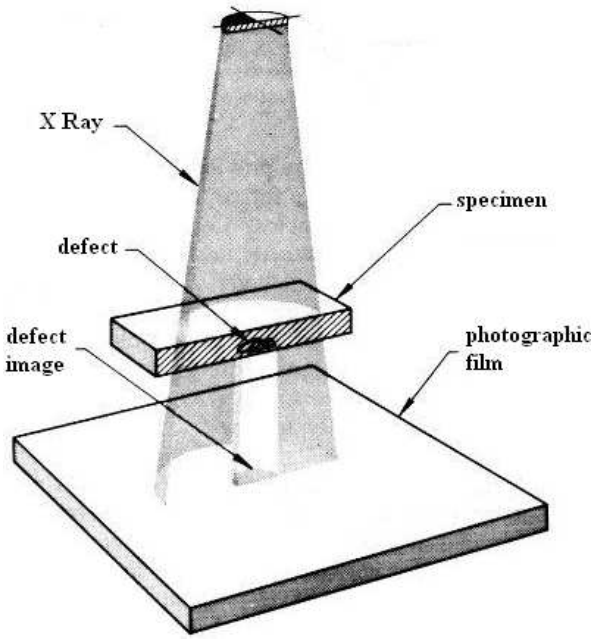

Figure 1.4: X-ray inspection

with an exponential law which is a function of the thickness and the material density. A photographic image of the X-ray after its passage through the device is an indication of the thickness, the density, material composition, whose variations are evaluated by the density image variation, usually using a grey scale for the image (see Fig.1.4). The main advantages of the X-ray inspection are:

- It is easy to perform the test;
- By the microfocus technique it is possible to magnify the defect area;

On the other hand the main drawbacks are:

- The maximum defect thickness is 400-500 mm;
- The defects with crack plane not aligned with the irradiation cone, cannot be revealed;
- It is necessary to keep the X-ray radiation in the maximum level prescribed by the normative;
- The testing devices are not portable.

1.1.6 Eddy Current Testing

Eddy Current Testing (ECT) is based on the detection of the reaction magnetic field produced by the eddy currents induced in the specimen under test by a driving coil passed by a sinusoidal current (see Fig.1.5). The presence of a defect disturbs the flow

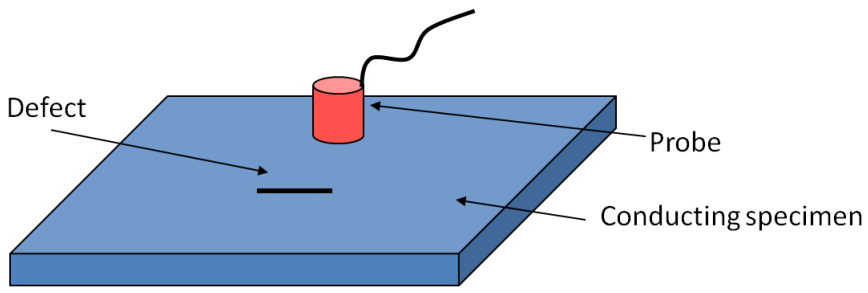

Figure 1.5: Eddy Current Testing

of the eddy currents, thus producing a magnetic field perturbation that depends on the position and shape of the defect and reflects in an impedance variation of the coil. By the impedance variation it is possible to determinate the amplitude and phase of the eddy current which depends on the material conductivity and permeability, and by the position and the shape of a defect inside the device under test. In presence of a defect the eddy currents deviate and this translates in an increasing of the amplitude and phase of the coil impedance variation.

The penetration depth is a critical parameter for this method. In order to detect internal defect it is mandatory to use low frequency signals with an high penetration depth (usually 1kHz), because the eddy current pattern has to extent inside the device under test. Anyway it is difficult to apply this technique to deep defect because the coil impedance variation decreases with the frequency and there is a trade-off between the penetration depth and the signal quality in the receptive coils. On the other hand the eddy current inspection is particularly adapt to reveal surface and sub-surface defect (penetration depth of few millimetres) by using an excitation frequency from 10kHz to 1MHz with an good enough impedance variation signal. The main advantages of the Eddy Current inspection are:

- High sensitivity of the test;
- High affidability;
- Complex geometries can be analyzed;
- The test is fast;
- The test has a low cost, the testing devices are portable;

On the other hand the main drawbacks are:

- The method can be applied only on metals with surface or sub-surface defects;
- The results analysis requires experience.

In the last years the optimization and modelling techniques improvement has given rise to an automation and a executing time reduction, so that the errors are reduced in the Non Destructive Testing. The testing automation process is based on the envelope of automatic procedures for the complete testing of a component and for the analysis of the type and characteristics of the revealed defect. For this last aspect it is used to apply the following methods:

- Signal analysis: the signals obtained in the non destructive analysis of the component are compared with the ones obtained in laboratory from artificial defect of known shape;

- Numerical model: the experimental signals are compared with the ones obtained with a numerical code based on the finite element method. Moreover inversion algorithms which minimise the errors between the numerical and the experimental signals can be applied to find the position and the exact shape of the defect.

Among the presented NDT methods, we choose to focus this thesis on the eddy current testing. As we explained eddy current testing can detect very small cracks and physically complex geometries can be investigated. It is also useful for the electrical conductivity and thickness measurements. The testing devices are portable, provide immediate feedback, and do not need to contact the device under test. So this technique is particular adapt to study several classes of problems from both the experimental and numerical point of view. In particular we show the development of numerical codes to simulate the eddy current testing, experimental activities coupled with inversion algorithms to recovery the shape of a defect or the conductivity profile of the analyzed devices.

1.1.7 Numerical methods for Eddy Current Testing

Eddy Current Testing constitutes an essential technique for the electromagnetic non-destructive testing of defects in conductive materials. Main applications are found in the inspection of aircraft, nuclear power plants, and other engineering constructions. In recent years numerical methods to simulate the experiments have been developed. This numerical interest is mainly due to the design of the experimental setup and is related to the development of new inversion algorithms to reconstruct the profile and the position of a defect. From a general point of view, we recognize the direct and the inverse problems.

1.1.7.1 Direct problem

The direct problem consists of computing, usually by numerical methods, the measurements (the magnetic flux density in given space locations or the voltages induced in the pickup coils) for an assigned geometrical configuration and driving system (excitation field).

The electromagnetic model of the measurements can be described by the magneto-quasistatic form of the Maxwell equations. We consider the situation described in

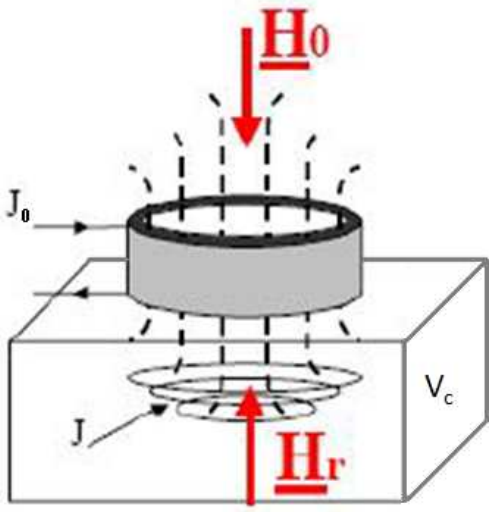

Figure 1.6: Coil above a plate. The source magnetic field H_0 induces in the conductive region V_c the eddy current density J which is the source of the reaction magnetic field H_r.

Fig.1.6 with an imposed current density $\mathbf{J_0}$ in a coil in $\mathbb{R}^3 \backslash V_c$, where V_c is a conductive material (see Fig.1.6). The mathematical model for the conductive region V_c is given by the equations:

$$\nabla \times \mathbf{E} = -\frac{\partial \mathbf{B}}{\partial t} \; in \; V_c \tag{1.1}$$

$$\nabla \times \mathbf{H} = \mathbf{J} \; in \; V_c \tag{1.2}$$

$$\mathbf{B} = \mu_0 \mathbf{H} \; in \; V_c \tag{1.3}$$

$$\mathbf{J} = \sigma \mathbf{E} \; in \; V_c \tag{1.4}$$

$$\nabla \cdot \mathbf{B} = 0 \; in \; V_c \tag{1.5}$$

and outside the conductive region:

$$\nabla \times \mathbf{H} = \mathbf{J_0} \; in \; \mathbb{R}^3 \backslash V_c \tag{1.6}$$

$$\nabla \cdot \mathbf{B} = 0 \; in \; \mathbb{R}^3 \backslash V_c \tag{1.7}$$

$$\mathbf{B} = \mu_0 \mathbf{H} \; in \; \mathbb{R}^3 \backslash V_c \tag{1.8}$$

where μ_0 is the permeability of the free space and σ is the conductivity of the

conductive volume V_c. In eddy current testing if a time variating current density $\mathbf{J_0}$ circulates in a coil, it is generated a time-variating magnetic field $\mathbf{H_0}$, which induces an electric field $\mathbf{E}$. Exploiting the Ohm law the current density $\mathbf{J}$ (eddy current density) is induced in the conductor, which generates a reaction magnetic field $\mathbf{H_r}$ (see Fig.1.6). The presence of an inclusion in the conductive material is equivalent to a variation in the conductivity $\Delta\sigma$ which causes a perturbation in the eddy current density and in the reaction magnetic field, that can be measured in terms of impedance variation in the receptive coil.

The direct problem consist of solving numerically this magneto-quasistatic model of the Maxwell equations. In recent years, numerical methods for solving the direct have been extensively studied. Several numerical formulations have been developed for modelling the effects of defects in a conductive material. The problem is challenging because of its intrinsically multiscale nature. Indeed, the eddy current density perturbation due to a defect is spatially localized, whereas the total eddy current density is circulating on a larger scale depending on the size of the probe. Commercial codes typically fail in solving this class of multiscale problems and, therefore, ad-hoc numerical formulation is mandatory. Numerical methods based on finite element formulations or the moment method have been applied to get a satisfactory accuracy and to reduce the computational cost. In this thesis we concentrate on finite element formulations both differential and integral.

We have implemented a differential formulation exploiting the differential geometry [1] to relax the multiscale nature of the direct problem and use the same finite element mesh for a class of problems.

On the other hand we have applied an integral formulation, developed in our research group for more than a decade, named CARIDDI_ECT [2, 3] to the computation of cracks on benchmarks related to the nuclear power industry [4] and compared its performances with another integral formulation, the CIVA code [5], and the experimental data.

1.1.7.2 Inverse problem

The inverse problem aims to find the position and the shape of a defect on the basis of the measurements obtained for a given excitation field. As each inverse problem it is non-linear and ill-posed. Strong difficulties arise since the possible presence of

local minima requires global optimization procedures, such as simulating annealing or genetic algorithms that work efficiently only with a limited number of unknowns. In this thesis we exploit both the iterative and non-iterative methods. In the iterative algorithms the strategy for estimating the shape of the defect is that the imaging algorithm "adapt" and improve iteratively its best estimate of the defect. To have a system that, in perspective, can be used for practical applications, it is fundamental that the imaging algorithm requires few steps only to find the estimate. To this aim we implemented an iterative topology based inversion algorithm [6] which has better performances by respect the genetic algorithm [7]. The problem which cannot be solved for the iterative methods is the high computation time due to the iterative cycles. We implemented and improved a fast non iterative inversion algorithm developed in our research group, the Monotonicity imaging method [8], and compared it with the other two methods available in literature, the Factorization method [9] and MUSIC method [10] in terms of reconstructions quality and computational cost. These three methods are the State-of-the-art of the non iterative methods. As very interesting results we got that Monotonicity imaging method works fine by respect the other two methods and can be applied to more than two phases conductivity materials [11, 12, 13]. Finally we performed for the first time an experimental validation of the Monotonicity imaging method in the frame of the Eddy Current Tomography, applying the method to reconstruct the conductivity profile of Printed Circuits Boards (PCB). We got as the most interesting result of the work of this thesis that with a designed measurement system, the Monotonicity imaging method provides the conductivity profile of the device under test in real time with no errors [14]. This result can be the starting point for the development of real-time imaging methods in eddy current inverse problem.

2

Direct Electromagnetic Problem

2.1 Introduction

The determination of the eddy currents induced in conductive materials by a time varying applied magnetic field is based on the solution of the quasi-stationary Maxwell's equations. Several numerical formulations based on the finite element method have been proposed to overcome the well known difficulties related to this kind of this open boundary problem both differential and integral. Among the differential formulations we recall the H-Φ formulation proposed by Bossavit and Verite [15],the T-Ω formulation discussed by Carpenter [16], later by Brown [17] and Albanese and Rubinacci [18], the a-v formulation proposed by Biró [19]. The main advantage of the differential formulation is that the matrices of the solving system are sparse, and this is quite very important for the computational cost. The main drawback is the air meshing which implies the re-meshing of the system when the movement has to be simulated. The computation with re-meshing can be source of numerical noise on the field computation. These problems can be reduced with new techniques which exploit the differential geometry to simulate the movement [20]. We will show in the following section that the same concept can be applied to relax the multiscale nature of the eddy current problem which involves mesh generation of narrow cracks in a bigger domain [1].
In the frame of integral formulations we mention a method used in the high-frequency regime [22]. This is a thin-skin model valid for crack depths larger than four times the electromagnetic skin depth. Typical surface crack inspections as indeed fulfil this prerequisite. The second model,is based on an integral formulation [23]-[28] specifically

derived to deal with this kind of problem and numerically approximated by the method of moments. In this case, the unknowns are the equivalent sources consisting of volume current dipole distributions, usually approximated by piecewise constant vector pulse functions. These integral equations are based on the dyadic Green's function that requires to discretize only the region occupied by the flaw and, in addition, takes into account automatically the continuity conditions. The finite element integral formulation [2, 3] named CARIDDI_ECT is based on the scalar Green's function rather than dyadic one. This formulation exploits the superposition principle. Specifically, the effects due to the defect are evaluated by solving a small problem onto a local mesh in a neighbourhood of the defect, once the unperturbed problem has been solved either analytically or onto a larger mesh. The superposition is very helpful when many tentative solution of the direct problem need to be computed when for example we use an iterative inversion algorithm, as we will show in the following chapter. The main advantage of the integral approach is in the fact that only the conducting part of the domain must be discretized. The conductive structures are usually thin and meshing only the conductive is very attractive. Nevertheless, for the integral approach both the numerical solution time and memory requirements grow at least as the square of the number of unknowns involved. A number of the techniques have been used to increase the effectiveness of the integral formulation, including tools to improve the sparsity of the matrices and the parallel treatment of the inversion [37]-[38]. These new techniques based on parallel computing make the integral formulation computational cost at least comparable with the differential formulation one.

2.2 Differential geometry based method

A typical problem in non-destructive testing (NDT) is to specify the defect that generates a certain signal into a probe. This is an indirect problem –the geometry of the defect that causes the signal is not known– and consequently, a number of forward computations is required to sketch the defect. Moreover, finite element-type NDT computations are known to be rather sensitive to numerical errors and all this makes NDT problems burdensome. The dimensions of a defect depend on the metric chosen for a space. At first this may sound preposterous, as obviously the defect is what it is and cannot be changed by some modeling choice. This is indeed the case, but the issue is

how we as the modelers observe the defect. The change of metric is like viewing the defect through eyeglasses that magnify locally the view, making the defect appear large. This alleviates the FE-mesh generation problems caused by narrow defects. Moreover, the magnification can be made adjustable, and a family of defect widths can then be modeled with a single (topological) mesh. This reduces the errors sensitive to the mesh [20]. Practically, the change of eyeglasses in this sense is done by a transformation between different systems that reflect the choices of metric one makes. Pre-processors use hardwired Euclidean metric to measure distances of coordinates. Standard parameterizations assign coordinates to points such that their Euclidean coordinate distances equal the measured distances of the points [21]. Reparameterization changes the points' coordinate distances (as we cannot redefine the hardwired coordinate metric) and this induces a new metric into the space. The change of metric affects the constitutive laws' material parameters, whose numerical values depend on the particular metric. Another view to the matter: Each finite element stiffness matrix corresponds to some field problem. If one changes locally the metric, altering the numeric values of distances, one can counterbalance this by adjusting the material parameters such that the entries of the stiffness matrix remain the same.

2.2.1 Equivalence of boundary value problems

Forward NDT problems regarding the magnetic field and current density are electromagnetic boundary value problems (BVP). To pose an electromagnetic BVP, one needs to specify its domain and the constitutive equations, and impose Maxwell's equations and appropriate boundary values. Typically, a standard parameterization (here ξ-coordinates) is used to "start up" the modeling process, i.e. describe the domain by coordinates and determine the material parameters that are expressed in terms of an appropriate length unit. However, our aim is to formulate and solve the problem with a reparameterization (here x-coordinates), and therefore we pose another BVP in terms of the reparameterization, such that the BVP describes the same physics. The reparameterization does not change Maxwell's equations, because they are invariant under diffeomorphic changes of coordinates and independent of metrics. To derive the material parameters for the reparameterization, we require that the virtual works related to corresponding displacements match for corresponding fields, and the field expression of energy stored is independent of our choice of coordinate system [21]. The invariance of

the virtual work establishes a correspondence between the fields in different coordinate systems. If $\mathbf{E}_\xi$ denotes the electric field vector in the ξ-system and the change-of-coordinates map from the x-system is $h = \xi \circ x^{-1}$, then the virtual displacements are related by $\mathbf{d}\xi = J\mathbf{dx}$, where J is the *Jacobian matrix* of h. Then the invariance requirement $\mathbf{E}_\xi \cdot \mathbf{d}\xi \equiv \mathbf{E}_x \cdot \mathbf{dx}$ relates the electric field vector $\mathbf{E}_\xi$ to $\mathbf{E}_x$ by the formula

$$\mathbf{E}_\xi = J^{-T}\,\mathbf{E}_x, \tag{2.1}$$

The same transformation formula holds also for the magnetic field $\mathbf{H}$ which denotes the magnetic field intensity. Departure from a standard parameterization implies that the Euclidean distances between x-coordinates are no more the same as the measured distances between the points they label. If a corresponding virtual displacement now appears shorter than originally, the corresponding field vector appears stronger. The invariance of energy, together with the invariance of virtual work, establishes the correspondence of material parameters. If $D \subset \mathbb{R}^3$ is the domain of the BVP in the ξ-system, the invariance of the energy means that

$$\int_D \mathbf{E}_\xi \cdot\, \epsilon_\xi\, \mathbf{E}_\xi \, dv_\xi = \int_{h^{-1}(D)} \mathbf{E}_x \cdot\, \epsilon_x\, \mathbf{E}_x \, dv_x \tag{2.2}$$

holds for all field pairs $(\mathbf{E}_\xi, \mathbf{E}_x)$ satisfying (2.1).

The matrix ϵ_x in terms of matrices ϵ_ξ and J is

$$\epsilon_x = \det(J) J^{-1} \epsilon_\xi J^{-T}. \tag{2.3}$$

The permeability μ and the conductivity σ transform similarly [21]. Their inverses transform as

$$\nu_x = \mu_x^{-1} = \frac{J^T \nu_\xi J}{\det(J)}. \tag{2.4}$$

The above transformation rules indicate how to pose equivalent BVPs on different coordinate systems . If the FEM meshes of equivalent BVPs are related by the change of coordinates h, then equation (2.2) shows that the stiffness matrices for both systems are identical.

2.2.2 Transformations

In most NDT applications, the probe must be placed into the immediate vicinity of the defect in order to detect it reliably, and because the geometry of the probe is independent of the defect width, it is not practical to extend the transformation into the probe.

We shall consequently restrict the transformations into the immediate vicinity V of the defect. The domain V may be tessellated into subdomains, see Fig. 2.1, if practical [20]. The feasible transformations

- must not displace any points at the boundary of V, and
- be continuous and piecewise differentiable with piecewise differentiable inverse.

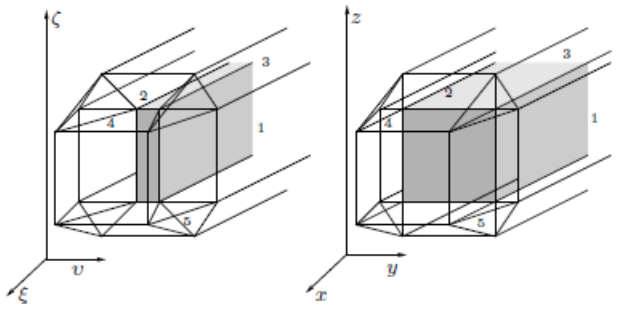

Figure 2.1: Defect (shaded) and its vicinity regions.

The Jacobians of the transformations must be reasonably well-behaved: their condition numbers and their determinants must not be extreme. We propose transformations to change the problem geometry (here defect width) and adjust the mesh to different penetration depths (frequency-dependent).

2.2.3 Problem geometry transformation

Let us now introduce transformations to modify the defect size. We can then treat a family of problems with the same mesh and ease the problems related to the mesh generation of narrow defects. The coordinates seen in the pre-processor are x, y, z, and the coordinates related to the original metric are ξ, υ, ζ. The original width of the defect is αw, and the transformation is produced by displacement of points of V in y-direction

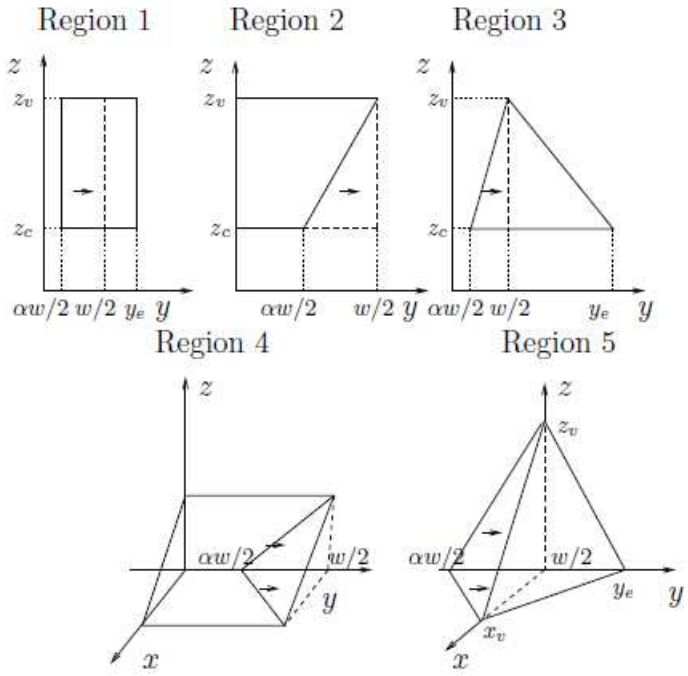

Figure 2.2: Regions 1 to 5.

only. We subdivide the box surrounding the defect into five different types of regions (see Fig. 2.1), where we apply the geometric transformations shown in Fig. 2.2.

We map piece-wise from x-positions to ξ-positions by $h = \xi \circ x^{-1}$. The material parameters for the x-system are given by equations (2.3) and (2.4). These expressions are convenient, because the Jacobian is expressed in terms of x-coordinates and the transformations from x to ξ and z to ζ are identities. The only interesting component of each transformation is υ, expressed in Fig. 2.2, and equations (2.5)–(2.10).

$$\upsilon_{defect} = \alpha y, \tag{2.5}$$

$$\upsilon_1 = y + \frac{w}{2}(1-\alpha)\frac{y - y_e}{y_e - w/2}, \tag{2.6}$$

$$\upsilon_2 = y - y(1-\alpha)(1 - \frac{z - z_c}{z_v - z_c}), \tag{2.7}$$

$$\upsilon_3 = y - \frac{w}{2}(1-\alpha)(1 - \frac{x-x_c}{x_v-x_c} - \frac{y-w/2}{y_e-w/2}), \tag{2.8}$$

$$\upsilon_4 = y - y(1-\alpha)(1 - \frac{x-x_c}{x_v-x_c} - \frac{z-z_c}{z_v-z_c}), \tag{2.9}$$

$$\upsilon_5 = y - \frac{w}{2}(1-\alpha)(1 - \frac{x-x_c}{x_v-x_c} - \frac{y-w/2}{y_e-w/2} - \frac{z-z_c}{z_v-z_c}). \tag{2.10}$$

2.2.4 Penetration depth transformation

Different frequencies of the excitation field cause different penetration depths. This is challenge for detection of defects, that relies on accurate computation of eddy currents. The current flaw around the defect is shown in Fig. 2.3. The mesh should correctly take into account the localization of the current density around and below the defect. The exponential decay of the current density calls for a mesh with several layers of elements in one penetration depth. The problem is that the penetration depth depends on the excitation frequency, typically leading to re-meshing for each frequency.

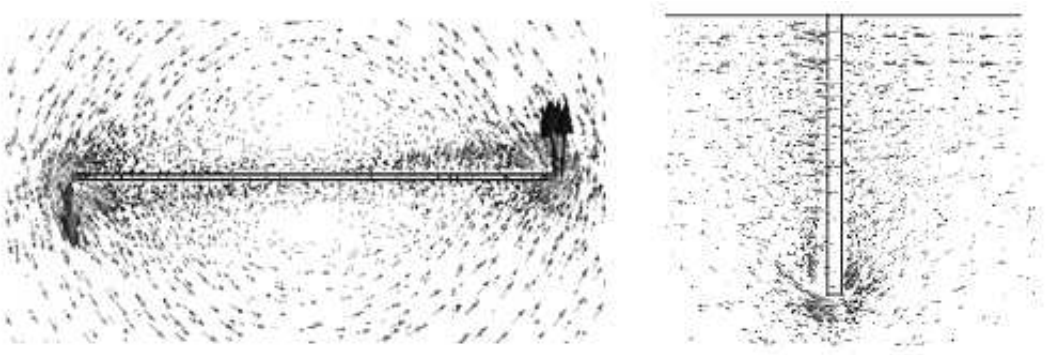

Figure 2.3: Eddy current distribution around a defect inside a plate for a given position of the excitation coil from a top view (left) and on a cut plane of the plate (right).

Our proposal is to work with a single mesh (protype mesh) and apply metric transformations to adapt it for study of problems with different excitation frequencies, as shown in Fig. 2.4. We henceforth call the layer where the defect resides the "top layer" and the layer underneath the defect the "bottom layer".

On the top layer, we propose an exponential transformation, adapt for the cases of small penetration depth (see Fig. 2.5). Applying the mapping to a layer between z_1 and z_2, such that we increase the mesh density towards z_2 we obtain:

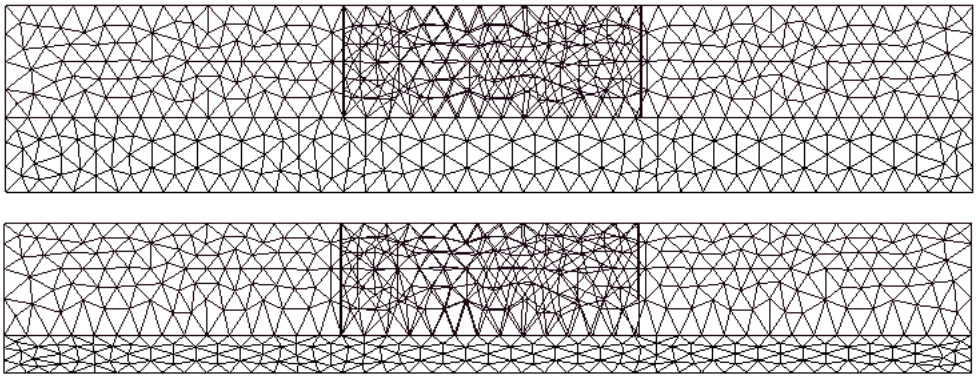

Figure 2.4: The mesh in the non-standard parameterization (above). It is mapped to the mesh in a standard parameterization (below): Top layer by exponential mapping, bottom layer by linear compression. (Two superposed surface meshes visible in the defect area.)

$$\zeta = \frac{\beta^{\frac{z-z_1}{z_2-z_1}} - 1}{\beta - 1}(z_2 - z_1) + z_1, \tag{2.11}$$

with displacement parameter β satisfying $\beta > 1$.

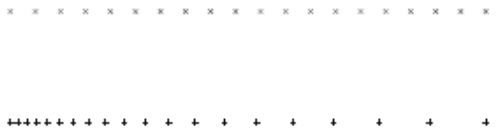

Figure 2.5: Exponential mapping of mesh points in z-direction from a non-standard (even point spacing) to a standard parameterization.

On the bottom layer, we propose a linear compression in order to increase uniformly the elements density on the bottom layer between the coordinates z_1 and z_c. To extend the layer from z_c to z_e, we obtain the mapping:

$$\zeta = (z(z_1 - z_c) + (z_1 - z_c)z_1)/(z_1 - \gamma z_c), \tag{2.12}$$

where γ is the aspect ratio z_e/z_c.

It is, of course, possible to compose mappings to deal with both geometric and penetration depth changes in one go. The Jacobian J of a composite mapping $f_1 \circ f_2$

Figure 2.6: Linear compression of mesh points in z-direction from a non-standard (even point spacing) to a standard parameterization.

is the product of the single Jacobians J_1 and J_2:

$$J = J_1 J_2. \tag{2.13}$$

2.2.5 Differential Formulation

The magneto-quasi-static model is used [29] and the boundary value problem is formulated in terms of the magnetic vector potential A and electric scalar potential V. Specifically, we use the symmetrized version of $A, V - A$ formulation [19], and impose the uniqueness of the magnetic vector potential with the tree-co-tree gauge [30]. The domain is topologically simple, with no cavities or tunnels through it. We assume the media linear. The current in the driving coil is imposed, and the magnetic vector potential it causes without eddy current is first computed. The magnetic vector potential due to the eddy currents are subsequently solved for. Current flow out of the conducting sample is prohibited, as is the magnetic flux out of any part of the domain boundary. Let us start from the Gauss law:

$$\nabla \cdot \mathbf{B} = 0 \Rightarrow \mathbf{B} = \nabla \times \mathbf{A} \tag{2.14}$$

and the Faraday law:

$$\mathbf{E} = -\frac{\partial \mathbf{A}}{\partial t} - \nabla \mathbf{V} \tag{2.15}$$

and finally the Ampere-Maxwell law:

$$\nabla \times 1/\mu_0 \nabla \times \mathbf{A} = \mathbf{J}_s + \mathbf{J}_{eddy} \tag{2.16}$$

Where $\mathbf{J}_s$ is the source density current and $\mathbf{J}_{eddy}$=$\sigma\mathbf{E}$ is the eddy current density. Now we can divide the contribution of the source field B_s by the reaction field B_r

introducting the following position:

$$\mathbf{A} = \mathbf{A}_s + \mathbf{A}_r \tag{2.17}$$

where $\mathbf{A}_s$ is the magnetic vector potential due to the source and $\mathbf{A}_r$ is the reaction vector potential inducted by the eddy currents. The magnetic vector potential is pre-calculated with the Ampere-Maxwell law considering as source the current density J_s in the coil:

$$\nabla \times 1/\mu_0 \nabla \times \mathbf{A}_s = \mathbf{J}_s \tag{2.18}$$

Taking into account the position (2.17) and equation (2.18) for $\mathbf{A}_s$ we have that the equation for the reaction magnetic vector potential is given by:

$$\nabla \times 1/\mu_0 \nabla \times \mathbf{A}_r = -\sigma \cdot (\frac{\partial \mathbf{A}_r}{\partial t} + \frac{\partial \mathbf{A}_s}{\partial t} + \nabla \mathbf{V}) \tag{2.19}$$

The unicity of the magnetic vector potential is guaraanted with the tree-cotree gauge which imposes zero values for $\mathbf{A}$ on the trees of the finite element mesh. In the conductive regions the unicity is imposed with the gauge condition:

$$\nabla \cdot \mathbf{J} = 0 \tag{2.20}$$

this condition coupled with the Neumann condition:

$$\mathbf{J} \cdot \mathbf{n} = 0 \tag{2.21}$$

guarantees that the equation for the scalar potential $\mathbf{V}$ is well-posed. In fact we can rewrite the equations (2.20) and (2.21):

$$\nabla \cdot \sigma \nabla \mathbf{V} = -\nabla \cdot \sigma \frac{\partial \mathbf{A}_s}{\partial t} - \nabla \cdot \sigma \frac{\partial \mathbf{A}_r}{\partial t} \tag{2.22}$$

$$\frac{\partial \mathbf{V}}{\partial \mathbf{n}} = -\frac{\partial \mathbf{A}_s}{\partial t} \cdot \mathbf{n} - \frac{\partial \mathbf{A}_r}{\partial t} \cdot \mathbf{n} \tag{2.23}$$

$\mathbf{V}$ is actually defined up to a constant value which can be set by defining V at one point P in the space:

$$\mathbf{V}(P) = C \tag{2.24}$$

where C is a costant. Now the Galerkin formulation can be derived by representing the unknows as:

$$\mathbf{A} = \sum_{l=1}^{n} a_l W_{e,l} \tag{2.25}$$

$$\mathbf{V} = \sum_{s=1}^{n} v_s W_{n,s} \tag{2.26}$$

where W_e are the Whitney edge basis functions and W_n are the Whitney nodal functions. Simplicial meshes are used to span Whitney function spaces [31], W_e for A and W_n for V.

2.2.6 Computational example

TEAM test problem number 8 [32] is used as the computational example. The problem features a defect that is a $40 \times 10 \times 0.5$ mm rectangular crack at the surface of an austenitic 18-10MO steel plate with relative permeability $\mu_r = 1$ and conductivity $\sigma = 0.14 \times 10^7$ S/m. We calculate the transfer impedance parameter by the difference of magnetic fluxes in the receptive coils, normalized such that the impedance at the last scan position is $0 + 1j$ in the complex plane. The models were constructed with gmsh pre-processor [33], and the computations were carried out with GetDP [34]. The

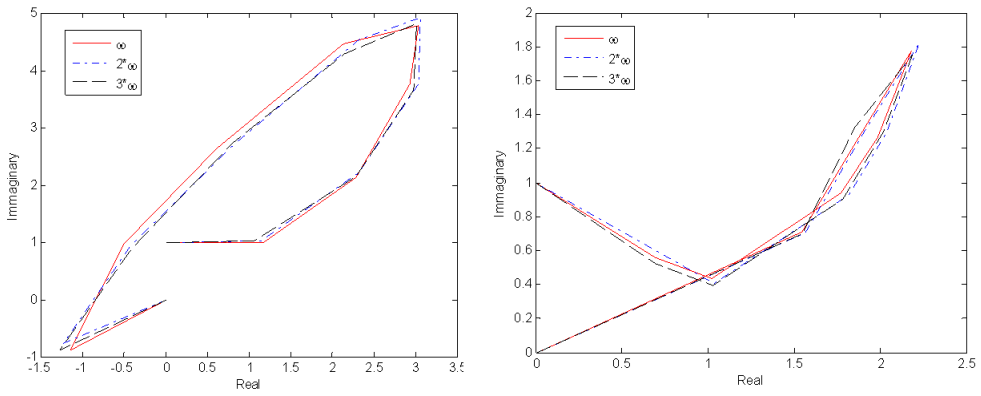

Figure 2.7: Normalized values of real and imaginary part of the impedance, for a parallel (above) and perpendicular (below) scan, with values 1 (continuous line), 1/2 (·-), 1/3 (-) for α.

first simulation, whose result are presented in Fig. 2.7 demonstrates two strengths of

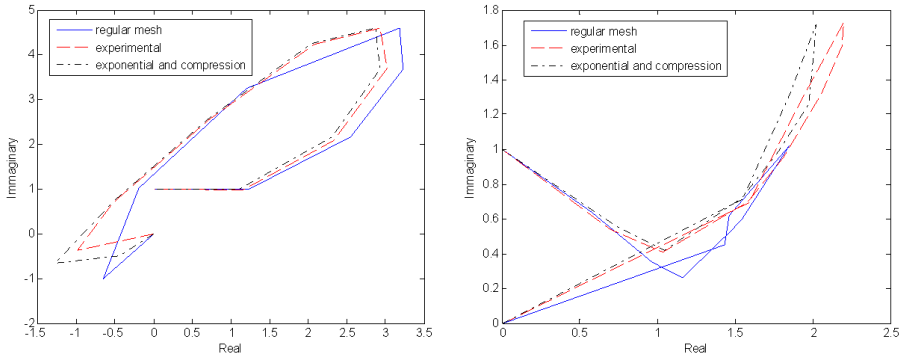

Figure 2.8: Normalized values of real and imaginary part of the impedance for a parallel (above) and perpendicular (below) scan. Numerical results obtained with a mesh without transformations (-), a mesh where there are both exponential and compression transformations (-·-), experimental results (continuous line).

the proposed technique: the high aspect ratio of the defect can be reduced somewhat to ease the meshing, and defects of different widths can be computed with a single mesh.

The Fig. 2.7 shows the real and imaginary part of the impedance, for a parallel and perpendicular scan of the active probe [32], with values $1, 1/2, 1/3$ for α. The results with different values of α show reasonable mutual agreement, according to the fact that they pertain to the same defect in the standard parameterization. The experimental results indicate that we need to increase the mesh density on the top layer and on the bottom layer in order to follow the current variations. We start the computations with a prototype mesh and then apply both the exponential and the compression transformations. The results are shown in Fig. 2.8.

The Fig. 2.8 shows that the computation of the impedance with the prototype mesh produces some mismatch with the experimental data. If we apply both the exponential and compression transformations in order to improve the mesh density near the defect, the numerical results show a reasonable agreement with the experimental ones. The values chosen for β and γ are respectively 2.2 and 1.5.

2.3 The CARIDDI_ECT Integral Formulation

Here we briefly summarize the CARIDDI_ECT numerical model [2, 3] assuming linear constitutive relationships and time harmonic operation (hereafter the $e^{j\omega t}$time dependence is assumed). We refer to perfectly insulating defects. The formulation is described

in more details in the **Appendix A**.

In this formulation the Faraday's law is automatically satisfied by expressing the electric field as:

$$\mathbf{E} = -j\omega\mathbf{A} - \nabla\varphi \tag{2.27}$$

whereφ is the electric scalar potential and $\mathbf{A}$ is the magnetic vector potential:

$$B = \nabla \times A \tag{2.28}$$

that, under the Coulomb gauge, can be related to the unknown current density by the integral expression:

$$\mathbf{A}(\mathbf{r}, t) = \frac{\mu_0}{4\pi} \int_{V_c} \frac{\mathbf{J}(\mathbf{r}', t)}{|\mathbf{r} - \mathbf{r}'|} d\mathbf{r}' + \mathbf{A}_s(\mathbf{r}, t) \tag{2.29}$$

$\mathbf{A}_s$ being the magnetic vector potential due to the source current $\mathbf{J}_S$. The electric constitutive equation is imposed in weak form as:

$$\int_{V_c} (\eta\mathbf{J} - \mathbf{E}) \cdot \mathbf{W} d\mathbf{r} = 0, \qquad \mathbf{J} \in S, \qquad \forall \mathbf{W} \in S \tag{2.30}$$

where η is the electric resistivity, S=$\{\mathbf{J}\in \mathrm{L}^2_{div}(\mathrm{V}_c)$, $\nabla\cdot\ \mathbf{J} = 0$ in V_c, $\mathbf{J}\cdot\hat{\mathbf{n}} = 0$ on $\partial\mathrm{V}_c\}$, $\mathrm{L}^2_{div}(\mathrm{V}_c)$ is the space of vector fields that are square integrable in V_c together with their divergence, and $\hat{\mathbf{n}}$ is the outward normal defined on the boundary of V_c. In order to get the numerical model, the current density is expanded in terms of solenoidal shape functions with normal component zero on ∂V_c. The shape functions are the curl of edge elements shape functions $\mathbf{N}_k$:

$$\mathbf{J} = \sum_k I_k \nabla \times \mathbf{N}_k \tag{2.31}$$

The Degrees of Freedom (DoFs) are related to the edges of the finite element mesh and represent the integrals of the tangential component of the electric vector potential $\mathbf{T}$ ($\mathbf{J} = \nabla\times\mathbf{T}$) along the edge. The gauge and the boundary conditions can be imposed by using the tree-cotree decomposition as described in [2, 3]. By imposing these two conditions, it follows that the unknowns are restricted to only a proper subset of edges of the finite element mesh. The edges of this subset are termed active edges.

The numerical model is finally obtained by combining eqq.(5.9) and (2.31) through the Galerkin method yielding:

$$\left(\underline{\underline{R}} + j\omega\underline{\underline{L}}\right)\underline{I} = \underline{\mathrm{V}} \tag{2.32}$$

where $\mathrm{I} = \{\mathrm{I}_k\}$, $\mathrm{V}=\{\mathrm{V}_k\}$ and

$$L_{ij} = \frac{\mu_0}{4\pi}\int_{V_c}\int_{V_c}\frac{\nabla\times\mathbf{N}_i(\mathbf{r})\cdot\nabla\times\mathbf{N}_j(\mathbf{r}')}{|r-r'|}d\mathbf{r}d\mathbf{r}' \tag{2.33}$$

$$R_{ij} = \int_{V_c}\nabla\times\mathbf{N}_i(\mathbf{r})\cdot\eta\nabla\times\mathbf{N}_j(\mathbf{r})d\mathbf{r} \tag{2.34}$$

$$V_i = -j\omega\int_{V_c}\nabla\times\mathbf{N}_i(\mathbf{r})\cdot\mathbf{A}_S d\mathbf{r} \tag{2.35}$$

In case of linear problems, to improve the accuracy and speed of the numerical calculation, it is possible to use the superposition principle. With the superposition principle the first step is to calculate the solution of the direct problem without the flaw (the unperturbed current density $\mathbf{J}_0$). For canonical shape of the conducting domain, as is the case for the infinite plate [35] and thin plates [36], it is possible to use analytical expressions. Otherwise it is possible to solve the forward problem numerically. The second step (perturbed solution), consists in solving the problem obtained by imposing that the total current $\mathbf{J}=\mathbf{J}_0+\delta\mathbf{J}$ is equal to zero in the flaw. In order to improve the accuracy, we solve this second forward problem in term of the eddy current density perturbation $\delta\mathbf{J}$. It is worth noting that $\delta\mathbf{J}$ is essentially localized in a neighbourhood of the defect whereas $\mathbf{J}_0$ is circulating in a much larger region, i.e. the problem is intrinsically multiscale. Moreover, this separate computation of $\mathbf{J}_0$ and $\delta\mathbf{J}$ allows to avoid ill-conditioning due to elements with size of different order of magnitude and to reduce the number of elements. Indeed, we can use a coarser and larger mesh for computing the unperturbed current and a finer and smaller mesh for computing the perturbed current, so that we can minimize the overall computational time and improve the accuracy.

Finally, from the eddy current perturbation $\delta\mathbf{J}$ it is possible to calculate the impedance

change in the exciting coil as:

$$\delta \mathbf{Z} = j\omega \int_{Coil} \delta \mathbf{A} \cdot \mathbf{J}_S d\mathbf{r} / \mathbf{I}_S^2 \tag{2.36}$$

$$\delta \mathbf{Z} = j\omega \int_{V_C} \mathbf{A}_S \cdot \delta \mathbf{J} \; d\mathbf{r} / \mathbf{I}_S^2 \tag{2.37}$$

where $\delta \mathbf{A}$ is the vector potential due to $\delta \mathbf{J}$. Equation (2.36) is the standard expression while (2.37) is given by the reciprocity theorem and usually produces more accurate results. In the following section the integral formulation is applied to problems arising from the nuclear power industry. Specifically, we consider the inspection of a steam generator tube without and with the support plate. The specific configurations, as well as the experimental data used for the validation, are from benchmark problems provided by the Commissariat l´nergie Atomique (CEA) at Saclay (France).

2.3.1 Numerical Results

In the following section we will show numerical results that simulate four types of NDT benchmark problems proposed by the Commissariat a lÉnergie Atomique (CEA). The first two refer to the inspection of tubes using either an internal bobbin coil and an external bobbin coil. The third benchmark involves a steam generator tube with the support plate, whereas the last benchmark concerns the inspection of a planar slab with an air coil probe.

2.3.1.1 Tube inspection

The considered tube has the typical dimensions and material properties from nuclear power plants applications. The tube is made by Inconel, a nonmagnetic alloy with conductivity 1MS/m, and it has the following dimensions: Rmin=9.84mm (inner diameter), etube=1.27mm (wall thickness). We considered two differential probes: an internal axial probe and an external axial probe. Each probe is made by two coils operating in differential mode. The measurement consists of the voltage across the two coils of the probe are connected to the branches of a Wheatstone bridge working close to its equilibrium when the specimen is unflawed (see Fig.2.9). The internal

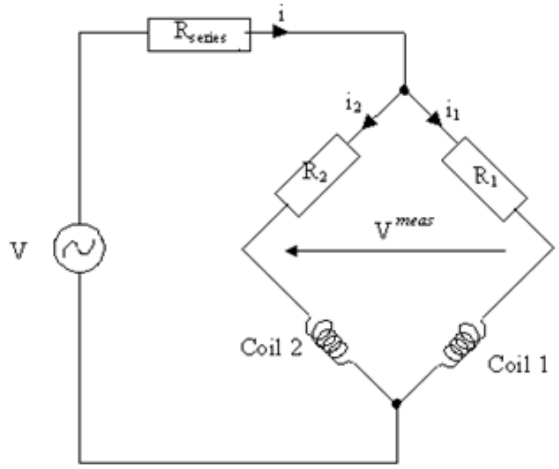

Figure 2.9: The measurement circuit. Coil 1 and Coil 2 are the two coils that are part of a single probe.

axial probe is made by two bobbin coils characterized by the following parameters: internal radius Rmin=7.83mm, external radius Rmax=8.50mm, height h=2.00mm, gap between the coils d=0.50mm, number of turns N=70. The inspection is carried out at the frequency f=100kHz. The external axial probe is made by two bobbin coils characterized by the following parameters: internal radius Rmin= 11.3mm, external radius Rmax= 12.313mm, height h = 2.01mm, gap between the coils d=0.99mm, number of turns N=20. The inspection is carried out at the frequency f=120kHz. The numerical models calculate the impedance variation of the probe during the scanning whereas in industrial applications, as in our case, the data consists of voltage measurements rather than impedance measurements. Since the voltage values depend upon several parameters of the experimental set-up (gain of the amplifier, amplitude of the injected current, resistances in the Wheatstone bridge, etc), the numerical computed measurements need to be calibrated on some reference flaws. Usually, the numerical signals are calibrated through a rotation and magnification in the complex plane in order to match the amplitude and phase of the experimental signals for the reference flaw. Specifically, the numerical data after the calibration are the complex voltages $\dot{V}_k$'s (k being the position of the probe) that are obtained from the numerically computed impedance value $\dot{z}_k$ as $\dot{V}_k = \dot{M}\ \dot{z}_k$, where $\dot{M}$ is a complex constant. The complex constant $\dot{M}$ can

be obtained by solving the following least-square problem:

$$\min_{\dot{M}} \sum_{k} \left| \dot{V}_k^{meas} - \dot{M}\, \dot{z}_k \right|^2 \tag{2.38}$$

where $\dot{V}_k^{meas}$ is the experimentally measured complex voltage at the k-th location. The flaws used for calibrating the internal and external bobbin coils are, respectively, an outer groove flaw termed GE40 (40 % of the tube thickness, height of 1mm along the tube's axis) and a through-wall borehole with a diameter of 1mm termed TFP1. Specifically the CEA prescribes, for the two benchmarks, the distance and the direction for the two peaks of the impedance appearing in the Lissajous plot as shown in Tab.2.1 and Fig.2.10.

Flaw	A (V)	$\varphi(^\circ)$
GE40	2.814	+141.8
TFP1	0.980	-169.8

Table 2.1: Amplitude and phase for the reference flaws.

From Fig.2.10 it is evident the excellent agreement between the experimentally measured data and the numerically computed data (after the calibration) achieved on the reference flaws. Specifically, the relative errors defined as:

$$\sqrt{\sum_{k} \left| \dot{V}_k^{meas} - \dot{V}_k^{num} \right|^2 \Big/ \sum_{k} \left| \dot{V}_k^{meas} \right|^2} \tag{2.39}$$

where $\dot{V}_k^{num}$ is the numerically computed voltage are: 0.08 (CARIDDI_ECT) and 0.09 (CIVA) for reference flaw GE40 and for 0.089 (CARIDDI_ECT) and 0.077 (CIVA) for reference flaw TFP1. The relative discrepancy between CARIDDI_ECT and CIVA is 0.0132 on GE40 and 0.039 on TFP1. The discrepancies between the numerically computed voltages are due to intrinsic differences in the numerical methods such as integration schemes and meshes. On the other hand, the discrepancies between numerical and experimental results are mainly due to uncertainty affecting parameters such as the lift-off, material properties, etc. In any case, the agreement is excellent for industrial applications. Once the calibration constants have been evaluated on the reference flaws, they can be applied to any other configuration where only the geometry of the flaws is changed. In the following we apply the calibration constants evaluated

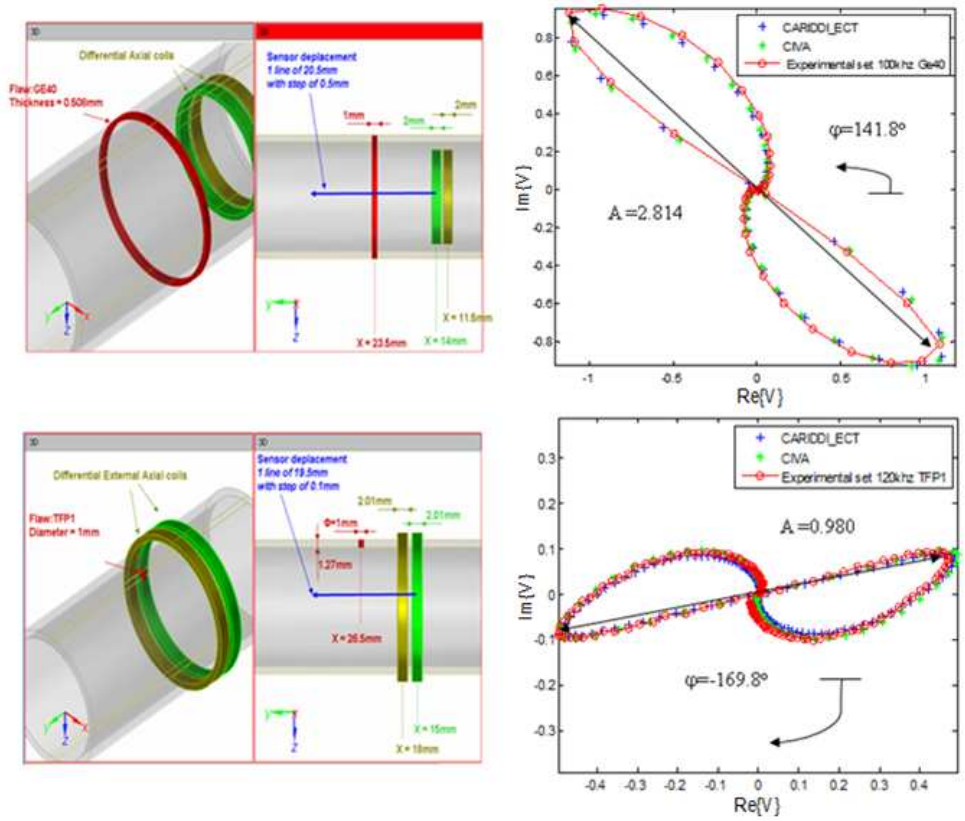

Figure 2.10: Top: description of the inspection procedure for the flaw GE40 (left) and experimental results (o) vs numerical results obtained with the CARIDDI_ECT code (+) and the CIVA code (*) after the calibration (right) @ f=100kHz. Bottom: description of flaw TFP1 (left) and results after the calibration (right) @ f=120kHz.

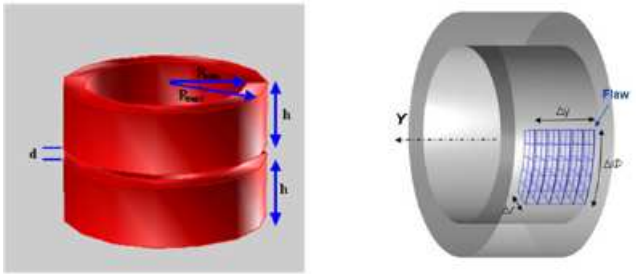

Figure 2.11: The bobbin coil used in the measurements (left). Flaws representation in cylindrical coordinate system (right).

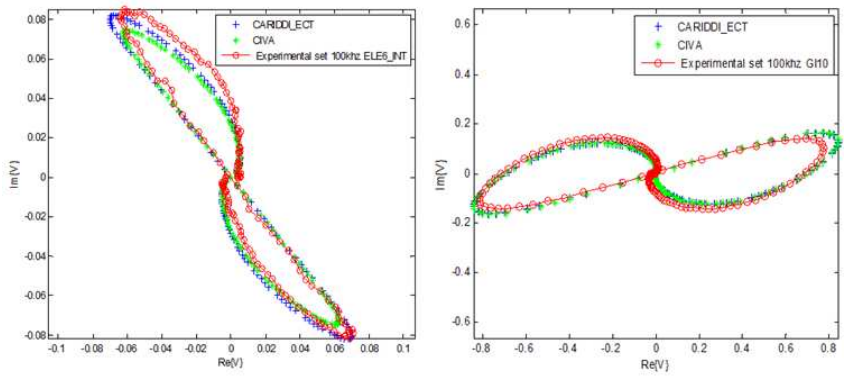

Figure 2.12: Left: the experimental results (o) vs the numerical results obtained with CARIDDI_ECT code (+) and CIVA code (*) for the flaw ELE6. Right: the results for the flaw GI10.

in this section. Two longitudinal notches are considered in the case of the internal bobbin coil. The main parameters describing the flaws (ELE6 and GI10) are shown in Fig. 2.11and Tab.2.2. The inspection is carried out at the frequency f=100kHz. The comparison between the experimental and numerical results for the two flaws is shown in Fig.2.12.

Flaws	Descriptions	Dimensions		
		Δr	$\Delta\Phi$	Δy
ELE6	External Longitudinal notch, length of 6mm	0.66mm (52%)	0.63 ° (opening: 0.12mm)	6mm
GI10	Internal groove 10% of the tube thickness	0.127mm (10%)	360 °	1mm
ELE10	External Longitudinal notch length of 10mm	0.69mm (54%)	0.60 ° (opening: 0.1mm)	10mm
ET82	Transversal through wall notch, angular extension 82 °	1.27mm (100%)	82 ° (extension: 12.9mm)	0.133mm ± 0.02mm

Table 2.2: Flaws dimensions along the tube

The relative errors with the experimental data are 0.082 (CARIDDI_ECT) and 0.104 (CIVA) for flaw ELE6; 0.121 (CARIDDI_ECT) and 0.130 (CIVA) for flaw GI10.

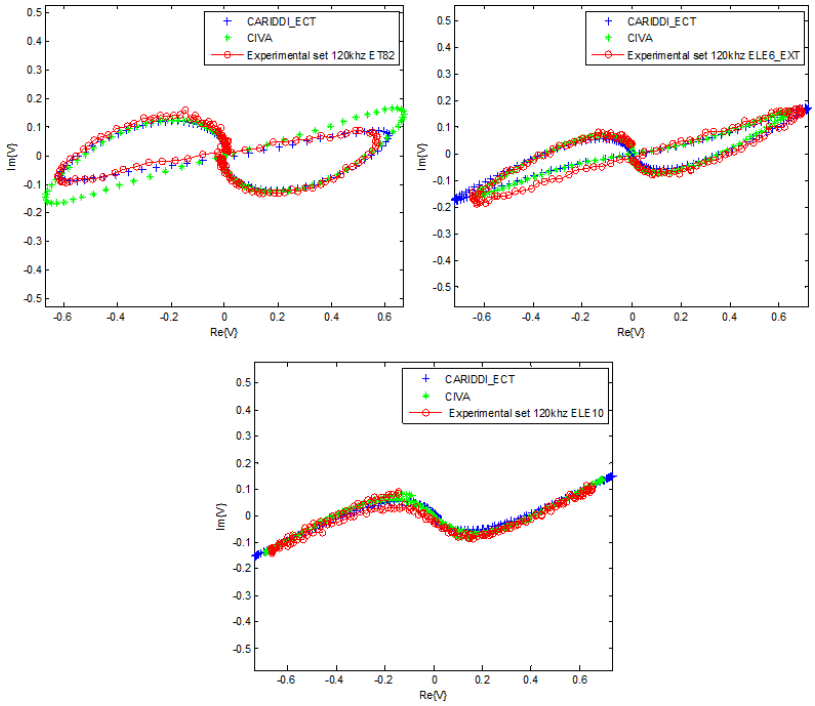

Figure 2.13: Top: the experimental results (o) vs the numerical results obtained with CARIDDI_ECT code (+) and CIVA code (*) for the flaws ET82 (left), ELE6 (right). Bottom results for the flaw ELE10.

The relative discrepancy between CARIDDI_ECT and CIVA is 0.10 on ELE6 and 0.015 on GI10. It is worth noting that the numerical modelling of ELE6 is more difficult than GI10 because of its smaller dimensions (moreover ELE6 is a fully 3D problem whereas GI10 is an axisymmetric problem). As a matter of fact, the signature of ELE6 is one order of magnitude smaller than the signature of GI10. The flaws considered in the case of the internal bobbin coil are a transversal through wall notch (ET82) and two longitudinal notches (ELE6 and ELE10) described in Tab.2.3. The inspection is carried out at the frequency f=120kHz. The comparison between the experimental and the numerical results is shown in Fig.2.13. The relative errors against the experimental data are 0.1811 (CARIDDI_ECT) and 0.1811 (CIVA) for flaw ET82; 0.105 (CARIDDI_ECT) and 0.125 (CIVA) for flaw ELE6; 0.132 (CARIDDI_ECT) and 0.091 (CIVA) for flaw ELE10. The relative discrepancy between CARIDDI_ECT and CIVA is 0.154 for ET82, 0.118 for ELE6 and 0.081 for ELE10. We notice that for flaw ET82 both CARIDDI_ECT and CIVA give the same relative error against the experimental data, despite figure 6 (left) shows that the graph of the signature obtained

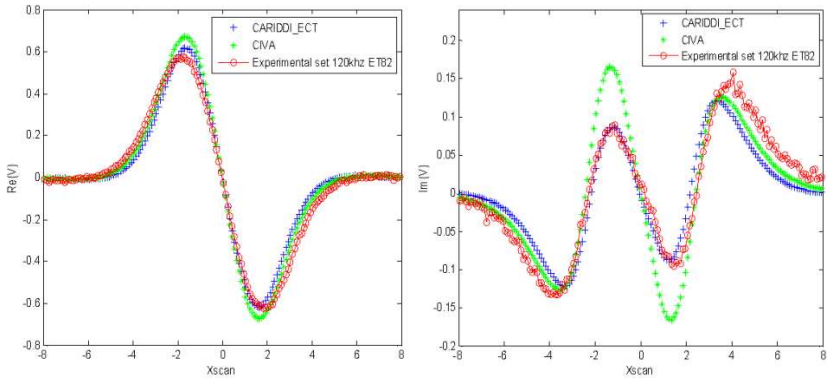

Figure 2.14: Real (left) and imaginary (right) parts of the voltages as a function of the spatial position for flaw ET82. Experimental results (o), CARIDD_ECT numerical results (+) and CIVA numerical results (*).

by means of the CARIDDI_ECT is definitely better than the graph of the signature for the CIVA if compared to the experimental data. The sources of the relative errors can be better understood by considering the plot of the real and imaginary parts of the voltages as a function of the probe position (see Fig.2.14). From this figure it appears that the discrepancies against the experimental data are mainly in the imaginary part that, moreover, is the smaller component and, thus, contributes in a secondary manner to the relative error.

2.3.1.2 Steam Generator Tube with a Support Plate

This benchmark concerns a steam generator tube with a nonmagnetic support plate. In the nuclear power plant the tubes are usually supported with plates that are termed support plates.

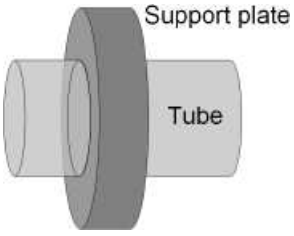

Figure 2.15: The tube with a support plate.

The plate gives a major complexity to the defect detection by eddy current because it produces signals having amplitude usually much larger than that due to the defect.

In this example the tube is the one considered in the previous simulations. The support plate consists of a copper, alloy with conductivity plate=58 MS/m and thickness 20mm. It is in mechanical contact but electrically insulated from the tube as shown in Fig.2.15. In Fig.2.16 are shown the results related to the case GE40 at f=100kHz. Since

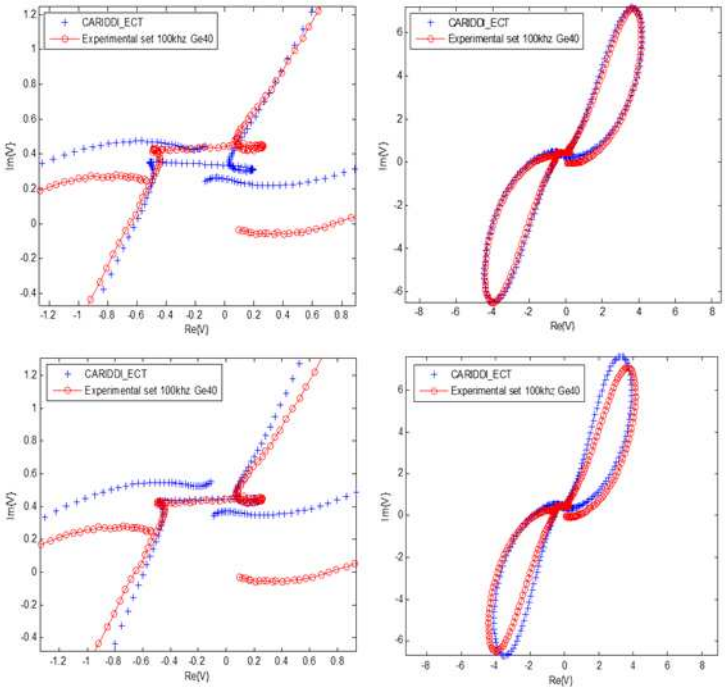

Figure 2.16: Top: matching by fitting the field due to the support plate (major lobes), local view (left), global view (right). Bottom: matching by fitting the field due to the notch, local view (left), global view (right).

calibration signals are not available, we compare the signals after performing a best fit consisting in a proper phase rotation and amplification, as for the previous case, plus a translation compensating a background voltage. However, in this case we found that it is not possible to match with the same rotation, amplification and translation both the major lobes (mainly due to the support plate) and the central area (mainly due to the notch). Therefore, we applied two different matching: (i) a matching on the major lobes and (ii) a matching on the central area, as shown in Fig. 2.16. In both cases, the agreement after the matching is remarkable. The existence of two different matching denotes potential errors such as lift-off etc. affecting the experimental measurements.

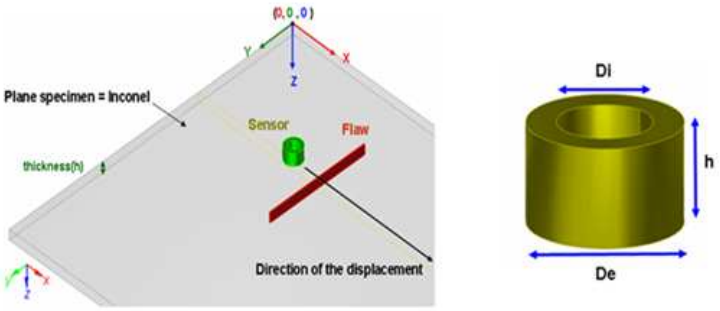

Figure 2.17: Measurement scheme (left). The coil used in the measurements (right).

Finally, we highlight that the CARIDDI_ECT, due to its capability of treating full 3D backgrounds, can be applied straightforwardly for modelling this non-canonical geometry where Green's dyadic are difficult or impossible to be computed.

2.3.1.3 Slab inspection using an air-core coil

The flaws considered in the following case are 20mm long notches (see Tab.2.3). The specimen is a nonmagnetic slab made by Inconel (conductivity 10^6S/m, relative permeability 1, thickness 1.55mm).

Flaws	Descriptions	Dimensions		
		$Length(mm)$	$Width(mm)$	$Height(mm)$
FL1(100-20mm-011)	Length 20mm	20	0.11	1.55 (100%)
FL2(80I-20mm-014)	Length 20mm	20	0.14	1.24 (80% in surface)
FL3(40I-20mm-011)	Length 20mm	20	0.11	0.62 (40% in surface)
FL4(80E-20mm-14)	Length 20mm	20	0.14	1.24 (80% in back-wall)

Table 2.3: Flaws dimensions along the slab.

The probe is a single emitting and receiving nonmagnetic-coil with dimensions: internal diameter Di=2mm, external diameter De=3.25mm, height h=2.00mm, number of turns N=328. The inspection is carried out at the frequency f=300kHz. The real and imaginary parts of the impedance of the coil are measured with an impedance analyzer.

The lift-off is 0.303mm and the scanning step is 0.1mm. The sensor is moved along a line crossing orthogonally the defect, as shown in Fig.2.17. The comparison between the experimental and numerical results is shown in Fig.2.18.

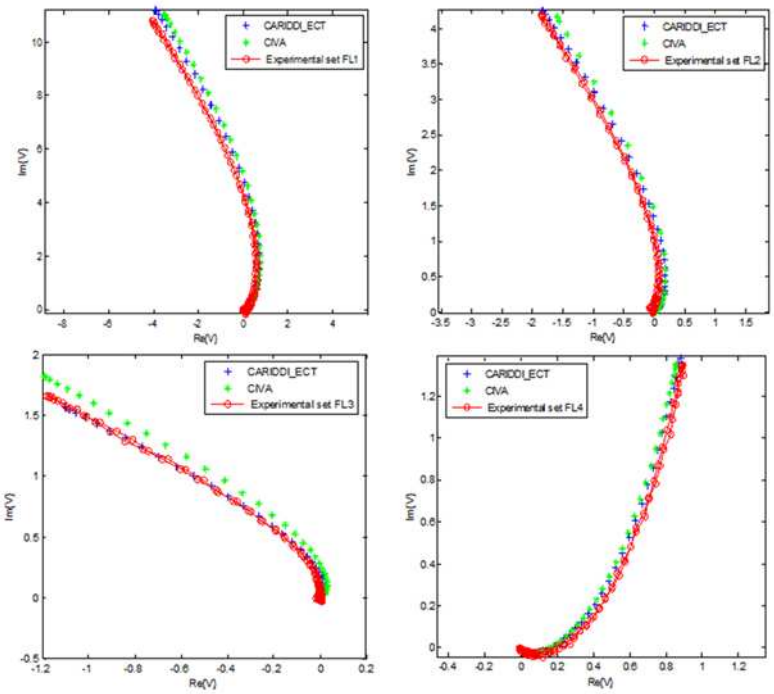

Figure 2.18: Top: experimental results (o) vs numerical results obtained with CARIDDI_ECT code (+) and CIVA code (*) for the flaws FL1 (left) and FL2 (right). Bottom: results for the flaws FL3 (left) and FL4 (right).

The relative errors against the experimental data are 0.049 (CARIDDI_ECT) and 0.069 (CIVA) for flaw FL1; 0.0693 (CARIDDI_ECT) and 0.0992 (CIVA) for flaw FL2; 0.0894 (CARIDDI_ECT) and 0.0863 (CIVA) for flaw FL3; 0.0525 (CARIDDI_ECT) and 0.048 (CIVA) for flaw FL4. The relative discrepancy between CARIDDI_ECT and CIVA is 0.0363 for FL1, 0.0522 for FL2, 0.1318 for FL3 and 0.025 for FL4. We notice that for FL3 we have similar relative errors but slightly different signatures. The CARIDDI_ECT is less accurate than CIVA on the real part but more accurate than CIVA on the imaginary part (see fig. 2.19) thus producing similar relative errors.

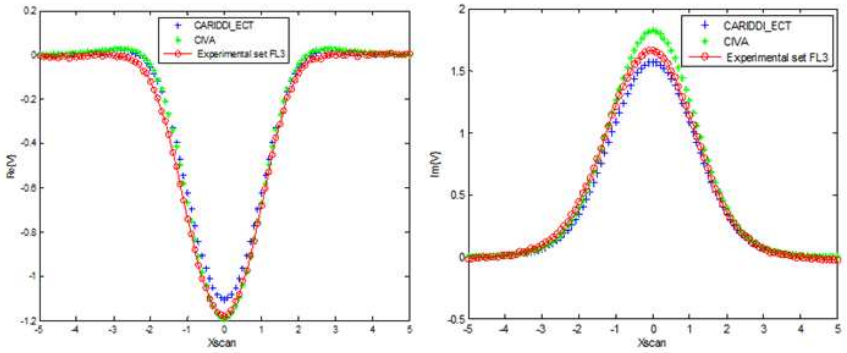

Figure 2.19: Real (left) and imaginary (right) parts of the impedance variation as a function of the spatial position for FL3. Experimental results (o), CARIDDI_ECT numerical results (+) and CIVA numerical results (*).

2.4 Conclusions

In this chapter we propose a new technique based on differential geometry to perform numerical computations in eddy current direct problem. The size of a defect can be parameterized to model a family of defect widths with a single mesh. The avoidance of mesh regenerations makes automated simulation runs immune to mesh generation failures, that are commonplace in problems with narrow defects with differential formulations. Moreover, we show how to adapt a mesh for different penetration depths, dependent on different frequencies [1]. In the second part of the chapter we have illustrated an integral formulation, named CARIDDI_ECT, that allows to treat arbitrary 3D geometrical configurations with defects of arbitrary shape in a background material having arbitrary shape and, eventually, with space varying properties. This integral model requires to discretize the volumetric region where circulates the perturbation of the eddy current density due to the defect and it involves, for building the stiffness matrix, the integration of singular kernels. Finally, the CARIDDI_ECT numerical model has been capable of modelling correctly the response also for a defect near the support plate for a nuclear power plant tube [4]. This, as well known, is a challenging and difficult problem.

3

Iterative Methods for Crack Shape Reconstruction

3.1 Introduction

The following three chapters are dedicated to the inverse problems. First we investigate the iterative methods and later we move to non iterative ones which are the candidate for real-time imaging, they are very fast and no iterations are required to get the shape of the inclusion. In this chapter we show a topology based algorithm to reconstruct the shape of anomalies in eddy current inverse problem. We show an improvement in the reconstructions by exploiting topology informations which improve the convergence of the numerical solution. As well known, the inverse problem of the detection of the shape of defects retrieval from eddy current testing measurements is non-linear and ill-posed (see [39]-[41] for mathematical issues). In particular, the sensitivity of the measurements with respect to the defect shape is poor and therefore, it is very difficult to invert the ECT data. This challenging problem has attracted the interest of the scientific community. We mention papers [42]-[49] about the inversion of ECT data with both iterative (gradient based or stochastic) and non-iterative methods. In this section we describe a new iterative procedure that we have applied to reconstruct inclusions in industrial applications [7] by combining an efficient integral formulation Cariddi_ECT [3] for the direct problem described in the previous chapter and an algorithm based on Topology Costrained Optimization Algorithms (TOPCSA) for the inverse problem [6]. As we explained the Cariddi_ECT formulation restrict the computation of the field

due to the inclusion to a limited region in a neighbourhood of the defect so that only a "small" sub-problem has to be solved; this is particular adapt for an iterative cycle which require the solution of the direct problem for many tentative regions (see Appendix A for details). The inversion (zero-order method) is carried out by the TOPCSA optimization, and compared with the results obtained with a Genetic Algorithm (GA). The GA overcomes the difficulties related to gradient-based optimization methods that can be trapped in local minima in multimodal problems. However such methods rely on operators that are developed to reconstruct specific types of shapes, so that the ability of the GA to evolve complex rules for more realistic topologies is an open question. In the TOPCSA approach the optimization algorithm is an interesting alternative to the GA because it presents both local and global operators with a computational cost at least comparable to the one of the GA and moreover it does not require any kind of recombination method. In the following sections we describe both the GA and TOPCSA algorithms and then, a comparison of the performances obtained by them in processing (inverting) the experimental ECT data.

3.2 Genetic algorithm

Genetic algorithms have been developed to solve optimization problems with natural selection principles. They are suitable to solve non-linear problems where the objective function could even be not continuous and not differentiable. The GA consider a population of individuals (chromosomes or genotypes) and defines a fitness function that evaluates the quality of each individual gi (i.e. how is good the solution for the problem) of a given population P. In abstract terms, the fitness function indicates how individuals adapt to the environment: individual with better fitness are more likely to reproduce and transmit their genes to the future generations. At each step the genetic algorithm uses three main types of operators to create the next generation of individuals:

- Crossover or recombination (inspired by genetics);
- Mutation (inspired by genetics).
- Selection (inspired by natural selection);

The operators select individuals to improve the fitness. Individuals with higher fitness should be privileged over the others. Members selected are placed in a mating pool for reproduction. When the mating pool is filled with n members (number of individuals of the population), n new descendents are generated by applying genetic operators. Two individuals in the mating pool (parents) are chosen at random and portion of their genotype are exchanged (see Fig. 3.1), in order to generate two individuals (children) with characteristics from both parents.

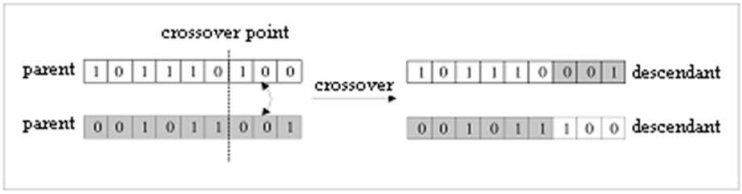

Figure 3.1: Crossover operator. The crossover point is chosen at random.

The crossover operator is applied $n/2$ times; according to a fixed probability $0 < p < 1$, to obtain n individuals. The mutation operator applies a random change with a fixed and small probability pm to a single gene of a chromosome for reintroducing genetic material in the population.

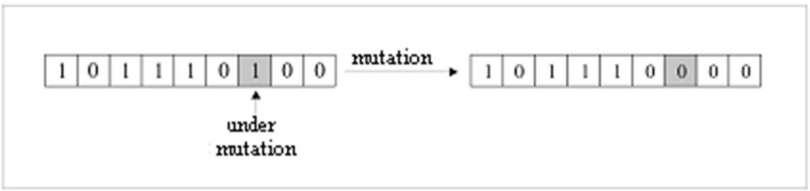

Figure 3.2: Mutation operator. The mutation point is chosen at random.

Regard to selection the operator selects individuals to improve the fitness. Individuals with higher fitness should be privileged over the others.

A termination criterion for the algorithm, may be to achieve a high percentage of individuals of a generation that has the same function as fitness of the best. The GA algorithm can be described with an iterative scheme:

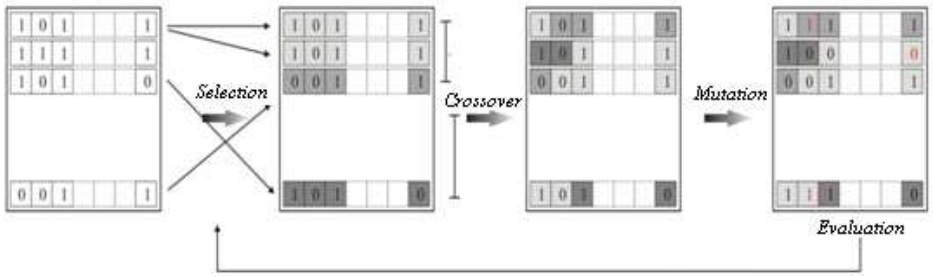

Figure 3.3: Genetic iterative cycle.

```
    t = 0
initialize population P(t) at random
order the population P(t) using a function of fitness
while (termination condition not satisfied)
      select individuals from P(t) and enter them in P1
      select individuals from P1 and enter them in the mating pool (MP)
      apply the crossover to the individuals forming P2
      apply the mutation of P2 individuals forming P3
      form P(t +1) by selecting for the replacement individuals from P3 and P(t)
      t = t +1
end while
```

3.3 Topology Constrained Optimization Algorithm

Shape inclusion optimization usually starts from initial user-defined configuration of material. Optimization algorithms are then applied for optimizing objective functions starting form predefined parameters. A different approach to the shape optimization is the Topology Constraint Optimization algorithm (TOPCSA) described in [6]. It is worth noting that the TOPCSA is capable of treating arbitrary topologies: the material properties at every point of the design space are considered in the design processes. The TOPCSA algorithm is an interesting alterative to the GA because it presents both local and global operators with a computational cost comparable to the one of genetic algorithms. The TOPCSA algorithm starts by generating *Npop* initial distributions in the material. The performance of these distributions, called antibodies, is evaluated in an iterative cycle with an fitness function subject to a given criterion. The first *Nsel* antibodies are selected and some copies, called clones, are generated which are subjected to an affinity maturation (local operator) process or to a macromutation

process (global operator). The number of clones for each iteration i is given by:

$$N_C^i = \frac{\beta N_{sel}}{i} \tag{3.1}$$

Where the ratio is approximated by the upper natural number. The parameter is a constant that regulates the number of clones. After that, the fitness of the clone is evaluated, and the clone replaces the original antibody if it presents a better fitness. The antibodies that are not selected for cloning are replaced by a new material configuration randomly generated. This process is performed with several generations. The iterative cycle is repeated until some stop criterion is reached. From this scheme it seems that the computational effort is too high with respect to the genetic algorithm. In order to avoid this, the size of the population is progressively reduced, until $Npop = Nsel$, i.e until all the antibodies are selected for cloning. At the same time, the parameter regulating the number of clones is increased, in order to intensify the local evolution of the material distributions. With this strategy, it is possible to narrow the search for the optimal topology around the most promising solution.

3.3.1 Affinity maturation

The affinity maturation is the main local operator and it involves only a limited area of the interested domain, usually corresponding to the pixels on the boundary of the inclusion that have an empty pixel on both side.

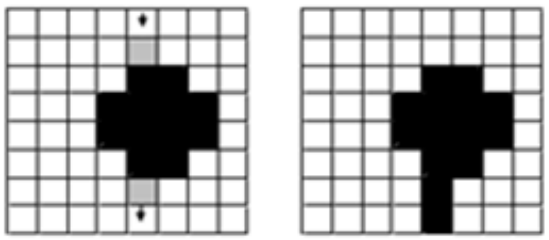

Figure 3.4: Domain with inclusion before (left) and after (right) the affinity maturation. The grey pixel are interested in the process and the arrows are indicative of the relative mutation direction, while the dark pixel are representative of the pixel belonging to the inclusion not considered by the operator.

The affinity maturation is performed at random with a prescribed probability.

3.3.2 Cleaning

This operator is dedicated to avoid isolated filled elements in the material. It checks the neighbors of each element so that if the four side of a filled element are empty, the considered pixel is also converted to empty, as shown in the next figure.

3.3.3 Surface Smoothing

This operator is equivalent to the cleaning, but it involves pixel on the boundary of the whole domain that presents three empty elements as shown in the next figure.

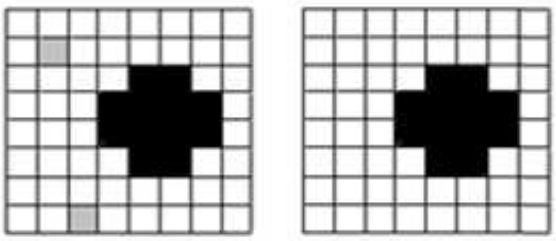

Figure 3.5: Domain with inclusion before (left) and after (right) both the cleaning and the surface smoothing operators. The grey pixel in the bottom is interested in the surface smoothing process, while the pixel in the top is interested by the cleaning.

3.3.4 Macromutation

This last operator is the main helpful in crack reconstruction . It helps the algorithm to explore areas, randomly chosen, that can belong to the inclusion by setting a group of neighbor elements to the same state. This operator helps the algorithm in exploring new regions of the search space, to generate shapes with holes in the middle of material regions, and to escape local minima in the later generations [6], when the population size is reduced according to (3.1).

The TOPCSA algorithm can be described with an iterative scheme:

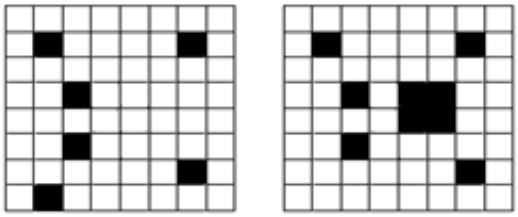

Figure 3.6: Domain with a random distribution in the material before (left) and after (right) the macromutation operator.

```
    t = 0
assign algorithm parameters: Npop, Nsel, b and initialize population P(t)
while (termination condition not satisfied)
    Evaluate and sort the antibodies from P(t)
    for the first Nsel better antibodies
        for Nc times
        Generate a clone and apply either one of the Global Operators
        or the Affinity Maturation
            if the clone outperforms its parent antibody
            than it replaces the antibody in the population P(t)
            end if
        end for
    end for
    Recalculate Npop, Nsel, b
    t = t +1
end while
```

3.4 Experimental setup

In the following we show a comparison between the TOPCSA and GA algotithms for both 2D and 3D reconstructions together with an experimental validation. The measurement system is composed by a robot scanner, a sliding probe for fastener inspection and an impedance analyser. The robot scanner, produced by Mitsubishi Electric, named Melfa RV-1A, is composed by six joints which reproduce all the degrees of freedom related to the human arm movement with a precision of 0.02 mm. The robotic arm is controlled by a PC via RS-232 interface (see Fig. 3.8). The probe is a dual element reflection probe with a complex ferrite magnetic circuit [50, 51]. For this kind of probe-defect interaction we used for the direct problem computation the numerical formulation Cariddi_ECT in presence of linear magnetic materials whose details

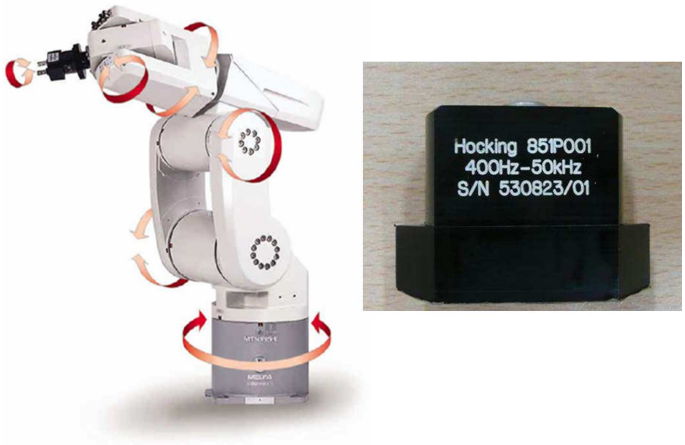

Figure 3.7: Robot Melfa RV-1A (left), reflection probe (right).

are shown in **Appendix A**. EC signals from the sliding probe were measured by an impedance analyzer . Both the robotic arm and EC instrument were controlled by a PC via RS-232 interface (see Fig. 3.8). The measurement have been performed with a frequency of 25KHz to get an appropriate signal to noise ratio.

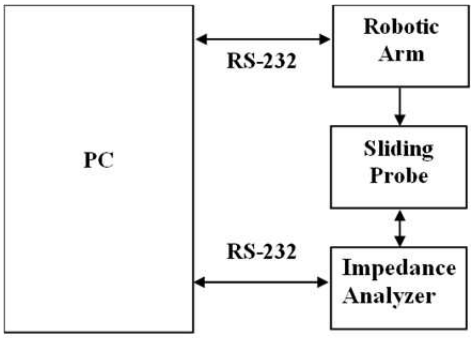

Figure 3.8: Block diagram of the measurement system.

3.4.1 2D Reconstructions

The sample used in our first test is a titanium plate used in aeronautical application, provided by Alenia Aeronautica S.p.A (Naples, Italy). The slab has dimensions 12.5cm×12.5cm×0.35cm and a background conductivity of 0.55 MS/m.

The plate has an through-wall hole on the top and three fatigue cracks, as indicated by Alenia Aeronautica S.p.A, whose orientations, dimensions and shapes are unknown

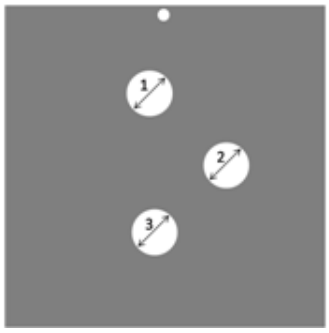

Figure 3.9: Titanium plate SPT 10-T with a through-wall hole on the top and three defects contained within the region 1,2 and 3. The regions have a circular cross-section with a diameter of 5mm. Each defect is a fatigue crack. Metallographic cross-sections are not available for this specimen.

(see Fig. 3.9 and its caption). On this titanium plate we performed several reconstructions starting from the related experimental data. The EC inspection is performed by robotic scanning of samples along straight lines containing both the hole and the three flaws with the sensitive axis of the sliding probe being oriented along the scanning path. The measurement data are shown in Fig. 3.10. The numerical model [3] has been tested on the through-wall hole on the top of the slab as shown in Fig. 3.11. It is worth noting the high accuracy of the numerical method and of the experimental measurements.

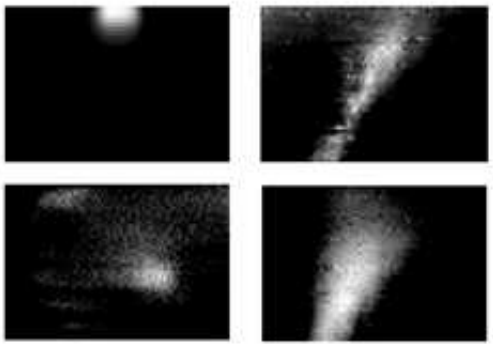

Figure 3.10: Top: Experimental ECT data obtained on the hole (left) and on the defect 1 (right); ECT data on the defect 2 (left) and defect 3 (right). The intensity diagram are referred to the modulus of the measured impedance.

Then we analyzed the defects. The fatigue cracks can be considered with zero thickness and typically perpendicular to the specimen. In order to find the crack plane

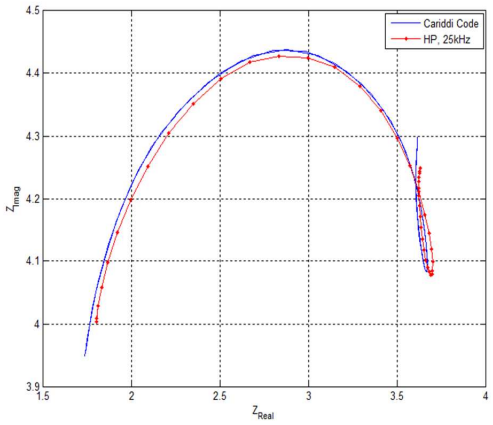

Figure 3.11: Plot of the numerical (-) and experimental (·−) impedance values in the complex plane.

we analyzed the symmetries in the measured response. Finally, the reconstruction was carried out by minimizing an error functional for the real and the imaginary part of the impedance, related to the root mean square error between experimental measurements and simulated signals:

$$\varepsilon_r = \frac{\sqrt{\sum_n (R_n^{calc} - R_n^{meas})^2}}{\sqrt{\sum_n (R_n^{meas})^2}}, \qquad \varepsilon_i = \frac{\sqrt{\sum_n (X_n^{calc} - X_n^{meas})^2}}{\sqrt{\sum_n (X_n^{meas})^2}} \tag{3.2}$$

where $R_n^{meas} + iX_n^{meas}$ is the measured impedance variation due to a crack and $R_n^{calc} + iX_n^{calc}$ $R_n^{calc} + iX_n^{calc}$is the computed impedance variation for each position of the coil along a line parallel to the specimen and to the fatigue crack. Finally, Figs. 3.12 and 3.13 show the reconstructions for the flaws (cases 1 and 2) on the crack plane, while Tab.3.1 shows the associated errors obtained with the two methods. It is worth noting that in both cases the solution provided by the TOPCSA fits the experimental data significantly better than the solution provided by the GA. Moreover, the TOPCSA, by taking into account topological constraints (defect made by several non connected component are "discarded"), provide better approximation of the geometry of a fatigue crack.

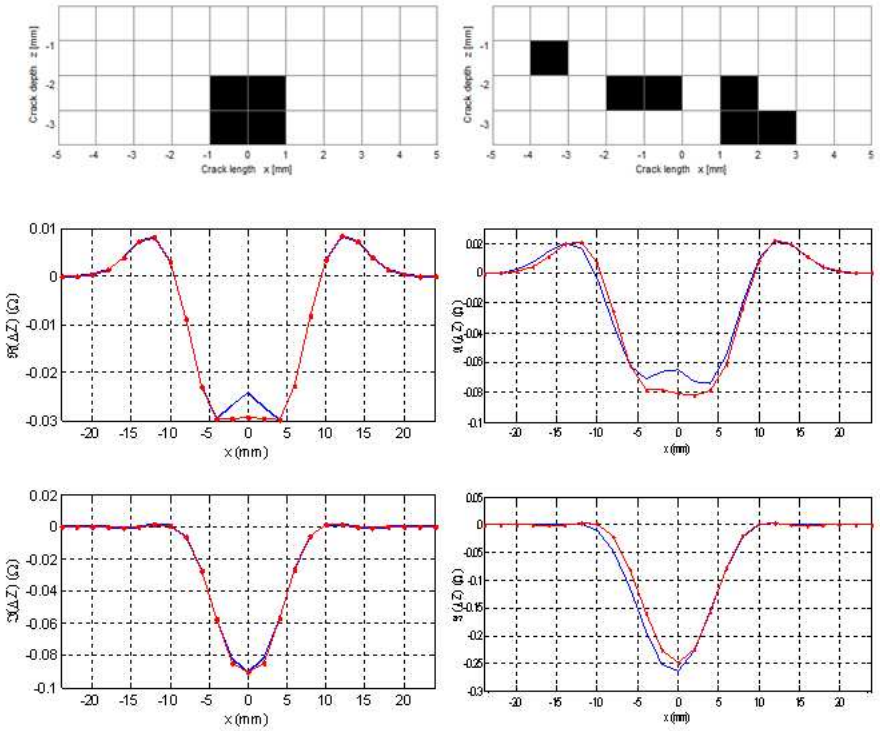

Figure 3.12: Top: Reconstructions obtained with TOPCSA (left) and GA (right) for the defect 1. The black pixels belong to the reconstructed inclusion. Bottom: plot of the experimental (·—) and numerical (-) impedance variation values (real and imaginary part) for each position of the reflection probe on the specimen, obtained after the fitting with TOPCSA (left) and GA (right).

Defect Topcsa	$\varepsilon_r\%$	$\varepsilon_i\%$
1	8.5	2.75
2	10	4.38
Defect GA	$\varepsilon_r\%$	$\varepsilon_i\%$
1	18.3	6.7
2	25.3	23.6

Table 3.1: Errors obtained with TOPCSA (Top)and GA (Bottom) for both the analyzed defects.

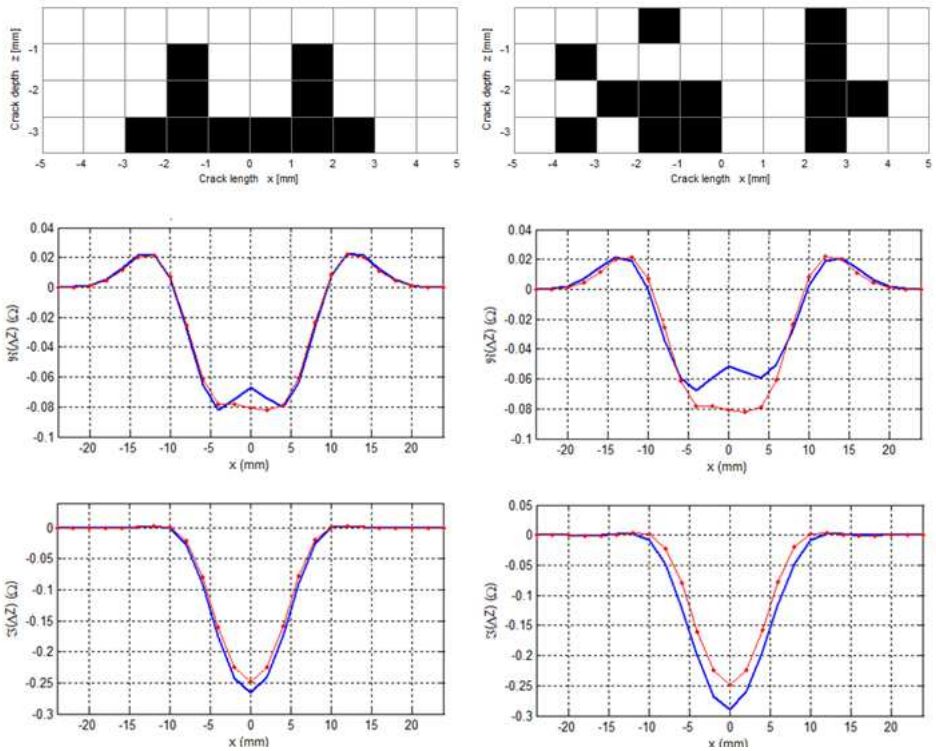

Figure 3.13: Top: Reconstructions obtained with TOPCSA (left) and GA (right) for the defect 2. The black pixels belong to the reconstructed inclusion. Bottom: plot of the experimental ($\cdot-$) and numerical (-) impedance variation values (real and imaginary part) for each position of the reflection probe on the specimen, obtained after the fitting with TOPCSA (left) and GA (right).

3.4.2 3D Reconstructions

In this section we perform a 3D reconstruction, by analyzing not more a crack plane but the whole region scanned by the probe. We analyze an aluminium plate (conductivity $\sigma = 18.30MS/m$, thickness 2mm) with a 5mm×0.2mm though-wall defect in the middle. The algorithms have to chose pixels which are identified in a volume as shown in Fig.3.14 where we chose three cut planes in the y direction in accordance with the measurement data. The defect is localised exactly in the middle, in the plane y=0.

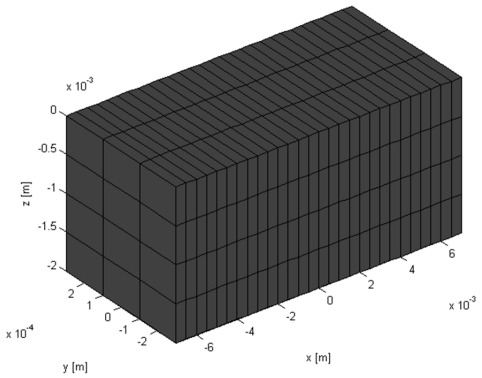

Figure 3.14: Finite element mesh used for the perturbed solution of Cariddi_ECT near the analyzed defect

In the following Figs. 3.15 and 3.16 are shown the reconstructions obtained with the GA algorithm and TOPCSA algorithm.

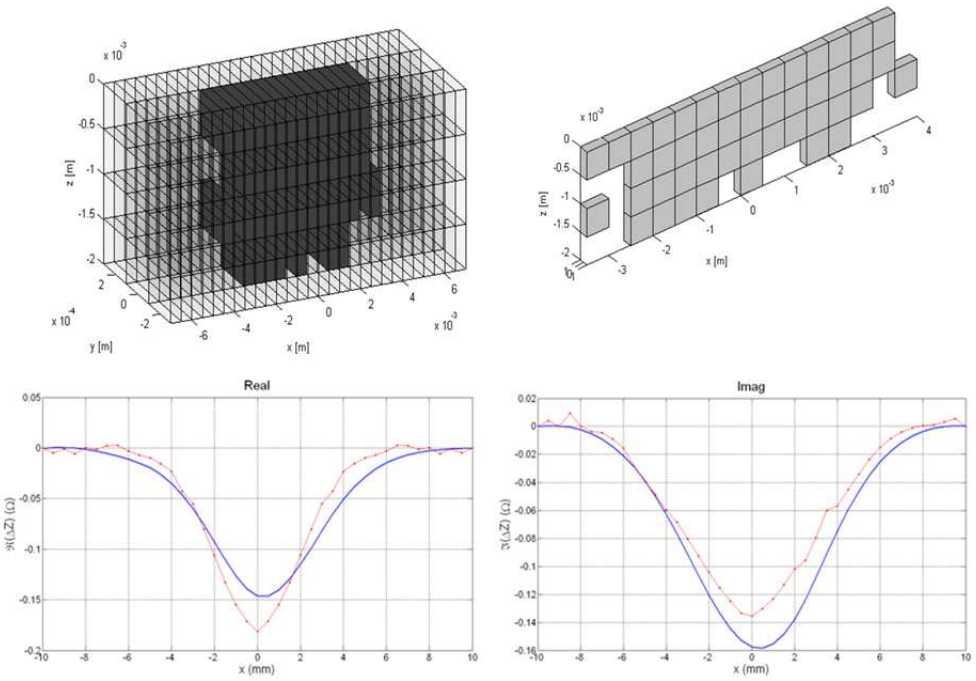

Figure 3.15: Top:3D reconstrution obtained with the GA algoritm. Bottom: plot of the experimental (·—) and numerical (-) impedance variation values (real and imaginary part) for each position of the reflection probe on the specimen.

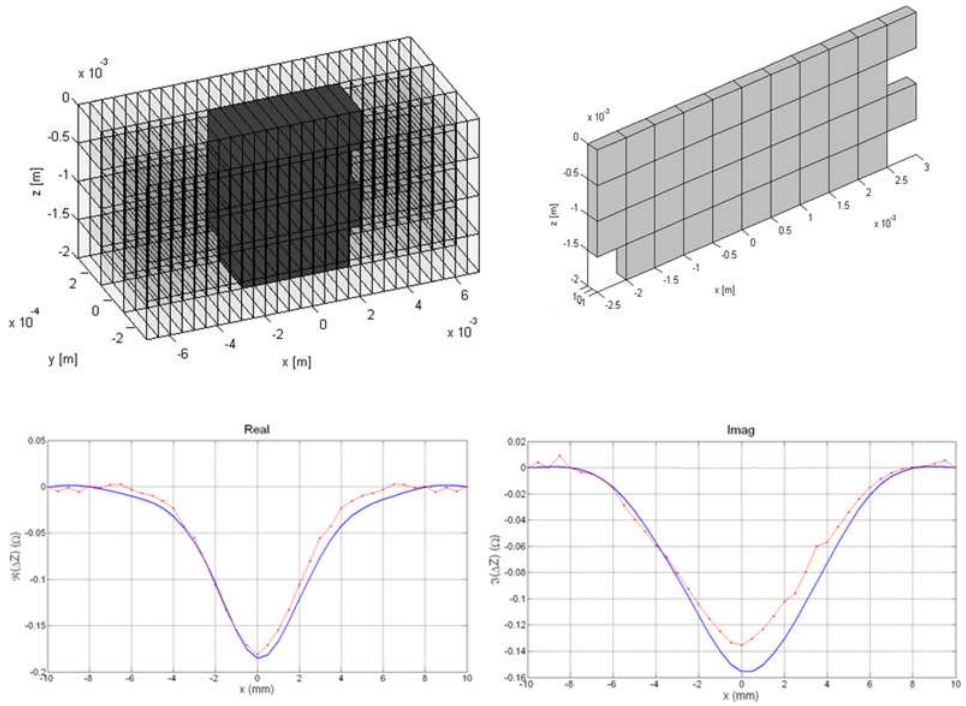

Figure 3.16: Top:3D reconstrution obtained with the TOPCSA algoritm. Bottom: plot of the experimental ($\cdot-$) and numerical (-) impedance variation values (real and imaginary part) for each position of the reflection probe on the specimen.

The errors are shown in the following Tab.3.2. As we expected the performances of TOPCSA are better than GA also when we consider the whole scanning area with 3D reconstructions.

Defect GA	$\varepsilon_r\%$	$\varepsilon_i\%$
	20.43	23.72
Defect Topcsa	$\varepsilon_r\%$	$\varepsilon_i\%$
	12.79	19.07

Table 3.2: Errors obtained with GA (Top) and TOPCSA (Bottom)

3.5 Conclusions

In this chapter we have applied a new iterative topological based algorithm (TOPCSA) to eddy current testing of defects. The method has been compared with a Genetic Algorithm (GA) and experimentally validated [7]. The topological optimization method

takes naturally into account some topological constraints performed significantly better than a classical GA based method for both 2D and 3D reconstructions.

4

Non-iterative Imaging Methods for Electrical Resistance Tomography

This chapter is focused on a comparison between the three non-iterative methods which are the State-of-the-Art of the non-iterative methods. The aim of this comparison is to analyze the performances of the Monotonicity imaging method [8], which has been developed for years in our research group and improved thanks to the work of this thesis with new details that we describe in this chapter. The comparison is carried out in the frame of the Electrical Resistance Tomography (ERT) to detect inclusions in conducting materials. This technique has been considered in a variety of applications covering different fields such as medical applications [52], geophysical prospecting [53], non-destructive testing [54, 55], process tomography [56]. The problem was first formulated mathematically by Calderón [57] as inverse boundary value problem, since the conductivity σ appears as a diffusion coefficient in an elliptic differential equation. A major role is played by the Neumann-to-Dirichlet operator Λ which maps the applied currents f on a body into the boundary (measured) voltages u.

Let $\Omega \subset \mathrm{R}^n$, n ≥ 2 be a simply connected, bounded domain with smooth boundary $\partial\Omega$. When a boundary current $f \in S(\partial\Omega)$ is imposed on $\partial\Omega$ is induced an electrical potential $u \in R(\partial\Omega)$ which is solution of the Neumann problem:

$$\begin{cases} \nabla \cdot \sigma \nabla u = 0 \; in \; \Omega \\ \sigma \frac{\partial u}{\partial n} = f \; on \; \partial\Omega \end{cases} \tag{4.1}$$

where

$$S(\partial\Omega) = \{f \in L^2(\partial\Omega) : \int_{\partial\Omega} f(s)ds = 0\}\text{g} \tag{4.2}$$

$$R(\Omega) = \{u \in H^1(\Omega) : \int_{\partial\Omega} u(s)ds = 0\} \tag{4.3}$$

The conductivity σ is piecewise constant, homogeneous in Ω except for a number p of inclusion B_j, j=1,...,p where σ is assumed to be different from the background:

$$\sigma(r) = \begin{cases} \sigma_0 & r \in \Omega\backslash B \\ \sigma_j & r \in B_j \end{cases} \tag{4.4}$$

and $B = \cup_j B_j$.

The problem is very challenging since the map $\sigma \rightarrow \Lambda$ is nonlinear and the recovery of σ from Λ is ill-posed in the sense of Hadamard. It has been demonstrated that the knowledge of the Neumann-to-Dirichlet map guarantees the uniqueness of the solution of the inverse problem [58]-[62].

Main of the developed algorithms are based on a linearization technique of the operator mapping the resistivity into the boundary data. We refer to [52] for a list of references, also covering other classes of methods such as iterative minimization for various error functionals, which are mainly based on Newton's method.

The iterative methods require the solution of the direct problem for several assigned tentative shapes of the inclusion and can be very expensive in terms of computational cost. Moreover, the convergence cannot be guaranteed.

On the other hand non-iterative methods have attracted a lot of interest because they provide a test for evaluating if a point of the domain (or a subregion) is part or not of the anomaly, regardless other points (or subregions). The test is very cheap from the computational viewpoint because no iterations are necessary and a robust numerical convergence criterion is given for each method, which can be extended to noisy data.

4.1 Monotonicity method

This method is based on the work described in [8, 14, 63, 64, 65]. The method is based on the monotonicity principle of the Neumann-to-Dirichlet operator, that is:

$$\sigma_2(r) \geq \sigma_1(r)\,,\ \forall r \in \Omega \Rightarrow \Lambda_{\sigma_1} \geq \Lambda_{\sigma_2} \tag{4.5}$$

where Λ_{σ_k} is the Neumann-to-Dirichlet map corresponding to σ_k and $\Lambda_{\sigma_1} \geq \Lambda_{\sigma_2}$ means that $\Lambda_{\sigma_1} - \Lambda_{\sigma_2}$ is positive semi-definite.

Monotonicity (4.5) can be easily proved through the variational characterization of the solution of problem (4.1) in term of minimum in $H^1(\Omega)$ of the functional:

$$F_\sigma(u) = \frac{1}{2}\int_\Omega \sigma\ |\nabla u|^2 d\tau - \int_{\partial\Omega} f\,u\,ds \tag{4.6}$$

Moreover, as well known, on the solution u_σ of (4.1) it turns out that:

$$F_\sigma(u) = -\frac{1}{2}\int_{\partial\Omega} f\,u_\sigma\,ds. \tag{4.7}$$

Finally, Monotonicity (4.4) can be obtained as follows:

$$\begin{aligned}
&\langle f, \Lambda_{\sigma_1} f\rangle = \int_{\partial\Omega} f\,u_{\sigma_1}\,ds = -2F_{\sigma_1}(u_{\sigma_1}) \geq -2F_{\sigma_1}(u_{\sigma_2})\\
&= -\int_\Omega \sigma_1\ |\nabla u_{\sigma_2}|^2 dx + 2\int_{\partial\Omega} f\,u_{\sigma_2}\,ds\\
&\geq -\int_\Omega \sigma_2\ |\nabla u_{\sigma_2}|^2 dx + 2\int_{\partial\Omega} f\,u_{\sigma_2}\\
&= -2F_{\sigma_2}(u_{\sigma_2}) = \langle f, \Lambda_{\sigma_2} f\rangle\,.
\end{aligned} \tag{4.8}$$

where we have taken into account the assumption $\sigma_2 > \sigma_1$ in the second inequality. It is worth noting that from the physical standpoint, (4.6) means that if the conductivity of the considered material increases pointwise, then the Ohmic losses for a prescribed boundary current f increase.

Monotonicity (4.5) can be easily turned into a fast imaging method [8]. Indeed, let us consider a two-phases problem, i.e. the shape identification problem consisting in retrieving a homogeneous unknown anomaly B hosted in the homogeneous domain Ω. In other terms, we are assuming that all the σ_j in (4.4) are equal. In addition, we assume that the conductivity of the anomaly is smaller than that of the background.

Let us now consider a test anomaly occupying the region B_{test}. Thanks to (4.5), if the test domain is contained in the unknown anomaly B, then the conductivity of the test anomaly is (pointwise) greater or equal to that of the unknown anomaly and $\Lambda_B \geq \Lambda_{B_{Test}}$($\Lambda_B$ is the Neumann-to-Dirichlet map related to B and $\Lambda_{B_{Test}}$ is the Neumann-to-Dirichlet map related to B_{test}). Consequently, it holds that:

$$\Lambda_B \geq \Lambda_{B_{Test}} \; false \; \Rightarrow \; B_{test} \not\subset B. \tag{4.9}$$

Test (4.9) is the basis for the fast imaging method. Indeed, once the data Λ_B has been measured, for a given (and known) test anomaly B_{test} it is possible to ascertain if it is part or not of the unknown anomaly B by simply checking the sign of the eigenvalues of $\Lambda_B - \Lambda_{B_{Test}}$. Then, the same test, repeated for different positions and shapes of the test anomaly, provides the shape of B. It is worth noting that Λ_B is the data corresponding to the unknown B, whereas $\Lambda_{B_{Test}}$ corresponds to the known B_{test} and it can be either measured experimentally or evaluated numerically [14].

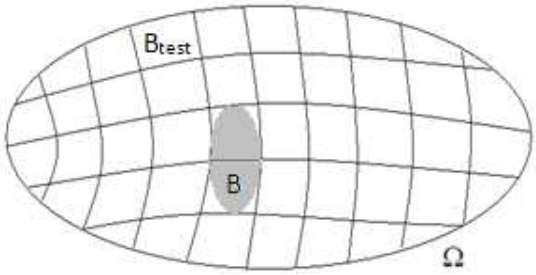

Figure 4.1: The domain Ω the inclusion B and a possible partitioning of in terms of the test subdomains B_{Test}

The imaging method checks (4.9) for different trial anomalies, for instance those obtained by partitioning the domain Ω in non-overlapped subsets (see Fig. 4.1). After evaluating through (4.9) if a generic test domain from this partition is included or not of the unknown anomaly B, the reconstruction is obtained as the union of the subsets that result to be included in B.

As well known from perturbation theory, the eigenvalues of the symmetric matrix $\underline{\underline{A}} + \underline{\underline{E}}$ differ from those of $\underline{\underline{A}}$ of at most the L^2-norm of the perturbation matrix $\underline{\underline{E}}$. Concerning the imaging algorithm, this means that if the L^2-norm of the measurement noise is larger than all negative eigenvalues, test (4.9) is unreliable and it may provide false detections of anomalies (see Fig.4.2).

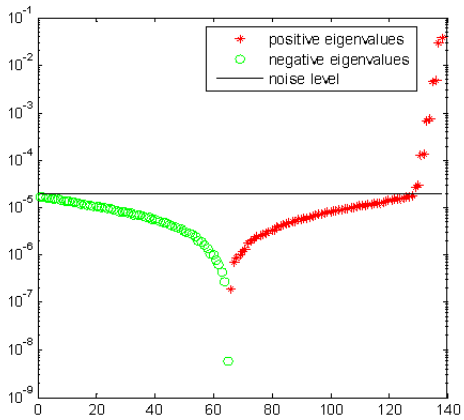

Figure 4.2: Eigenvalues of $\Lambda_B - \Lambda_{B_{Test}}$ in a logarithmic scale for a test anomaly external to the inclusion. (o) is the plot of the absolute value of the negative eigenvalues and (*) is the plot of the positive ones. The continuous line (-) is the noise level calculated with the L^2-norm of the noise matrix.

From extensive numerical tests, we found effective in improving the immunity to the noise to replace (4.9) with:

$$\Lambda_B - \Lambda_0 \geq C\,(\Lambda_{\ B_{Test}} - \Lambda_0)\ \ false\ \Rightarrow\ B_{test} \not\subset B \tag{4.10}$$

where C is a proper constant and Λ_0 is the Neumann-to-Dirichlet map when no anomalies are present.

Numerical simulations showed that the value of C depends on the noise level but is only weakly dependent on the shape of the anomaly. Therefore, the value of C can be a priori evaluated on some test configurations. Specifically, C is chosen numerically in order to keep the magnitude of the smaller eigenvalues above the noise level when the inclusion is outside the anomaly as shown in Fig.4.3.

It is worth noting that if the value of the constant C is too high, the inclusion condition can be not verified also in the regions that belong to the anomaly, so the choice of C has to be properly carried out.

4.2 Factorization method

The second algorithm is based on the Factorization method proposed by Brühl and Hanke in [9, 66] starting from an idea of Colton and Kirsch [67, 68] developed in

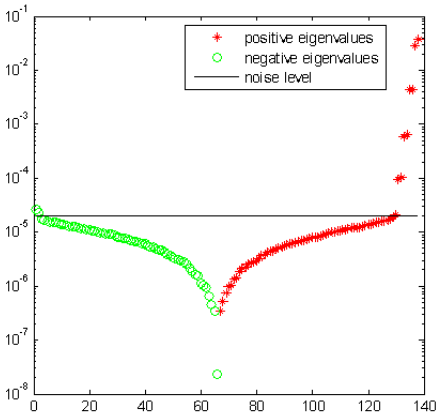

Figure 4.3: Eigenvalues of $\Lambda_B - \Lambda_{B_{Test}}$ in a logarithmic scale for a test anomaly external to the inclusion. The value chosen for C from simulations is 50. (o) is the plot of the absolute value of the negative eigenvalues and (*) is the plot of the positive ones. The continuous line (-) is the noise level calculated with the L^2 norm of the noise matrix.

the frame of inverse scattering problems. This method requires the knowledge of the Neumann-to-Dirichlet map Λ_0 related to the background, i.e. when no inclusions are present in Ω, and the measured map Λ corresponding to the actual configuration under testing. To be more specific, Λ_0 maps the applied currents $f \in S(\partial\Omega)$ on the boundary $\partial\Omega$, into the boundary voltages $u_0|_{\partial\Omega}$ where $u_0 \in R(\Omega)$ is the solution of:

$$\begin{cases} \nabla \cdot \sigma_0 \nabla u_0 = 0 \; in \; \Omega \\ \sigma_0 \frac{\partial u_0}{\partial n} = f \; on \; \partial\Omega \end{cases} \tag{4.11}$$

A primary quantity for the imaging algorithm is the solution of the following homogeneous (constant conductivity) problem:

$$\begin{cases} \nabla^2 G_{z,d} = \nabla^2 D_{z,d} \quad in \; \Omega \backslash \{z\} \\ \frac{\partial G_{z,d}}{\partial n} = 0 \quad on \; \partial\Omega \end{cases} \tag{4.12}$$

where $D_{z,d}$ is the scalar dipole potential:

$$D_{z,d}(x) = \frac{(z-x)\cdot d}{2\pi \left|x-z\right|^2}, \; x \neq z. \tag{4.13}$$

where $d \in \mathrm{R}^2$. Function $D_{z,d}$ represents the scalar potential for a dipole located in z and directed along the direction given by d.

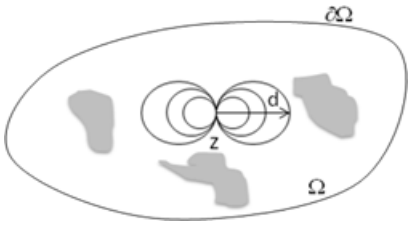

Figure 4.4: Equipotential lines of the dipole function $D_{z,d}$ in the domain Ω.

The imaging algorithm is based on the following result [9, 66]:

$$z \in B \quad \Leftrightarrow \quad g_{z,d} = G_{z,d}|_{\partial\Omega} \in R\left(\left(\Lambda - \Lambda_0\right)^{1/2}\right). \tag{4.14}$$

In other words, a point z belongs to the inclusion B if and only if the trace $g_{z,d}$ belongs to the range of range of the operator $(\Lambda - \Lambda_0)^{1/2}$. By exploiting the Picard criterion, condition (4.14) is equivalent to:

$$z \in B \textit{ if and only if } \sum_{k=1}^{\infty} \langle g_{z,d}, \nu_k \rangle^2 / \lambda_k < +\infty \tag{4.15}$$

where the ν_k's and λ_k's are the eigenfunctions and the eigenvalues of $\Lambda - \Lambda_0$. For understanding the imaging algorithm, at least partially, we notice that for prescribed f in (4.1) and (4.11), the difference between the boundary potentials $u|_{\partial\Omega}$ and $u_0|_{\partial\Omega}$, $h = u|_{\partial\Omega} - u_0|_{\partial\Omega}$, is a function from the range of the operator $\Lambda - \Lambda_0$, i.e.:

$$h = (\Lambda - \Lambda_0) f \tag{4.16}$$

that is the trace on $\partial\Omega$ of $w = u - \quad u_0$ that is an harmonic potential in $\Omega \backslash \overline{B}$. In addition the flux ∂w/∂n is equal to zero on $\partial\Omega$. Therefore, w is uniquely determined as the solution of the Cauchy problem:

$$\begin{cases} \nabla^2 w = 0 \textit{ in } \Omega \backslash \overline{B} \\ \frac{\partial w}{\partial n} = 0 \textit{ on } \partial\Omega \\ w = h \textit{ on } \partial\Omega \end{cases} \tag{4.17}$$

Therefore, it is clear that if $g_{z,d}$, that is the trace of $G_{z,d}$ in (4.14), is an element of the range of the operator $\Lambda - \Lambda_0$ then, $G_{z,d}$ satisfies (4.12) and, consequently, $z \in$B. The converse is not true for the operator $\Lambda - \Lambda_0$ and, therefore, an imaging algorithm testing condition $g_{z,d} \in R\,(\Lambda - \Lambda_0)$ may provide a smaller image of the anomalies. This is not

the case of the square root $(\Lambda - \Lambda_0)^{1/2}$ where, thanks to (4.15), an imaging algorithm testing $g_{z,d} \in R\left((\Lambda - \Lambda_0)^{1/2}\right)$ produce, at least theoretically and with complete and noise-free data, the exact shape on the anomaly.

From the practical viewpoint, to apply test (4.15), it is important to realize that the convergence of the series has to be evaluated from the available data: we have at our disposal only a finite number of elements of the series that, in addition, are known only in an approximate way. The convergence of the series (4.15) can be evaluated by comparing the decay of the terms $\langle g_{z,d}, \nu_k \rangle^2$and λ_k. As example (see Fig. 4.5) when $z \in B$ it turns out that the plot of $\langle g_{z,d}, \nu_k \rangle^2$ is steeper than the plot of the λ_k's. The converse is true when z is not part of the inclusion.

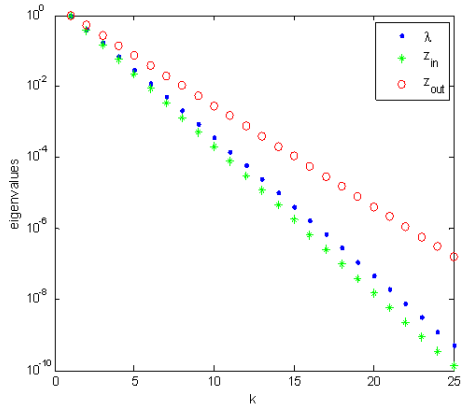

Figure 4.5: Plot of $\langle g_{z,d}, \nu_k \rangle^2$ when z is internal to the inclusion (*) and when z is external to the inclusion (o), together with the eigenvalues ($\cdot$). The plots are normalized.

It is well known that the eigenvalues λ_k's exhibit an exponential decay. By means of a least square approach it is possible to estimate the decay parameters c and q from the first m_0 eigenvalues λ_k:

$$\log \lambda_k \approx c + k \log q \tag{4.18}$$

Similarly it possible to apply the same concept to $\langle g_{z,d}, \nu_k \rangle^2$ in order to obtain the decay parameters ψ_z and ϕ_z:

$$\log \langle g_{z,d}, \nu_k \rangle^2 \approx \psi_z + k \log \phi_z \tag{4.19}$$

In terms of the decay parameters (numerical range criterion) test (4.15) becomes:

$$z \in B \text{ if and only if } \psi_z < q. \tag{4.20}$$

In case of noisy data, the trends of both $\langle g_{z,d}, \nu_k \rangle^2$ and λ_k are perturbed (see Fig. 6). Assuming the noise is additive, we may represent it as a perturbation operator E that sums to Λ and, therefore, to $\Lambda - \Lambda_0$. From the perturbation theory, we know that the eigenvalues of the new map $\Lambda - \Lambda_0 + E$ differ from the unperturbed ones by at most δ that is the L^2 norm of the operator E.

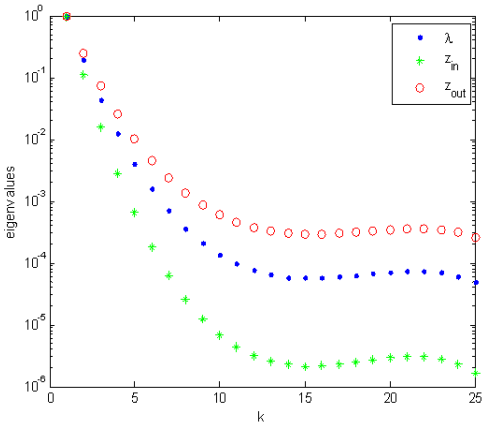

Figure 4.6: Plot of $\langle g_{z,d}, \nu_k \rangle^2$ when z is internal to the inclusion (*) and when z is external to the inclusion (o), together with the eigenvalues ($\cdot$). The plots have been obtained in the presence of additive random noise.

In order to minimize the effect of noise it is necessary to reduce m_0 that is the maximum number of terms of the series (4.15) that are considered in decay parameters in (4.17) and (4.18). Specifically, we retains only the terms such that condition $\lambda_k > \delta$ is satisfied. For example in Fig.4.6 only m_0=5 eigenvalues can be used.

4.3 MUSIC method

The third method is an algorithm based on the MUltiple SIgnal Classification method (MUSIC). The MUSIC algorithm has been originally developed to locate point scatterers from multistatic measurements in wave propagation inverse problems [10]. Here we briefly describe this method as originally developed for the scalar wave-propagation equation. Let us consider N elementary antennas located at the spatial positions R_1,

$\ldots$,R_N, in a material that is homogeneous apart from M small anomalies. Let X_1, $\ldots$, X_M be the spatial position of the anomalies. The (scalar) unperturbed field ψ_j^{inc} evaluated at the point x and due to the $j-$th antenna can be evaluated through the appropriate Green function as:

$$\psi_j^{inc} = G(x, R_j) i_j. \tag{4.21}$$

where i_j is the input current applied to the antenna.

Assuming the interactions between the M scatterers are negligible, the field $\psi_{j,m}^{Sc}$ scattered by the $m-$th anomaly is given by:

$$\psi_{j,m}^{Sc} = G(x, X_m) r_m \psi_j^{inc}(X_m), \tag{4.22}$$

where r_m is reflection coefficient of the scatterer. The field received by the $i-$th antenna is given by the superposition of the elementary fields given by (4.22) evaluated at X_i:

$$v_i = \sum\nolimits_m G(X_i, X_m) r_m G(X_m, R_j) e_j. \tag{4.23}$$

From (4.23) it is possible to recognize the multistatic response matrix H:

$$H_{ij} = \sum\nolimits_m G(R_i, X_m) r_m G(X_m, R_j) \tag{4.24}$$

that relates the applied input to the measured output. In compact form we have:

$$\underline{\underline{H}} = \underline{\underline{GRG}}^T \tag{4.25}$$

where the matrices G and R are defined as follows:

$$\underline{\underline{G}} = \begin{bmatrix} G(R_1, X_1), \ldots G(R_1, X_M) \\ \vdots \\ G(R_N, X_1), \ldots G(R_N, X_M) \end{bmatrix} \tag{4.26}$$

$$\underline{\underline{R}} = diag\left\{r_1, r_2, ...r_m\right\} \tag{4.27}$$

The matrix H is symmetric and for $N > M$ its null space is not trivial. It is possible to consider its singular value decomposition:

$$\underline{\underline{H}} = \underline{\underline{U\Sigma V}}^H \tag{4.28}$$

where $\underline{\underline{U}}$ and $\underline{\underline{V}}$ are N×N orthonormal matrices, $\underline{\underline{\Sigma}} = diag\{\sigma_1, ..., \sigma_N\}$ with $\sigma_1 \geq \sigma_2 \geq \ldots \geq \sigma_M > 0$ and $\sigma_{M+1} = \sigma_{M+2} = \sigma_N = 0$. Let U_0 be the last L columns of U related to the vanishing singular values $\sigma_{M+1}, \ldots, \sigma_N$. It follows that:

$$\underline{\underline{0}} = \underline{\underline{U}}_0^H \underline{\underline{GRG}}^T. \tag{4.29}$$

By exploiting that R is invertible and G is full (columns) rank, we have that:

$$\underline{\underline{U}}_0^H \underline{\underline{G}} = 0, \tag{4.30}$$

i.e.

$$\underline{\underline{U}}_0^H \underline{\underline{\Gamma}}(X_m) = 0, \ m = 1, ..., M \tag{4.31}$$

where

$$\underline{\underline{\Gamma}}(X) = \begin{bmatrix} G(R_1, X) \\ \vdots \\ G(R_N, X) \end{bmatrix} \tag{4.32}$$

Summing up, the position of the scatterers can be found through the peaks of:

$$P_{MUSIC}(X) = \frac{1}{\left\| \underline{\underline{U}}_0^H \underline{\underline{\Gamma}}(X) \right\|}. \tag{4.33}$$

In the framework of ERT, it has been observed [52, 66, 69, 71, 72] that there is a strong connection between the Factorization and the MUSIC methods. Indeed, in [71] it was proved that if the anomalies have radii proportional to a small parameter ε, then:

$$\Lambda_\varepsilon - \Lambda_0 = \varepsilon^2 \underline{\underline{K}} + o\left(\varepsilon^2\right), \text{ for } \varepsilon \to 0 \tag{4.34}$$

Λ_ε is the Neumann-to-Dirichlet map for a given ε and K, as in the case of MUSIC, has a rank equal to the number of anomalies M. Moreover, the range of K is spanned by the functions $g_{X_m,d}$, $m = 1, ..., M$ defined in the previous section. Within approximation (4.32) the ranges of K, $\Lambda_\varepsilon - \Lambda_0$ and $(\Lambda_\varepsilon - \Lambda_0)^{1/2}$ coincide and (4.33) can be replaced by:

$$\cot\theta(z) = \left\|(1 - \underline{\underline{P}})g_{z,d}\right\| / \left\|\underline{\underline{P}}g_{z,d}\right\| \tag{4.35}$$

where P is the orthoprojector operator in the null space of $\Lambda_\varepsilon - \Lambda_0$.

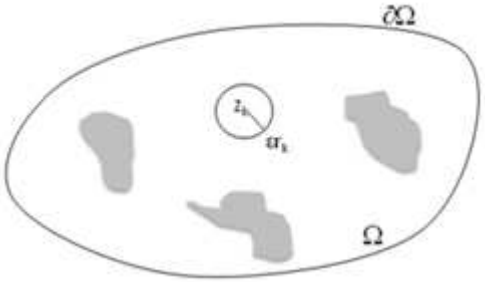

Figure 4.7: A point z_k of Ω surrounded by a circle of radius ϵr_k.

Geometrically, θ represents, the angle between $g_{z,d}$ and the range of Λ_ε-Λ_0. By construction $\cot\theta(z)$ is very large when z is inside an inclusion and the peaks of $\log\cot\theta(z)$ can be used to find an approximate location of the cavities. In the presence of noise having a level of δ the orthoprojector P is related to the linear space spanned by the eigenvectors of $\Lambda_\varepsilon - \Lambda_0$ whose corresponding eigenvalues are greater than the noise level δ.

4.4 2D Numerical Examples

In this section we present a comparison among the three fast imaging methods described in the previous section. We propose three different examples related to industrial and biomedical applications. At the discrete level, i.e. when the Neumann-to-Dirichlet map is represented through a matrix, the noise model is:

$$\tilde{\Lambda}_{ij} = \Lambda_{ij} + N_{ij} \cdot \xi, \tag{4.36}$$

where $\tilde{\Lambda}_{ij}$is the noisy Neumann-to-Dirichlet map, Λ is the noiseless Neumann-to-Dirichlet map, Nis a normalized noise having entries uniformly distributed in (-δ, +δ) and $\xi = \max_{i,j} \left|(\Lambda - \Lambda_0)_{i,j}\right|$. The number of applied currents is equal to 60. The values chosen for δ are 0.001 and 0.01. These values are realistic from an experimental point of view and, moreover, are compatible with the sought resolution. The constant C in the Monotonicity method is 50 for δ=0.001 and 100 for δ=0.01. We consider inclusions in a disk of unitary radius. The first example presents a single anomaly, the second example two anomalies whereas the third example concerns the treatment of a three phases material. In this latter case the monotonicity has been applied twice for retrieving the two phases that are different from the background.

4.4.1 First Numerical Example

The first example refers to an industrial application consisting of the identification of a defect (1S/m almost insulating) in a copper background (58MS/m). The shape of the inclusion is shown in Fig.4.8, whereas the related reconstructions are shown in Fig.4.9. From Fig.4.9 it is we notice that the reconstructions performed with the Factorization method and the Monotonicity method are quite good.

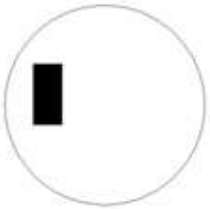

Figure 4.8: A rectangular inclusion with aspect ratio 3:1 in a circle domain.

On the other hand, the MUSIC method underestimates the shape because of the underlying hypothesis of small inclusions. The computational time for the inversions is the same for both the Factorization and the MUSIC methods; it concerns the evaluation of the dipole function $D_{z,d}$ on every node of the mesh used during the inversion. On the other hand, the Monotonicity algorithm requires test (4.15) to be applied to each region B_k. The estimated computational time for the inversions is about 60s for the Factorization and MUSIC methods and about 15s for the Monotonicity method.

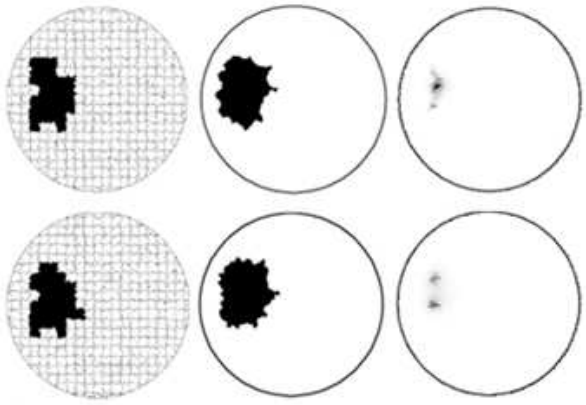

Figure 4.9: From left to right: reconstruction by means of the Monotonicity method, the Factorization method and the MUSIC method. Noise level: δ =0.001 (top) and δ =0.01 (bottom). In the Monotonicity method the reconstructions are shown together with the test subdomains.

4.4.2 Second Numerical Example

The second example refers to an industrial application consisting of the identification of low conductivity (1S/m) inclusions in an aluminum background (38 MS/m). Similarly to the previous example, the reconstructions are quite satisfactory for both the Monotonicity and Factorization methods, whereas the MUSIC method fails in detecting these "non small" anomalies.

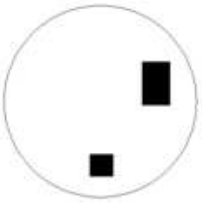

Figure 4.10: A rectangular inclusion with aspect ratio 2:1 and a square inclusion in a circle domain.

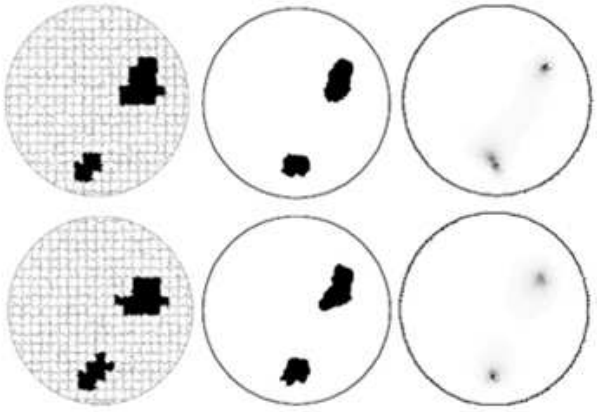

Figure 4.11: From left to right: reconstruction by means of the Monotonicity method, the Factorization method and the MUSIC method. Noise level: δ =0.001 (top) and δ =0.01 (bottom). In the Monotonicity method the reconstructions are shown together with the test subdomains.

4.4.3 Third Numerical Example

The third example (see Fig.4.12) concerns a biomedical application inspired to the reconstruction of the heart and two lungs with conductivities 0.5S/m and 1.2S/m respectively, in a diastolic configuration, with a background conductivity equal to 1S/m. The three "anomalies" have conductivities that are greater (lung) and smaller (heart) than that of the background. We notice that the Monotonicity method has been originally proposed in [8] for two-phases problems. Here, we propose to apply it twice: first for retrieving the heart (conductivity smaller than that of the background) and then for retrieving the lungs (conductivity greater than that of the background).

Figure 4.12: Two rectangular inclusions (lungs) with aspect ratio 3:1 and a square inclusion (heart) in a disk.

Specifically, we introduce two families of test anomalies. A first family is for detecting the presence of the heart and is made by anomalies whose conductivities are equal to that of the background apart from one test subdomain where the values is that of

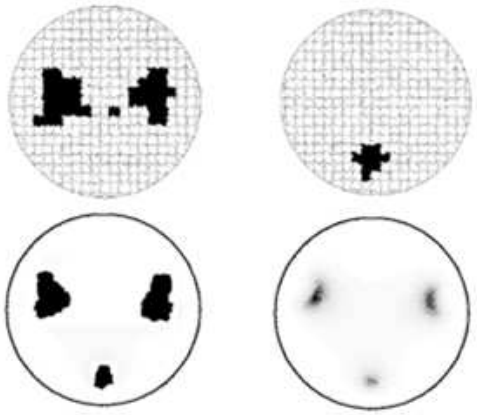

Figure 4.13: Reconstruction with δ =0.001: Monotonicity method applied to retrieve the lungs (top-left) and Monotonicity method applied to retrieve the heart (top-right), Factorization method (bottom-left), MUSIC method (bottom-right).

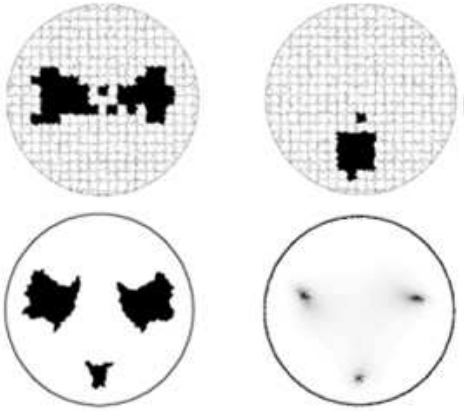

Figure 4.14: Reconstruction with δ =0.01: Monotonicity method applied to retrieve the lungs (top-left) and Monotonicity method applied to retrieve the heart (top-right), Factorization method (bottom-left), MUSIC method (bottom-right).

the heart (0.5S/m). The second family differs from the first one in the value of the conductivity in the test subdomain, equal to that of the lungs (1.2S/m). The numerical results are shown in Fig.4.14. In both cases, the reconstruction with the Monotonicity method is shown in terms of an image for the lungs and one image for the heart. The estimated computational time for the inversions is the same as the previous case for the Factorization and MUSIC method, while for the Monotonicity method it is doubled because of the application of two sets of test anomalies.

4.5 3D numerical examples

In this section we show numerical examples regarding applications in the field of process tomography [73]. We simulate the experimental acquisition of boundary voltage to obtain a finite dimensional approximation of the Neumann to Dirichlet map by imposing a set of boundary currents on a given number of electrode uniformly distributed on the analyzed tridimensional domain(see Fig.4.15). We use 75 electrodes and the same noise levels (δ=0.001 and δ=0.01) of the 2D examples. The constant C in the Monotonicity method is 35 for δ=0.001 and 70 for δ=0.01.

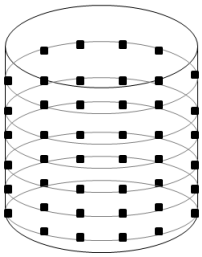

Figure 4.15: Simulated experiment setup. The black cubes are representative of the electrodes used to calculate the finite dimensional approximation of the Neumann to Dirichlet map.

The simulated experiments consist of placing plastic bottles ($\sigma = 10^{-9}$S/cm at 20℃) which are filled with tap water ($\sigma = 10^{-4}$S/cm at 20℃) in two different geometric configurations.

4.5.1 First 3D numerical example

The first 3D example is shown in next Fig.4.16 and the reconstructions in Fig.4.17. For these 3D reconstructions the estimated computational time for the inversions is 80s for the Factorization and MUSIC methods and 20s for the Monotonicity method, this increasing in time computation by respect the 2D case is obviously due to a major number of nodes in the finite element mesh for the evaluation of the dipole function of the Factorization and MUSIC methods, and a major number of regions in this 3D case for the Monotonicity method.

Figure 4.16: Configuration under investigation. The considered domain is a cylinder of height h=2m and radius r=1m. The inclusion is represented by a rectangular prism of dimensions 0.2×0.2×0.4.

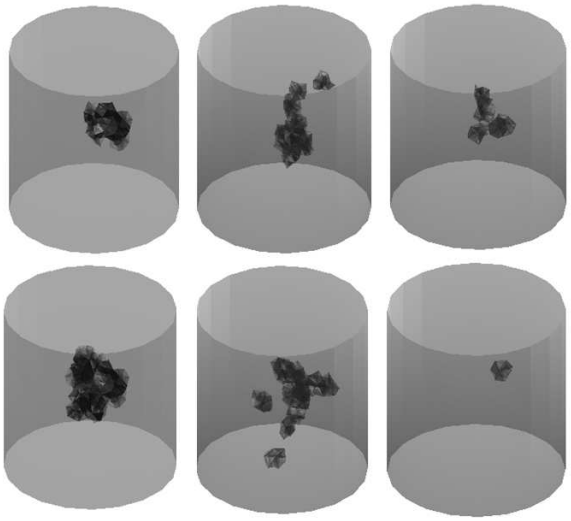

Figure 4.17: From left to right: Simulations obtained with Factorization method, MUSIC method and Monotonicity method with δ=0.001 (top) and with δ=0.01 (bottom).

4.5.2 Second 3D numerical example

The second 3D example is shown in next Fig.4.18 and the reconstructions in Fig.4.19. The reconstruction obtained with Monotonicity method are quite good while here is evident for the MUSIC method the underestimation of the inclusions as in the 2D cases. For the 3D inclusions the Factorization method seems to be more sensitive to noise by respect the 2D cases.

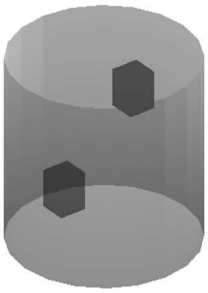

Figure 4.18: Configuration under investigation. The considered domain is a cylinder of height h=2m and radius r=1m. The inclusion is represented by rectangular prisms of dimensions 0.2×0.2×0.4.

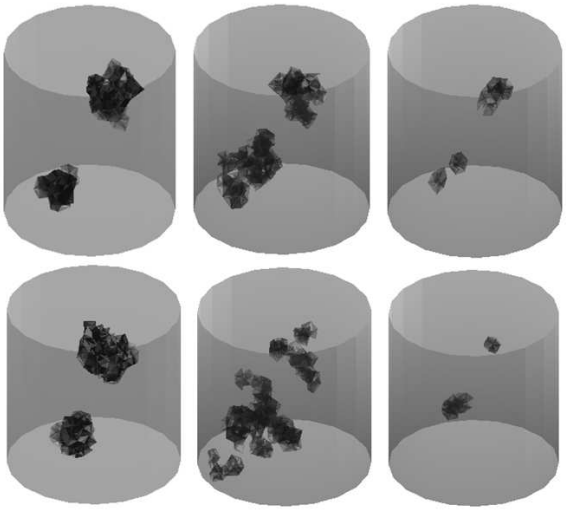

Figure 4.19: From left to right: Simulations obtained with Factorization method, music method and Monotonicity method with δ=0.001 (top) and with δ=0.01 (bottom).

4.6 Conclusions

In this chapter three non-iterative methods for locating inclusion in Electrical Resistance Tomography have been presented. These methods are candidate for real-time imaging because no iterations are required to get the shape of the inclusion. The Monotonicity and Factorization methods provide satisfactory reconstructions for a reasonable values of the noise level for both 2D and 3D reconstructions. They work for non "small" and multiple anomalies, as well. On the contrary, MUSIC achieve worse performances because it relies on the assumption of "small" anomalies. Moreover, in this section we have extended the Monotonicity method from two phases problems to

more complicated configurations consisting of more than two phases with conductivities which can be higher and lower than that of the background and improved the immunity to noise [11, 12, 13].

5

Non Iterative Imaging Method for Eddy Current Tomography

5.1 Introduction

In this chapter we present the first experimental validation of the Monotonicity imaging method presented in the previous chapter through the eddy current tomography [14]. Here we exploit the monotonicity property of the real part of the measured impedance matrix [63]. As we showed in the previous chapter this method was initially developed for elliptic problems such as electrical resistance tomography [8], than has been extended to parabolic problems such as the eddy current testing in both low frequency (large skin depth) [63] and high frequency (skin depth negligible with respect to the relevant dimension) [64, 65], but has never been applied on experimental data. A key role in eddy current tomography is the reconstruction of the resistivity profile of the specimen under test, starting from the measurement data, through the solution of an inverse problem. The measured data consist of measurements of the impedance matrix (self and mutual impedances) between the coils of the array (see Fig.5.1).

The identification of the conductivity distribution inside a material is seriously affected by the inherently ill-posed and nonlinear nature of the eddy currents inverse problem (see [39]-[41] for mathematical issues). First and foremost, the ill-posedness translates into low sensitivity measurements, i.e. different resistivity distributions produce similar measurements and, in addition, the nonlinearity requires sophisticated inversion algorithms. As we showed in the previous chapters the imaging methods can

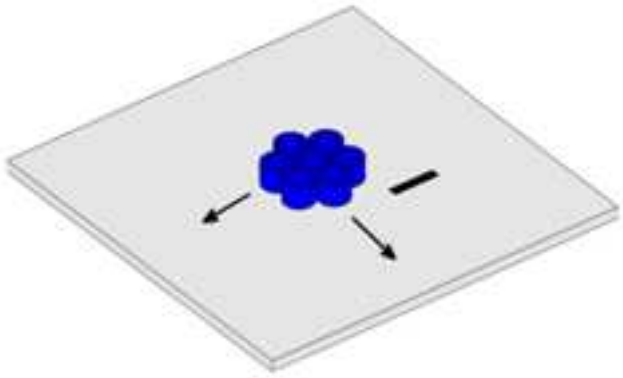

Figure 5.1: The planar surface to be investigated (specimen) together with a probe made by an array of seven coils and a rectangular defect.

be divided in iterative and non-iterative (direct). As main drawbacks, the iterative methods require the solution of the direct problem for several assigned tentative shapes of the inclusion and this can be very expensive in terms of computational cost. Moreover, the convergence cannot be guaranteed. On the other hand non-iterative methods have attracted a lot of interest because they provide a test for evaluating if a point of the domain (or a subregion) is part or not of the anomaly, regardless other points (or subregions). The test is very cheap from the computational viewpoint because no iterations are necessary. The aim of this chapter is to show that is possible to apply a real time imaging method to the eddy current inverse problem if we design correctly the measurement system in accordance with the noise level. Numerical simulations of the direct problem with the numerical code CARIDDI_ECT [2, 3] have been exploited to check numerically if a given probe was able to guarantee appropriate reconstructions. The Monotonicity imaging method is here applied to identify the conductivity profile of several benchmarks. We show that with a designed measurement system through direct simulations, the Monotonicity imaging method provides the conductivity profile of the device under test in real time with no errors.

5.2 Monotonicity principle for Eddy Current Testing

In this section we briefly describe the monotonicity principle for the real part of the measured impedance matrix (self and mutual impedances between pairs of coils of the

array shown in Fig.5.1). In the low frequency limit, the impedance matrix admits the following expansion:

$$\mathbf{Z}_D^{coil} = \mathbf{R}_0 + j\omega\mathbf{L}_0 + \omega^2\mathbf{P}_D^{(2)} + j\omega^3\mathbf{P}_D^{(3)} + O(\omega^4) \tag{5.1}$$

that is valid as long as the frequency is enough low so that the 4^{th} and higher order terms in (5.1) are negligible. We mention that all matrices appearing in (5.1) are real and symmetric. Matrix $\mathbf{P}_D^{(2)}$, which contributes to the real part of the impedance matrix, plays a key role because of its monotonicity property [63]. First we demostrate the monotonicity property for the operator $\mathbf{R}_\eta$ which represent the resistance matrix associated to the conductive region and later we extend the monotonicity property to the second order term $\mathbf{P}_D^{(2)}$. The operator $\mathbf{R}_\eta$ is defined through the ohmic power dissipated for a given resistivity η:

$$\mathbf{P}_\eta = \int_D \eta \left\|\mathbf{J}\right\|^2 dV = \mathbf{I}^{\mathbf{T}}\mathbf{R}_\eta\mathbf{I} \tag{5.2}$$

If we refer to the electric vector potential ($\mathbf{J} = \nabla \times \mathbf{T}$) based formulation for the direct eddy current problem, the vector potential $\mathbf{T}$ is given by the solution of the following variational formulation:

$$\textit{find } \mathbf{T} \in A^I \textit{ such that } \int_D \eta \left\|\nabla \times \mathbf{T}\right\|^2 dV \textit{ is minimum} \tag{5.3}$$

where

$$A^I \hat{=} \left\{ \mathbf{T} \in A | \int_{S_k} \nabla \times \mathbf{T} \cdot \hat{\mathbf{n}} dS = i_k,\ k = 1, \ldots, M \right\} \tag{5.4}$$

with i_k we indicate the imposed currents through the electrodes on the conductive region to calculate the resistance matrix.

Proposition 1. $\eta_1 \geq \eta_2 \Rightarrow \mathbf{R}_1 \geq \mathbf{R}_2$ where $\mathbf{R}_1$ is the resistance matrix related to η_1, $\mathbf{R}_2$ is the resistance matrix related to η_2 and $\mathbf{R}_1 \geq \mathbf{R}_2$ means that $\mathbf{R}_1 - \mathbf{R}_2$ is a positive semi-definite matrix, i.e. $\mathbf{x}^T \left(\mathbf{R}_1 - \mathbf{R}_2\right) \mathbf{x} \geq 0$, $\forall \mathbf{x}$.

Let $\mathbf{T}_1$ and $\mathbf{T}_2$ be defined as the solution of (5.3) when the column vector $\mathbf{I}$ of the electrode currents is given and the resistivities are η_1 and η_2, respectively. Then it

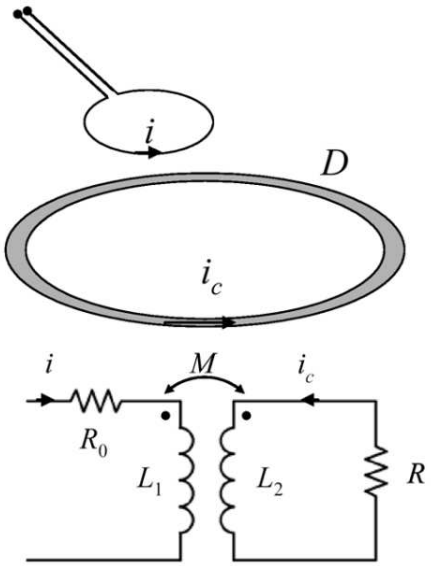

Figure 5.2: Top: a simple configuration where a single excitation coil is used to probe a wire-like conductor (grey) having an equivalent resistance equal to R. Bottom: the excitation coil and the conductor form two coupled inductors (L_1, L_2 and M are the self and mutual inductance coefficient, R_0 is the equivalent resistance of the excitation coil).

follows that

$$\mathbf{I}^T\mathbf{R}_1\mathbf{I} = \int_D \eta_1 \left\|\nabla \times \mathbf{T}_1\right\|^2 dV \geq \int_D \eta_2 \left\|\nabla \times \mathbf{T}_1\right\|^2 dV \geq \int_D \eta_2 \left\|\nabla \times \mathbf{T}_2\right\|^2 dV = \mathbf{I}^T\mathbf{R}_2\mathbf{I} \tag{5.5}$$

where the first and last equality follow from the definition of resistance matrix, the first inequality follows from the hypothesis and the second inequality follows from (5.3) when particularized to η_2. The thesis follows from the arbitrariness of **I.** In particular we can conclude that if the resistivity of the considered material increases pointwise, then the ohmic power dissipated in the conductor increases and consequently $\mathbf{P}_D^{(2)}$ decreases in the sense that will be clarified in the following. Let us consider, for the sake of simplicity, a simple system made by one exciting coil and by a filamentary conductor (see Fig. 5.2). The system is coupled magnetically (we are in the magneto- quasistatic limit) and it is equivalent to two coupled conductors (a transformer) with a current generator injecting a current on the "primary" and a resistor of the "secondary" see Fig. 5.2.

The ohmic power provided by the current generator is:

$$P = \left[R_0 + \frac{R(M/L_2)^2}{1+(R/\omega L_2)^2}\right]_i^2 \cong \left[R_0 + \frac{M^2\omega^2}{R}\right] \; i^2 \; for \; \omega \to 0 \tag{5.6}$$

where R_0 is the resistance of the exciting coil and L and M are the self and mutual inductance of the coupled inductors. From (5.6) it follows that for small ω the power P and the equivalent resistance seen from the current generator that correspond in our case to the second order term $\mathbf{P}_D^{(2)}$ of the measured impedance matrix, decrease as R (the equivalent resistance matrix of the conductive specimen) is increased, i.e., as the resistivity in D. From these considerations it follows that for two-phase materials the monotonicity can be stated as [63]:

$$V_1 \subseteq V_2 \;\text{ in } D \Rightarrow \mathbf{P}_{V_1}^{(2)} \geq \mathbf{P}_{V_2}^{(2)} \tag{5.7}$$

where $V_k \subseteq D$ represents the domain occupied by the k-th anomaly (resistivity η_a) that is hosted in the background material having resistivity $\eta_b < \eta_a$. In (5.7) $\mathbf{P}_{V_1}^{(2)} \geq \mathbf{P}_{V_2}^{(2)}$ means that matrix $\mathbf{P}_{V_1}^{(2)} - \mathbf{P}_{V_2}^{(2)}$ is positive semi-definite, i.e. all its eigenvalues are non-negative.

5.3 Monotonicity imaging method

Equation (5.7) forms the basis for the method to solve the inverse problem (see [63]). Let V be the (unknown) subset of $D$where the resistivity is η_a (the resistivity in $D \backslash V$ is η_b). The inverse problem consists in retrieving V.

Let us consider a generic (and known) test domain Ω_k. From (5.7) it follows that:

$$\mathbf{P}_{\Omega_k}^{(2)} \geq \mathbf{P}_D^{(2)} \text{false} \;\Rightarrow\quad \Omega_k \not\subset D, \tag{5.8}$$

and, thus, by checking (5.8) for different test anomalies $\Omega_k$it is possible to estimate/retrieve V. It is worth noting that the algorithm can be applied to an arbitrary number of anomalies with unknown shape and topology.

In order to test (5.8) we need to compute the eigenvalues of $\mathbf{P}_{\Omega_k}^{(2)} - \mathbf{P}_D^{(2)}$for checking if this symmetric matrix is positive semi-definite or not. However, only a noisy version $\tilde{\mathbf{P}}_D^{(2)} = \mathbf{P}_D^{(2)} + \mathbf{E}$, $\mathbf{P}_D^{(2)}$ being the noiseless matrix and $\mathbf{E}$ the noise matrix, can be measured and it can be processed as described in [63]. Similarly, the test matrices

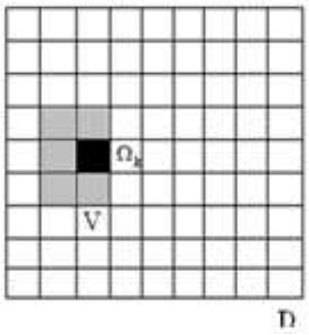

Figure 5.3: The conductive domain D subdivided in elementary regions together with an anomaly V (grey pixels) and a test region Ω_k (black pixel).

$\mathbf{P}^{(2)}_{\Omega_k}$ may be affected by either measurement errors (if measured) or numerical errors (if numerically computed). Therefore, the eigenvalues of $\tilde{\mathbf{P}}^{(2)}_{\Omega_k} - \tilde{\mathbf{P}}^{(2)}_{D}$ can be different from the eigenvalues of $\mathbf{P}^{(2)}_{\Omega_k} - \mathbf{P}^{(2)}_{D}$ and this may alter in an unpredictable way the sign of the eigenvalues with smaller magnitude, i.e. this may alter the reconstruction.

In order to deal with this situation, we quantify how much the matrix $\tilde{\mathbf{P}}^{(2)}_{\Omega_k} - \tilde{\mathbf{P}}^{(2)}_{D}$ is positive semi-definite through the so-called sign index s_k defined as:

$$s_k \hat{=} \frac{\sum_{j=1}^{M} \lambda_{k,j}}{\sum_{j=1}^{M} |\lambda_{k,j}|} \tag{5.9}$$

where $\lambda_{k,j}$ is the j-th eigenvalues of the matrix $\tilde{\mathbf{P}}^{(2)}_{\Omega_k} - \tilde{\mathbf{P}}^{(2)}_{D}$and M is the number of the available eigenvalues. We notice that s_k is closer to 1 when almost all relevant eigenvalues are non-negative (s_k=1 when $\tilde{\mathbf{P}}^{(2)}_{\Omega_k} - \tilde{\mathbf{P}}^{(2)}_{D}$ is rigorously positive semi-definite).

In addition, from perturbation theory [92], it follows that the eigenvalues that may change their sign due to the presence of noise, are only those having a magnitude smaller than the Euclidean norm of the noise. When the magnitude of the noise is known or estimated, these eigenvalues can be removed from the summations in (5.9).

Finally, we highlight that the dimension (number of rows and columns) of the matrix $\tilde{\mathbf{P}}^{(2)}_{\Omega_k} - \tilde{\mathbf{P}}^{(2)}_{D}$ is small because it is equal to the number of coils of the array that, usually, is made by few elements (few tens). Therefore, a very low computational cost (computation of the eigenvalues of $\mathbf{P}^{(2)}_{\Omega_k} - \mathbf{P}^{(2)}_{D}$) is required to compute (5.9) for performing test (5.8).

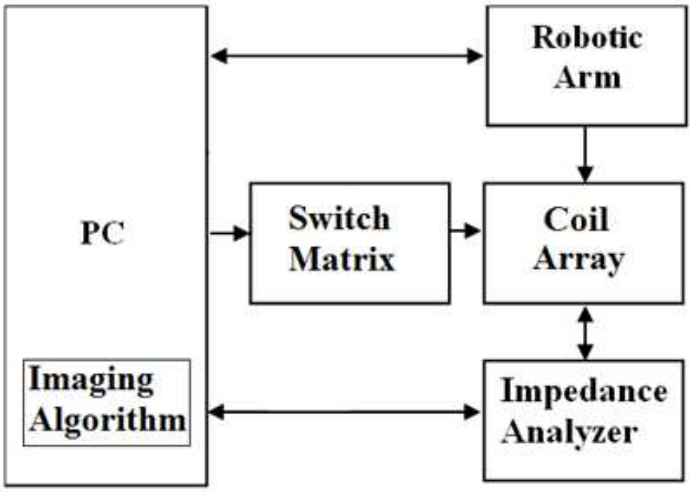

Figure 5.4: Block diagram of the measurement system.

.

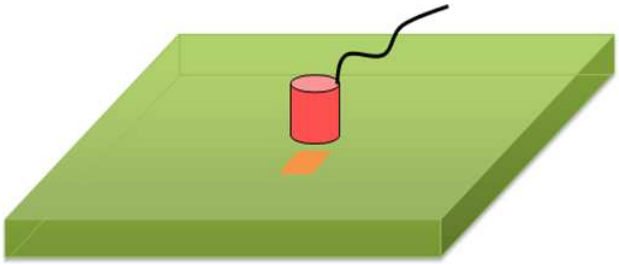

Figure 5.5: Representation of the test domain on the top side of the PCB.

.

5.4 Inversion Examples

The experimental tests we describe in the following consist of an array made by two coils mounted in a fully automated imaging system composed by a scanning system, a LCR meter and a PC controlling the whole acquisition and inversion process (see Fig.5.4).

The specimen under test is a printed circuit boards (PCB) presenting copper islands, having different size and shapes, to be imaged. The copper islands are union of 5mm×5mm elementary domains (see 5.5). These elementary domains are taken as the Ω_k during the imaging process. The sensor, that has been designed through extensive numerical simulations, is made by two pancake coils. The first coil (internal diameter=5mm, external diameter=10.5mm, height=6.5mm, number of turns=700)

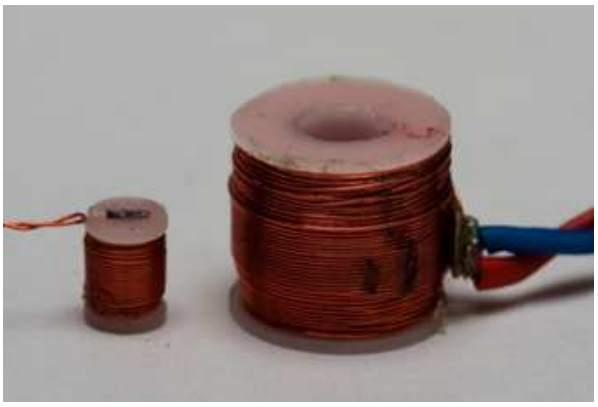

Figure 5.6: The two coils composing the array. The smaller coil is inserted into the bigger one.

.

contains internally the second coil (internal diameter=1mm, external diameter=4mm, height=3mm, number of turns=180). Simulated inversions have provided that this array gives no reconstruction errors for a noise level not greater than 50mΩ This threshold has been achieved during the experimental test that, therefore, provide error-free reconstructions. The excitation frequency is 30kHz, chosen to satisfy the condition of 4^{th} and higher order terms in (5.1) negligible. At same time, this frequency guarantees an appropriate magnitude of the measured signal and a noise level smaller than the 50mΩ threshold. The Monotonicity algorithm processes the experimental data providing the reconstruction, in 0.1ms per pixel.

5.4.1 Single-face PCB

The first test is a printed circuit board where the copper (thickness 35μm) forms the letters IP (Inverse Problem) as showed in Fig.5.7 (left). The inversion, that is showed in Fig.5.7 (right) is error free. This is because the experimental noise level is smaller than the threshold (50 mΩ) found by the aforementioned numerical simulations involving the inversion of synthetic data. It is worth noting that the second order moment for a test domain ($\mathbf{P}^{(2)}_{\Omega_k}$) has been experimentally measured on a 5mm×5mm copper island. Moreover, thanks to the translational invariance of the problem, it has been sufficient to perform the measurement of $\mathbf{P}^{(2)}_{\Omega_k}$ only a single test domain. In the following Fig.5.8(left) it is shown another benchmark. The reconstruction in Fig.5.8(right) is error free.

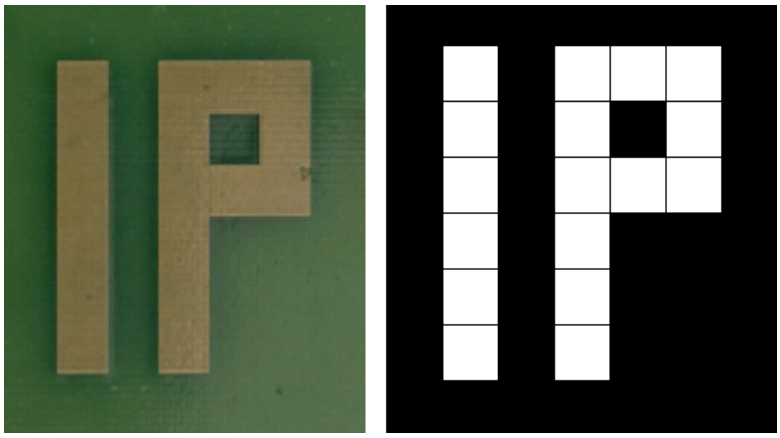

Figure 5.7: The specimen under test (left) and its reconstruction (right). The white pixels represent the conductive pixels. The pixel dimensions are 5mm×5mm.

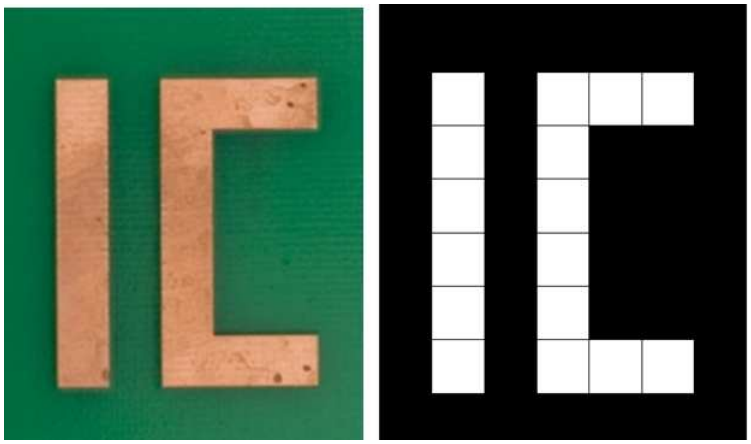

Figure 5.8: The specimen under test (left) and its reconstruction (right). The white pixels represent the conductive pixels. The pixel dimensions are 5mm×5mm.

Figure 5.9: Representation of the test domain on the top side of the PCB interested by the scanning (left), test domain on the bottom side of the PCB (right) under the dielectric.

5.4.2 Double-face PCB

The second test is a double-face printed circuit board. It consists of a double sided PCB (copper, thickness 35μm) as showed in Fig.5.10 (top). The measurements are taken from only the top side of the PCB. In this case the imaging algorithm requires the test domains on both sides on the PCB (see Fig.5.9). The test domains on a side of the PCB provide the reconstruction for the related side.

For instance, the test domains on the top side provide an error free reconstruction of the top side (Fig.5.10, left column). On the other hand, the test domain in the bottom layer provide as reconstruction the union of the pixels in the top and bottom sides (Fig.5.10, right column). This unexpected result can be easily explained by considering that it results $\tilde{\mathbf{P}}^{(2)}_{\Omega_k,\,bottom} \leq \tilde{\mathbf{P}}^{(2)}_{\Omega_k,\,top}$ and, therefore, it is trivial to prove that the test domains related to the bottom side provide a reconstruction that is the union of the pixels from the top and the bottom sides.

In the following Fig.5.11 (top) it is shown another example of double face PCB benchmark. The error free reconstructions are shown in Fig.5.11 (bottom).

It is worth noting that the image of the bottom of the PCB is obtained as difference between the showed maps except the pixel which are in common between the top and the bottom layer that is the case of Fig.5.11. This information can be retrieved by using in the inversions test domain which present metal on both the sides of the dielectric (see Fig.5.12).

These test domain have a signal which is comparable to those pixels of the benchmark which are on both the sides of the dielectric substrate. The inversion with these new test domain is shown in next Fig.5.13. In conclusion we get all the informations about the conductivity profile on the double-face PCB.

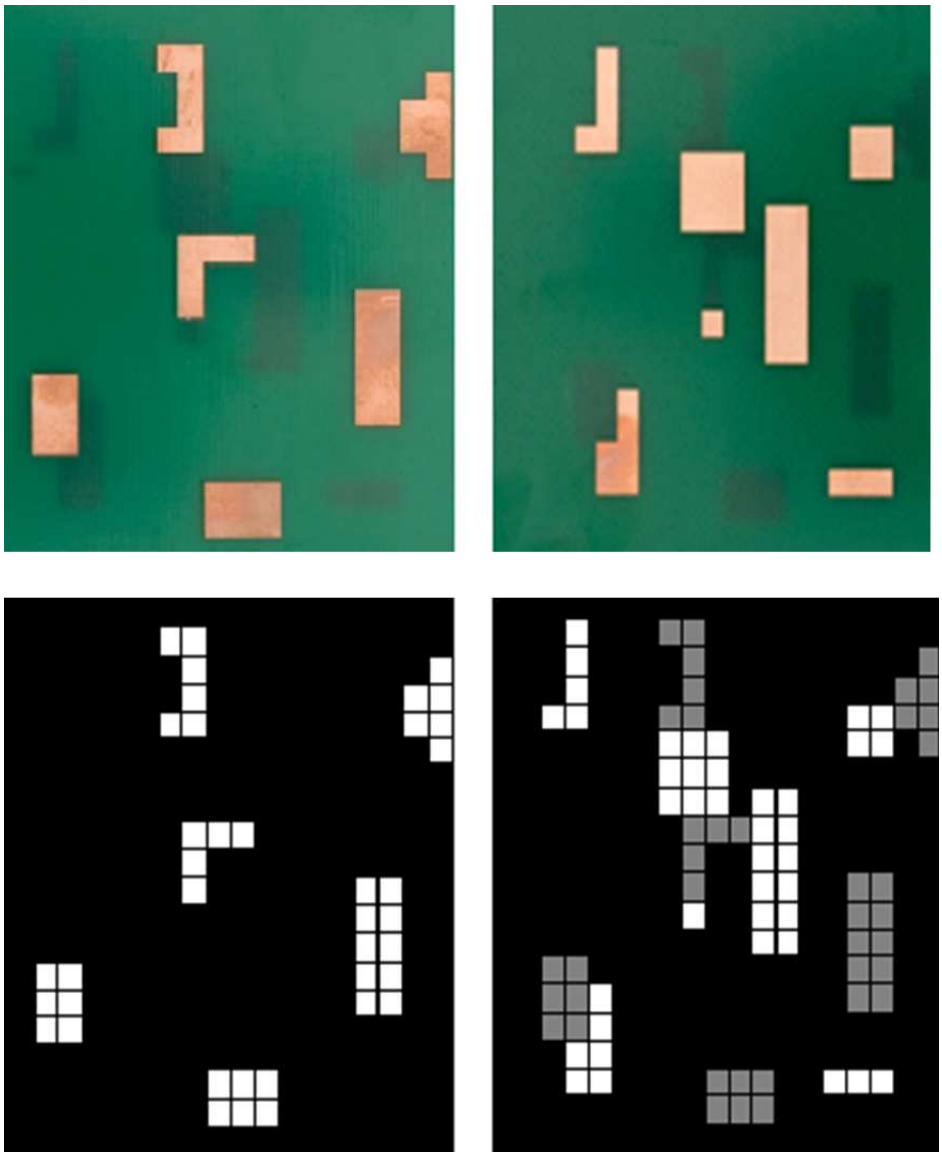

Figure 5.10: Top: The specimen under test. The top side (left) directly under the probe, and the bottom layer (right). Bottom: reconstructed image with the test domains from the top side (left) and reconstructed image with the test regions from the bottom side (right). For this latter inset the white pixels represent the pixels of the bottom side whereas the grey pixels represent the pixels of the top side.

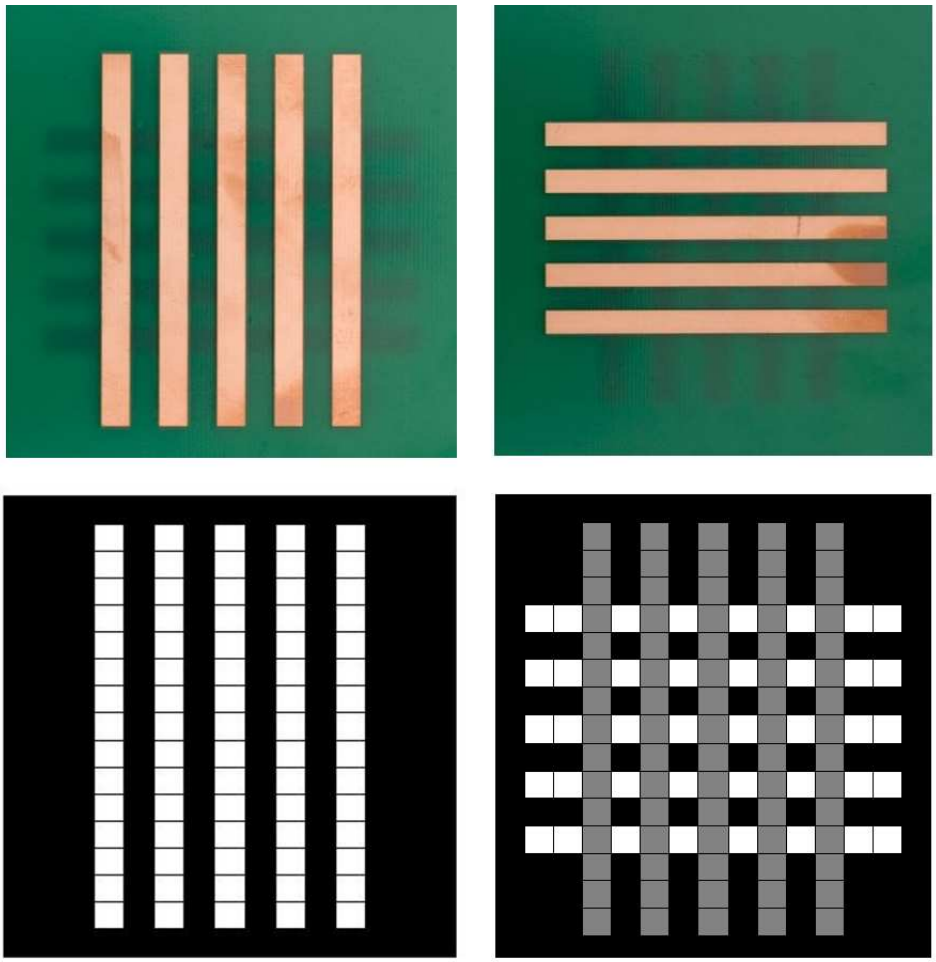

Figure 5.11: Top: The specimen under test. The top side (left) directly under the probe, and the bottom layer (right). Bottom: reconstructed image with the test domains from the top side (left) and reconstructed image with the test regions from the bottom side (right). For this latter inset the white pixels represent the pixels of the bottom side whereas the grey pixels represent the pixels of the top side.

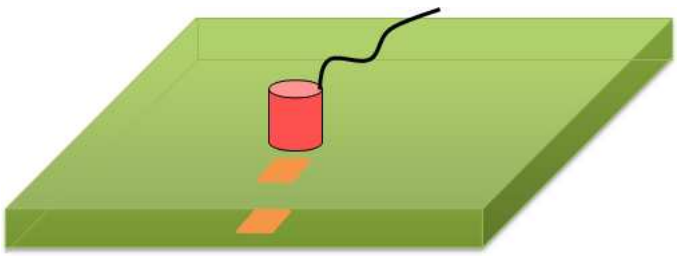

Figure 5.12: Representation of a test domain which presents metal on the top and on the bottom side of the PCB.

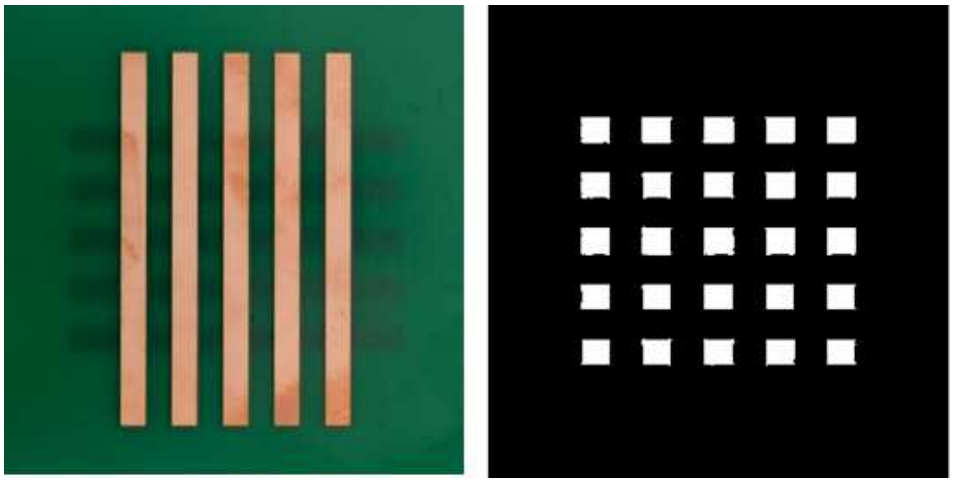

Figure 5.13: Reconstruction obtained with test domains which are on both sides of the dielectric.

5.5 Conclusions

A fast inversion method for inverting eddy-current testing data has been experimentally validated for the first time [14]. Numerical simulation of the whole imaging process (not reported here for the sake of brevity) provide noise level threshold of about 50mΩ such that for noise level below such threshold the reconstruction is error-free. The time required to form the image in a single pixel is about 0.1ms. The imaging algorithm is fully non-linear and, therefore, can treat arbitrary shapes and topologies. Moreover, the measured data have been processed by means of pre-measured data and without resorting to the numerical solution of the direct problem that, as well known, is time-consuming.

Appendix A

An Integral formulation for ECT defect simulation in linear magnetic materials

A.1 The Cariddi_ECT numerical model

Here we describe the formulation of the numerical code Cariddi_ECT which has been brefly discussed in **Chapter 2**. The model takes into account the presence of linear magnetic materials which is the case of **Chapter 3** where we model a dual element reflection probe with a ferrite magnetic circuit. The mathematical model, in the frequency domain, consists of the set of the eddy current equations in linear magnetic media:

$$\nabla \times \mathbf{E} = -j\omega \mathbf{B} \; in \; V_c \tag{A.1}$$

$$\nabla \times \mathbf{H} = \mathbf{J} \; in \; V_c \tag{A.2}$$

$$\mathbf{J} = \sigma \mathbf{E} \; in \; V_c \tag{A.3}$$

$$\mathbf{B} = \mu_0 \mathbf{H} \; in \; V_c \tag{A.4}$$

$$\mathbf{B} = \mu_0 (\mathbf{H} + \mathbf{M}) \; in \; V_f \tag{A.5}$$

$$\mathbf{M} = k\mathbf{B} \; in \; V_f \tag{A.6}$$

$$k = \frac{\mu_r - 1}{\mu_0 \mu_r} \; in \; V_f \tag{A.7}$$

where $\mathbf{E}$ is the electric field, $\mathbf{H}$ is the magnetic field, $\mathbf{B}$ is the magnetic flux density,

$\mathbf{J}$ is the current density, $\mathbf{M}$ is the magnetization vector, $\mathbf{J}_s$ is the impressed current density, σ is the electrical conductivity, and μ_r is the piecewise constant relative magnetic permeability. V_c is the conducting domain, i.e. the region of space where $\sigma \neq 0$, which will be supposed simply connected in the following to fix the ideas. The region of space where $\mu_r \neq 1$ is denoted by V_f and it can be either part of V_c either outside V_c. Outside V_c and V_f, the following equations hold:

$$\nabla \cdot \mathbf{B} = 0 \; in \; \mathbb{R}^3 \backslash \{V_c \cup V_f\} \tag{A.8}$$

$$\nabla \times \mathbf{H} = \mathbf{J}_s \; in \; \mathbb{R}^3 \backslash \{V_c \cup V_f\} \tag{A.9}$$

$$\mathbf{B} = \mu_0 \mathbf{H} \; in \; \mathbb{R}^3 \backslash \{V_c \cup V_f\} \tag{A.10}$$

where $\mathbf{J}_s$ is the impressed current density. Moreover, a suitable set of boundary and interface conditions must be imposed. The formulation recalled here is presented in detail in [4, 29, 93, 94, 95]. In this approach, the Faraday's law is automatically satisfied by expressing the electric field as:

$$\mathbf{E} = -j\omega \mathbf{A} - \nabla \varphi, \tag{A.11}$$

where φ is the electric scalar potential and $\mathbf{A}$ is the magnetic vector potential defined by Coulomb gauge:

$$\mathbf{B} = \nabla \times \mathbf{A}, \nabla \cdot \mathbf{A} = 0, \tag{A.12}$$

which can be linked to the unknown current density and magnetization by:

$$\mathbf{A}(\mathbf{x}, t) = \frac{\mu_0}{4\pi} \int_{V_c} \frac{\mathbf{J}(\mathbf{x}', t)}{|\mathbf{x} - \mathbf{x}'|} dV' + \frac{\mu_0}{4\pi} \int_{v_f} \frac{\mathbf{M}(\mathbf{x}', t) \times (\mathbf{x} - \mathbf{x}')}{|\mathbf{x} - \mathbf{x}'|^3} dV' + \mathbf{A}_s(\mathbf{x}, t) \tag{A.13}$$

where $\mathbf{A}_s$ is the vector potential due to the known source $\mathbf{J}_s$. The magnetic flux

density can also be expressed in terms of the sources **H** and **M** as:

$$\mathbf{B}(\mathbf{x},t) = \frac{\mu_0}{4\pi}\int_{V_c}\frac{\mathbf{J}(\mathbf{x}',t)\times(\mathbf{x}-\mathbf{x}')}{|\mathbf{x}-\mathbf{x}'|^3}dV' + \mu_0\mathbf{M}(\mathbf{x},t) - \frac{\mu_0}{4\pi}\int_{v_f}\nabla\cdot\mathbf{M}(\mathbf{x}',t)\frac{(\mathbf{x}-\mathbf{x}')}{|\mathbf{x}-\mathbf{x}'|^3}dV' + \frac{\mu_0}{4\pi}\int_{\partial v_f}\mathbf{M}(\mathbf{x}',t)\cdot\hat{\mathbf{n}}\frac{(\mathbf{x}-\mathbf{x}')}{|\mathbf{x}-\mathbf{x}'|^3}dS' + \mathbf{B}_s(\mathbf{x},t) \tag{A.14}$$

where $\mathbf{B}_s$ is the magnetic flux density due to the known source $\mathbf{J}_s$ and particular care must be taken to calculate the contribution of $\nabla\cdot\mathbf{M}$ if $\mathbf{M} \notin \mathbf{L}^2_{div}(V_f)$, where $\mathrm{L}^2_{div}(V_f)$ is the space of vector fields that are square integrable in V_f together with their divergence. Imposing the electric and the magnetic constitutive equations using the weighted residual approach, we obtain the following integral formulation of the field problem in terms of the sources **J** and **M**:

$$\int_{V_c}(\eta\mathbf{J}-\mathbf{E})\cdot\mathbf{W}dV = 0, \qquad \mathbf{J}\in S, \qquad \forall\mathbf{W}\in S \tag{A.15}$$

$$\int_{V_f}(\mathbf{M}-k\mathbf{B})\cdot\mathbf{W}_M dV = 0, \qquad \mathbf{M}\in\mathbf{L}^2(V_f), \quad \forall\mathbf{W}_M\in\mathbf{L}^2(V_f) \tag{A.16}$$

where $\eta{=}1/\sigma$ is the electric resistivity, $S = \{\mathrm{J}{\in}\mathrm{L}^2_{div}(V_c),\ \nabla{\cdot}\mathrm{J} = 0 \text{ in } V_c,\ \mathrm{J}{\cdot}\mathrm{n} = 0 \text{ on } \partial V_c\}$, Note that the condition J$\in S$, which implies the continuity of the normal component of J, comes from (A.15) and the continuity of the tangential components of H. On the contrary, the condition that also the weighting function W$\in$S is a numerical choice, which allows to remove the contribution of the electric scalar potential in (A.15). The numerical solution of (A.15)-(A.16) is obtained for a given discretization of V_c and V_f in terms of a finite element mesh. The condition J$\in S$ is imposed expanding $\mathbf{J} = \sum_k I_k\mathbf{J}_k$ on a set of basis functions J$_k$'s which in turn belong to S. This is guaranteed by introducing the electric vector potential T, such that $\nabla{\times}\mathrm{T} = \mathrm{J}$, and expanding it on an edge element basis N$_j$, as $\mathbf{T} = \sum_k I_k\mathbf{N}_k$ [29]. Doing so, the coefficient I_j is the line integral of T along the edge j. The uniqueness of T is guaranteed by zeroing the degrees of freedom associated to the edges of the tree of the graph made by the nodes and edges of the finite element mesh. Only the coefficients related to the edges of the co-tree are retained. Any of these coefficients, say I_k, is then the current flux linked by the loop closed by the edge k of the co-tree with the branches of the tree. It is also

straightforward to enforce the additional condition required to the functions of S:

$$\mathbf{J} \cdot \mathbf{n} = 0 \; on \; \partial V_c \tag{A.17}$$

If the tree is formed firstly connecting boundary nodes with boundary edges, for a simply connected region, all the co-tree edges on the boundary close loops completely laying on ∂V_c, and therefore the corresponding coefficient must vanish. Multiply connected regions can also be automatically treated as discussed in [96, 97]. In this way, the basis functions $\mathbf{J}_k = \nabla \times \mathbf{N}_k$ of the current density automatically belong to S, and so does J. The degrees of freedom I_k of the expansion

$$\mathbf{J} = \sum_k I_k \nabla \times \mathbf{N}_k \tag{A.18}$$

have the following property. Given a mesh facet f, let $k_1, ..k_r$ be the indices of the active (i.e. non vanishing) edges which are part of the contour ∂f of f. Then, the current flux through f is simply

$$G_f = \pm I_{k1} \pm ... \pm I_{kr} \tag{A.19}$$

where the signs depend on the relative orientation of the edges and ∂f.

The magnetization is supposed to be piecewise constant and is therefore represented using scalar pulse functions $p_k(\mathbf{x})$ as:

$$\mathbf{M}(\mathbf{x}) = \sum_{k=1}^{3N_e} M_k \mathbf{P}_k(\mathbf{x}) \tag{A.20}$$

where $\mathbf{P}_k(\mathbf{x})$ is a vector pulse function defined as

$$\mathbf{P}_k(\mathbf{x}) = p_j(\mathbf{x}) \hat{\mathbf{i}}_\alpha, \; \alpha = x, y, z \tag{A.21}$$

whereas the scalar pulse functions $p_j(\mathbf{x})$ is defined as:

$$p_j(\mathbf{x}) = \begin{cases} 1, & x \in jth \; element \, of \, V_f \\ 0, & x \notin jth \; element \, of \, V_f \end{cases} \tag{A.22}$$

Adopting the Galerkin method, i.e. choosing the W's equal to the basis functions J_k's, and the W_M's equal to the basis functions P_k's , Eqs (A.15,A.16) can be written

as:

$$\left(\underline{\underline{R}} + j\omega\underline{\underline{L}}\right)\underline{I} + j\omega\underline{\underline{FM}} = j\omega\underline{\underline{Q}}\underline{i} \tag{A.23}$$

$$\left(\underline{\underline{D}} - k\underline{\underline{E}}\right)\underline{M} - k\underline{\underline{F}}^T\underline{I} = k\underline{\underline{N}}\underline{i} \tag{A.24}$$

where $\underline{\mathrm{I}} = \{I_k\}$, $\underline{\mathrm{M}} = \{\mathrm{M}_k\}$, with $\mathrm{M}_k = \{\mathrm{M}_{k,x}, \mathrm{M}_{k,y}, \mathrm{M}_{k,z}\}$, i=$\{i_k\}$is the vector of the external coil currents and

$$L_{ij} = \frac{\mu_0}{4\pi}\int_{V_c}\int_{V_c}\frac{\nabla\times\mathbf{N}_i(\mathbf{x})\cdot\nabla\times\mathbf{N}_j(\mathbf{x}')}{|\mathbf{x}-\mathbf{x}'|}dVdV' \tag{A.25}$$

$$R_{ij} = \int_{V_c}\nabla\times\mathbf{N}_i(\mathbf{x})\cdot\eta\nabla\times\mathbf{N}_j(\mathbf{x})dV \tag{A.26}$$

$$Q_{ik} = \frac{1}{i_k}\int_{V_c}\nabla\times\mathbf{N}_i\cdot\mathbf{A}_{0_k}\,dV \tag{A.27}$$

$$F_{ij} = \frac{\mu_0}{4\pi}\int_{V_f}\int_{V_f}\frac{\nabla\times\mathbf{T}_j(\mathbf{x})\cdot(\mathbf{P}_i\times(\mathbf{x}-\mathbf{x}'))}{|\mathbf{x}-\mathbf{x}'|^3}dV\;dV' \tag{A.28}$$

$$E_{ij} = \mu_0\int_{V_f}\mathbf{P}_i\cdot\mathbf{P}_j dV - \frac{\mu_0}{4\pi}\int_{\partial V_{f,i}}\int_{\partial V_{f,j}}\frac{(\mathbf{P}_i(\mathbf{x})\cdot\mathbf{n})\;(\mathbf{P}_j(\mathbf{x}')\cdot\mathbf{n}')}{|\mathbf{x}-\mathbf{x}'|}dS\;dS' \tag{A.29}$$

$$D_{ij} = \int_{V_f}\mathbf{P}_i\cdot\mathbf{P}_j dV \tag{A.30}$$

$$N_{ik} = \frac{1}{i_k}\int_{V_f}\mathbf{P}_i\cdot\mathbf{B}_k^0 dV \tag{A.31}$$

in which $\partial V_{f,i}$ is the surface bounding the element where the shape function P_i is located and $\mathbf{B}_k^0$ is the magnetic induction produced in the vacuum by the k-th coil.

Hereafter

$$\underline{\underline{Z}}^*\underline{I} = j\omega\underline{\underline{Q}}^*\underline{i} \tag{A.32}$$

where

$$\underline{\underline{Z}}^* = \underline{\underline{R}} + j\omega\underline{\underline{L}}^* \tag{A.33}$$

$$\underline{\underline{L}}^* = \underline{\underline{L}} + \underline{\underline{FSF}}^T \tag{A.34}$$

$$\underline{\underline{Q}}^* = \underline{\underline{Q}} + \underline{\underline{FSN}} \tag{A.35}$$

$$\underline{\underline{S}} = k\left(\underline{\underline{D}} - k\underline{\underline{E}}\right)^{-1} \tag{A.36}$$

As a first step, we calculate the solution of the electromagnetic problem without the flaw. Analytical solutions are available for particular forms of the conducting structures, e.g., for an indefinite plate [35]. These analytical solutions provide acceptable approximations in most practical cases.

Otherwise, if the edge effects are not negligible, or the shape of the specimen is not canonical, the unperturbed field quantities can be determined numerically by solving (A.32) in absence of cracks, i.e. by expanding the current density J_0 in terms of shape functions J_k's, defined in V_c, in absence of defects ($\mathbf{J}_0 = \sum_k I_{0k}\mathbf{J}_k$). In this way, equation (A.32) becomes:

$$\underline{\underline{Z}}_0\underline{I}_0 = j\omega\underline{\underline{Q}}_0^*\underline{i} \tag{A.37}$$

where $\underline{\underline{Z}}_0 = \underline{\underline{R}}_0 + j\omega\underline{\underline{L}}_0^*$is the impedance matrix for the specimen without defects. The subscript "0" indicates that the matrices and the solution coefficients are calculated in the absence of the crack.

The second step for the solution of the forward problem is the determination of the modified eddy current pattern due to the presence of anomalies. In principle, the desired result might be obtained by calculating the eddy current density induced by the exciting coil in the presence of the crack, obtaining the corresponding signal, and subtracting the signal obtained without the flaw. However, to avoid cancellation errors, we exploit superposition, assuming directly the variation $\delta\mathrm{J}$ of the eddy current density

as unknown:

$$\mathbf{J} = \mathbf{J}_0 + \delta\mathbf{J} \tag{A.38}$$

The correction $\delta\mathbf{J}$ can be determined on the basis of the constraint imposed by the presence of defects. Among possible anomalies we distinguish between thin cracks and volume cracks. If the thickness of the defect is small when compared not only to its depth and width but also to the skin depth at the exciting frequency, the defect can be described as a surface Σ_d, discretized via a set of finite element faces characterized by the constraint:

$$\mathbf{J} \cdot \mathbf{n} = 0 \; on \; \Sigma_d \tag{A.39}$$

where n is the normal unit vector on the face. A volume crack is a more complex structure defined by a region Ω_d characterized by the constraint

$$\mathbf{J} = 0 \; in \; \Omega_d \tag{A.40}$$

Actually, if the shape of the crack would be known in advance, an ideal volume crack could also be associated to the constraint

$$\mathbf{J} \cdot n = 0 \; on \; \partial\Omega_d, \tag{A.41}$$

where the computational domain should be restricted to the region $V_c \backslash \Omega_d$. However this last constraint is not convenient in view of an efficient modelling of the perturbed problem using superposition. In this case, in fact, the computational domain includes also the region Ω_d. Since the identification of defects (the inverse problem) requires to solve the direct problem many times for the same specimen with different possible defects, a brute force approach, i.e. the solution of problem (A.32), with the boundary condition (A.17) imposed on $\partial V_c \cap \Sigma_d \cap \partial\Omega_d$ is not efficient at all, because the change of Σ_d for surface cracks and/or Ω_d for volume cracks implies redefinition of the tree and reassembling of the matrices.

We expand δJ in terms of the solenoidal shape functions used for the flawless plate:

$$\delta\mathbf{J} = \sum_k \delta I_k \mathbf{J}_k \tag{A.42}$$

A. AN INTEGRAL FORMULATION FOR ECT DEFECT SIMULATION IN LINEAR MAGNETIC MATERIALS

For a thin crack, the flux $\delta G_i = \int_{f_i} \delta\mathbf{J} \cdot \hat{\mathbf{n}}_i \, dS$of a given current density distribution δJ across any elementary facet f_i can be expressed as the circulation of δT (δJ=$\nabla\times\delta$T) along the edges identifying the face. As the values of the unknowns δI_k's represent the line integrals of δT along the active edges, the net current crossing an elementary face is given by the algebraic sum of the unknowns associated with the active edges of the face. Therefore, to satisfy Eq.(A.39), the normal component of δJ must be just the opposite of the unperturbed one across the crack, leading to the constraint

$$\underline{\underline{P}}_f \underline{\delta I} = -\underline{G}_0 \tag{A.43}$$

where $\underline{\underline{P}}_f$ is a (m, n) sub-matrix of the edge-facet incidence matrix with coefficients 0, +1 or -1 such as

$$P_{f,ij} = \int_{f_i} \hat{\mathbf{n}}_i \cdot \mathbf{J}_j^d S \tag{A.44}$$

Note that $\underline{G}_0 = \underline{\underline{P}}_f \underline{I}_0$ if J_0 is expanded by using the same shape functions $\mathbf{J}_k$'s defined on the discretization where the constraint is imposed.

In a similar way, we can describe the current density J_0inside Ω_d using the expansion (A.18), by requiring that $\int_{\Omega_d} \|\mathbf{J}(\mathbf{r}) + \mathbf{J}_0(\mathbf{r})\|^2 \, d\mathbf{r}$ is minimum. This condition yields the linear system

$$\underline{\underline{P}}_d \underline{\delta I} = -\underline{w}_0 \tag{A.45}$$

where

$$P_{d,ij} = \int_{\Omega_d} \mathbf{J}_i \cdot \mathbf{J}_j^d \mathbf{r} \tag{A.46}$$

$$w_{0,i} = \int_{\Omega_d} \mathbf{J}_i \cdot \mathbf{J}_0 d\mathbf{r} \tag{A.47}$$

It is worth noting that (x) is equivalent to imposing J(r)=-J_0(r) in Ω_d in weak sense. We also notice, as before, that $\underline{w}_0 = \underline{\underline{P}}_d \underline{I}_0$ if J_0 is expanded by using the same shape functions $\mathbf{J}_k$'s represent $\mathbf{J}$ in (A.32).

In conclusion, the problem is described by the following system of algebraic equations

$$\underline{\underline{Z}}\underline{\delta I} = 0 \tag{A.48}$$

with the constraint $\underline{\underline{P}}_f\underline{\delta I} = -\underline{G}_0$for a thin crack, and the constraint $\underline{\underline{P}}_d\underline{\delta I} = -\underline{w}_0$ for a volume crack.

The impedance change of a given couple of exciting coils, associated to the presence of the flaw, is given by:

$$\delta Z_{kl} = \frac{j\omega}{2i_k i_l}[(\underline{\underline{Q}}_k^*)^T \delta I_l i_k + (\underline{\underline{Q}}_l^*)^T \delta I_k i_l] \tag{A.49}$$

We now summarize the numerical method proposed in [4, 95] to solve the problem. This method is very efficient when the solution for many different trial defects is required. Indeed, by a block partition of the impedance matrix, the unknowns outside the crack region can be eliminated, with the subsequent reduction of the order of the system that should be solved at any step of the inversion procedure.

We initially refer to a volumetric flaw. We note that in practice it is often possible to identify a search region V_T containing the defect in its interior. The identification of this tentative region is fairly easy from the experimental viewpoint. Therefore, we assume that V_T is a possibly small subset of V_C and that Ω_d is an arbitrary subset of V_T, i.e. $\Omega_d \subseteq V_T$.

Let $\underline{\underline{P}}_T$ and $\underline{\mathrm{w}}_T$ be the matrix and vector defined by (A.46) and (A.47), respectively, but referred to V_T. Let us define the following change of variables:

$$\underline{\delta I} = \underline{\underline{K}}_T\underline{x} + \underline{\underline{R}}_T^T\underline{y} \tag{A.50}$$

where the columns of the matrix $\underline{\underline{K}}_T$ span the null space of $\underline{\underline{P}}_T$ and the rows of $\underline{\underline{R}}_T$ are an orthonormal basis for the space spanned by the rows of $\underline{\underline{P}}_T$. In this way, the unknown can be partitioned into two sets: one is related to $\underline{\mathrm{x}}$ and it accounts for current densities flowing externally to V_T, as$\underline{\underline{P}}_T\underline{\underline{K}}_T\underline{x} = \underline{0}$ for any $\underline{\mathrm{x}}$. The other one, related to $\underline{\mathrm{y}}$, takes into account the current densities flowing in V_T^E, defined as the union of the elements of the finite elements mesh sharing at least one active edge with V_T.

For a given $\Omega_d \subseteq V_T$, we have also that $\underline{\underline{P}}_d \underline{\underline{K}}_T = \underline{\underline{0}}$, because the columns of $\underline{\underline{K}}_T$ represent current densities that are vanishing in V_T and, therefore, also vanishing in Ω_d. Thus, substituting (A.50) in (A.45), we have

$$\underline{\underline{P}}_d \underline{\underline{R}}_T^T \underline{y} = -\underline{w}_0 \tag{A.51}$$

This constraint can be imposed by representing the solution of (A.29) as:

$$\underline{y} = \underline{\underline{\tilde{K}}}_d \underline{q} + \underline{y}_0 \tag{A.52}$$

where the columns of the matrix $\underline{\underline{\tilde{K}}}_d$span the null space of $\underline{\underline{P}}_d \underline{\underline{R}}_T^T$ and $\underline{y}_0$ is a particular solution of (A.51).

By substituting (A.51) in (A.49) we have the following change of variables

$$\delta \underline{I} = \underline{\underline{K}}_T \underline{x} + \underline{\underline{R}}_T^T \underline{\underline{\tilde{K}}}_d \underline{q} + \underline{\underline{R}}_T^T \underline{y}_0 \tag{A.53}$$

where the unknowns are $\underline{x}$ and $\underline{q}$, and an impressed source in Ω_d: is explicitly introduced. In (A.52) $\underline{x}$, as already remarked, represents current densities flowing in $V_C \backslash V_T$, $\underline{q}$ current densities flowing in $V_T^E \backslash \Omega_d$ and $\underline{y}_0$ represents the best approximation of -J_0(r) in Ω_d. Applying the Galerkin method to (A.29) with the new shape functions following from (A.53) we easily obtain:

$$\underline{\underline{Z}}_{xx} \underline{x} + \underline{\underline{Z}}_{xy} \underline{\underline{\tilde{K}}}_d \underline{q} = -\underline{\underline{Z}}_{xy} \underline{y}_0 \tag{A.54}$$

$$\underline{\underline{\tilde{K}}}_d^T \underline{\underline{Z}}_{yx} \underline{x} + \underline{\underline{\tilde{K}}}_d^T \underline{\underline{Z}}_{yy} \underline{\underline{\tilde{K}}}_d \underline{q} = -\underline{\underline{\tilde{K}}}_d^T \underline{\underline{Z}}_{yy} \underline{y}_0 \tag{A.55}$$

where

$$\underline{\underline{Z}}_{xx} \hat{=} \underline{\underline{K}}_T^T \underline{\underline{\underline{Z}}} \underline{\underline{K}}_T \tag{A.56}$$

$$\underline{\underline{Z}}_{xy} = \underline{\underline{Z}}_{yx}^T \hat{=} \underline{\underline{K}}_T^T \underline{\underline{\underline{Z}}} \underline{\underline{R}}_T^T \tag{A.57}$$

$$\underline{\underline{Z}}_{yy} \hat{=} \underline{\underline{R}}_T \underline{\underline{\underline{Z}}} \underline{\underline{R}}_T^T. \tag{A.58}$$

Solving (A.54) with respect to $\underline{x}$ and substituting in (A.55) leads to:

$$\underline{\underline{\tilde{K}}}_d^T \left(\underline{\underline{Z}}_{yy} - \underline{\underline{S}}_{yy} \right) \underline{\underline{\tilde{K}}}_d \underline{q} = \underline{\underline{\tilde{K}}}_d^T \left(\underline{\underline{S}}_{yy} - \underline{\underline{Z}}_{yy} \right) \underline{y}_0 \tag{A.59}$$

$$\underline{x} = -\underline{\underline{Z}}_{xx}^{-1} \underline{\underline{Z}}_{xy} \left(\underline{\underline{\tilde{K}}}_d \underline{q} + \underline{y}_0 \right) \tag{A.60}$$

where

$$\underline{\underline{S}}_{yy} = \underline{\underline{Z}}_{yx} \underline{\underline{Z}}_{xx}^{-1} \underline{\underline{Z}}_{xy}. \tag{A.61}$$

In case of a thin crack, the partition of the unknowns is much easier. As for the volume flaw, we identify a set Σ_T of all possible candidate crack facets, i.e. the set of all mesh facets which could possibly belong to the crack. Consequently, we assume that Σ_d is an arbitrary subset of Σ_T, i.e. $\Sigma_d \subseteq \Sigma_T$.

In this case, every elementary facet f_i of Σ_T is characterized by an elementary flux G_i and it is easily possible to directly identify the subset $\underline{\mathrm{G}}_0$ characterizing Σ_d. Therefore, we introduce the following change of variables, analogous to eq. (A.50):

$$\delta \underline{I} = \underline{\underline{K}}_T \underline{x} + \underline{\underline{W}}_b \underline{\delta G}_b + \underline{\underline{W}}_f \underline{\delta G}_f \tag{A.62}$$

where now the columns of the matrix $\underline{\underline{K}}_T$ span the null space of $\underline{\underline{P}}_f$, defined by (A.44) but referred to Σ_T, $\left[\underline{\underline{W}}_b \, \underline{\underline{W}}_f \right] = \underline{\underline{P}}_f$, and $\underline{\delta G}_b$ ($\underline{\delta G}_f = -\underline{G}_0$) are the current fluxes (unperturbed current fluxes) through the mesh facets belonging to $\Sigma_T \backslash \Sigma_d$ (to Σ_d). Having identified the unknowns $\underline{\delta G}_b$ in $\Sigma_T \backslash \Sigma_d$, the analogous of the Eqs (A.54)-(A.55) can be easily written as

$$\underline{\underline{Z}}_{xx} \underline{x} + \underline{\underline{Z}}_{xb} \underline{\delta G}_b = \underline{\underline{Z}}_{xf} \underline{G}_0 \tag{A.63}$$

$$\underline{\underline{Z}}_{bx} \underline{x} + \underline{\underline{Z}}_{bb} \underline{\delta G}_b = \underline{\underline{Z}}_{bf} G_0 \tag{A.64}$$

where

$$\underline{\underline{Z}}_{xx} \hat{=} \underline{\underline{K}}_T^T \underline{\underline{\underline{Z}}} \underline{\underline{K}}_T \tag{A.65}$$

$$\underline{\underline{Z}}_{xy} = \underline{\underline{Z}}_{yx}^{T} \hat{=} \underline{\underline{K}}_{T}^{T} \underline{\underline{\underline{\underline{ZW}}}}_{y} \tag{A.66}$$

$$\underline{\underline{Z}}_{by} \hat{=} \underline{\underline{W}}_{b}^{T} \underline{\underline{\underline{\underline{ZW}}}}_{y}^{\cdot} \tag{A.67}$$

The efficiency of the proposed numerical scheme comes from the fact that system (A.59) is small because of the order of the number of DoF's in region V_T that, by assumption, is a small part of the whole conducting domain V_c.

Moreover, for a given V_T, matrices $\underline{\underline{Z}}_{xx}$, $\underline{\underline{Z}}_{xy}$, $\underline{\underline{Z}}_{yy}$, $\underline{\underline{S}}_{yy}$ and $\underline{\underline{Q}}_{y}$ are independent from V_0 and can be computed once for all. On the other hand, each time that Ω_d is changed, the re-computation of the matrix $\tilde{\underline{\underline{K}}}_{d}^{T} \left(\underline{\underline{Z}}_{yy} - \underline{\underline{S}}_{yy} \right) \tilde{\underline{\underline{K}}}_{d}$ as well as the vector $\tilde{\underline{\underline{K}}}_{d}^{T} \left(\underline{\underline{S}}_{yy} - \underline{\underline{Z}}_{yy} \right) \underline{y}_0$ (see (A.59)) requires a modest computational cost because it involves multiplications of matrices of the order of the number of DoF's in region V_T. Similarly, the computation of $\underline{y}_0$ involves the solution of a small system.

Finally, we notice that the number and the shape of the defects are not limited by any further modelling assumption, the only constraint being that Ω_d should be a subset of volume elements of V_T. Similar considerations hold true for the system of equations (A.63)-(A.64).

Bibliography

[1] F. Calvano, P. Raumonen, S. Suuriniemi, L. Kettunen, G. Rubinacci, "Size Is in the Eye of the Beholder: Technique for Non-destructive Detection of Parameterized Defects", *IEEE trans on Magn.*, pp. 3006-3009, vol. 46, 2010. 11, 13, 37

[2] R. Albanese, G. Rubinacci, and F. Villone, "An integral computational model for defect simulation and detection via eddy currents", *J. Comp. Phys.*, vol. 152, pp. 736-755, 1999. 11, 14, 24, 25, 76

[3] M. Morozov, G. Rubinacci, A. Tamburrino, and S. Ventre, "Numerical Models with Experimental Validation of Volumetric Insulating Defects in Eddy Current Testing", *IEEE Trans. on Magnetics*, vol. 42, no. 5, pp. 1568-1576, 2006. 11, 14, 24, 25, 39, 47, 76

[4] S. Ventre, F. Calvano, G. Pichenot, P. Calmon and A. Tamburrino, "ECT benchmark results for 3D defect signatures in industrial applications, *NDT & E International, 2010, in print.* 11, 37, 90, 97

[5] C. Gilles-Pascaud, G. Pichenot, D. Premel, C. Reboud, A. Skarlatos, "Modeling of eddy current inspections with CIVA", *proceedings of the 17th World Conference on Nondestructive Testing, Shanghai, edited on CD-ROM*, 2008. 11

[6] F. Carmelo, F.G. Guimaraes, H. Igarashi, K. Watanabe and J. A. Ramirez, "An Immune-based Algorithm for Topology optimization", *IEEE Congress on Evolutionary Computation, Vancouver (Canada)* , pp. 10973-10980, 2006. 12, 39, 42, 44

[7] F. Calvano, G. Caturano, G. Cavaccini, G. Rubinacci, A. Tamburrino, S. Ventre, "Crack shape reconstruction from ECT using Topology Costrained Optimization

(TOPCSA) Algorithms", *Electromagnetic Nondestructive Evaluation (XIII), Ios press*, pp 230-237, 2010. 12, 39, 52

[8] A. Tamburrino and G. Rubinacci, "A new non-iterative inversion method for electrical Resistance tomography", *Inverse Problems*, pp. 1809-1829, 2002. 12, 55, 57, 69, 75

[9] M. Hanke and M. Brühl, "Numerical implementation of two noniterative methods for locating inclusions by resistance tomography", *Inverse Problems*, vol. 16, pp. 1029-1042, 2000. 12, 59, 61

[10] H. Lev-Ari, A.J. Devancy, "The time-reversal technique re-interpreted: subspace-based signal processing for multi-static target location", *proc. of the 2000 IEEE Sensor Array and Multichannel Signal Processing Workshop, Cambridge, MA (USA)*, pp. 509-513, 2000. 12, 63

[11] F. Calvano, G. Rubinacci, A. Tamburrino, "Non-Iterative Imaging Method for Electrical Resistance Tomography", *Frontiers in Artificial Intelligence and Applications, Ios press*, vol. 204, pp. 241-246, 2009. 12, 74

[12] F. Calvano, G. Rubinacci, A. Tamburrino, "Non-Iterative Imaging Methods for Electrical Resistance Tomography: comparison between two fast methods", *in Electromagnetic Nondestructive Evaluation (XIII) , Ios press*, pp 173 - 180, 2010. 12, 74

[13] F. Calvano, G. Rubinacci, A. Tamburrino, "Non-Iterative Methods for Locating Inclusions in Electrical Impedance Tomography", *proceeding of the 17th International Conference on the Computation of Electromagnetic Fields (COMPUMAG), November 22-26 2009, Florianpolis, Brazil.* 12, 74

[14] S. Ventre , F. Calvano, G. Rubinacci, A. Tamburrino, "Experimental Validation of a Fast Non-Iterative Imaging Algorithm for Eddy Current Tomography", *accepted for publication in Electromagnetic Nondestructive Evaluation (XIV), Ios press.* 12, 57, 58, 75, 87

[15] A. Bossavit , J.C. Verite: "A Mixed FEH-BlEM Method to Solve 3-D Eddy Current Problems", *IEEE trans on Magn.*, pp. 431 -435, 1982. 13

[16] C.J. Carpenter : "Comparison of Alternative Formulations of 3-D Magnetic Field and Eddy Current Problem a at Power Frequencies", *IEE Proc.*, vol. 124, n. 2, pp.l026-1034, 1977. 13

[17] N. L. Brown, "Calculation of 3-D Eddy Currents at Power Frequencies", *IEE Proc.*, vol. 129, n. 1, pp.46-53. 1982. 13

[18] R. Albanese, G. Rubinacci, "Solution of three dimensional eddy current problems by integral and differential methods", *IEEE Trans. Magn.*, vol. 24, pp. 98-101, 1988. 13

[19] O. Bíró and K. Preis, "On the use of the magnetic vector potential in the finite element analysis of three-dimensional eddy currents", *IEEE Trans. Magn.*, vol. 25, no. 4, pp. 3145-3159, 1989. 13, 21

[20] P. Raumonen, S. Suuriniemi, and L. Kettunen, "Parametric models in quasi-static electromagnetics", *IEEE Trans. Magn.*, vol. 45, no. 3, pp. 944-947, 2009. 13, 15, 17

[21] P. Raumonen, S. Suuriniemi, T. Tarhasaari, and L. Kettunen, "Manifold and metric in numerical solution of the quasi-static electromagnetic boundary value problems", *arXiv.org, Mathematical Physics*, 2007. 15, 16

[22] N. Harfield, J.R. Bowler, "Theory of thin-skin eddy-current interaction with surface cracks", *Journal of Applied Physics*, vol. 82, no. 9, pp. 4590603, 1997. 13

[23] Z. Chen, K. Miya, and M. Kurokawa, "Reconstruction of Defect shapes using a newly developed ECT probe", *in Electromagnetic Non destructive Evaluation II, IOS press*, pp. 225-232, 1998. 13

[24] J.R. Bowler, S.A. Jenkins, L.D. Sabbagh, and H. A. Sabbagh, "Eddy-current probe impedance due to a volumetric flaw", *J. Appl. Phys.*, vol. 70, no. 3, pp. 1107-1114, 1991.

[25] Y. Le Bihan,, J. Pv, C. Marchand, "Study and experimental validation of the calculation of the ECT signal induced by a minute defect using a FEM-BIM combination", *NDT & E International*, vol. 39, pp. 476-486, 2006.

[26] V. Monebhurrun, D. Lesselier, and B. Duchne, "Eddy current nondestructive evaluation of a 3-D bounded defect in a metal tube using volume integral methods and nonlinearized inversion schemes", *in Electromagnetic Non destructive Evaluation II, IOS Press*, pp. 261-270, 1998.

[27] J. Pavo and K. Miya, "Reconstruction of defect shape by optimization using eddy current field measurement", *IEEE Trans. Magn.*, vol. 30, no. 5, pp. 3407-3410, 1994.

[28] T. Theodoulidis, N. Poulakis, A. Dragogias, "Rapid computation of eddy current signals from narrow defects", *NDT & E International*, vol. 43, Issue 1, pp. 13-19, 2010. 13

[29] R. Albanese and G. Rubinacci, "Finite element methods for the solution of 3D eddy current problems", *Advances in Imaging and Electron*, 1997. 21, 90, 91

[30] R. Albanese and G. Rubinacci, "Integral formulation for 3D eddy-current computation using edge elements", *IEE Proc.*, vol. 135, no. 7, pp. 457-462, 1988. 21

[31] A. Bossavit, "Whitney forms: A class of finite elements for three- dimensional computations in electromagnetism", *IEE Proc.*, vol. 135, Pt. A, pp. 493-500, 1988. 23

[32] J.C. Vérité, "Application of a 3-d eddy current code (TRIFOU) to nondestructive testing", *COMPEL*, vol. 3, pp. 167-178, 1984. 23, 24

[33] C. Geuzaine and J.F. Remacle, "Gmsh: a three-dimensional finite element mesh generator with built-in pre- and post-processing facilities", *International Journal for Numerical Methods in Engineering*, vol. 79, pp. 1309-1331, 2009. 23

[34] P. Dular and C. Geuzaine and F. Henrotte and W. Legros, "A general environment for the treatment of discrete problems and its application to the finite element method",*IEEE Trans. Magn.*, vol. 34, no. 5, pp. 3395-3398, 1998. 23

[35] C.V. Dodd and W. E. Deeds, "Analytical solutions to eddy-current probe-coil problems", *J. Appl. Phys.*, vol. 39, no. 6, pp. 2829-2838, 1968. 26, 94

[36] M. Adamo, F. Calvano, C. Nappi, E. Sarnelli, "Scanning magnetic microscopy model analysis of circular flaws in thin metallic plates", *J. Appl. Phys.*, pp. 123913-123913-7, vol. 106, 2009. 26

[37] G. Rubinacci, R. Fresa, S. Ventre, "An eddy current integral formulation on parallel computer systems", *International Journal for Numerical Methods in Engineering*, vol. 62, n. 9, 2004. 14

[38] G. Rubinacci, S. Ventre, F. Villone, Y. Liu, "A fast technique applied to the analysis of Resistive Wall Modes with 3D conducting structures", *Journal of Computational Physics*, 2009. 14

[39] D. Colton and L. Paivarinta, "The uniqueness of a solution to an inverse scattering problem for electromagnetic waves", *Arch. Ration. Mech. Anal.*, vol. 119, pp. 59-70, 1992. 39, 75

[40] V. Isakov, "Uniqueness and stability in multidimensional inverse problems", *Inverse Problems*, pp. 579-621, 1993.

[41] M. Yamamoto, "A mathematical aspect of inverse problems for non-stationary Maxwell's equations", *Int. J. Appl. Electromagn. Mech.*, pp. 77-98, 1997. 39, 75

[42] Z. Chen, G. Preda, O. Mihalache and K. Miya, "Reconstruction of Crack shape from the MFLT signals by using a rapid forward solver and an optimization approach", *IEEE Trans. Magn.*, vol. 38, no. 2, pp. 1025-1028, 2002. 39

[43] Y. Li, L. Udpa, and S. S. Udpa, "Three-dimensional defect reconstruction from eddy current NDE signals using a genetic local search algorithm," *IEEE Trans. Magn.*, vol. 40, no. 2, pp. 410-417, 2004.

[44] D. Dos Reis, M. Lambert, and D. Lesselier, "Non-destructive evaluation of 3-D voids in a metal plate," *Inverse Problems*, vol. 18, pp. 1857-1871, 2002.

[45] D. Premel and A. Baussard, "Eddy-current evaluation of three dimensional flaws in flat conductive materials using a Bayesian approach," *Inverse Problems*, vol. 18, pp. 1873-1889, 2002.

[46] G. Rubinacci, A. Tamburrino, and S. Ventre, "A differential formulation based on a perturbative approach to solve the ECT inverse problem," *Comput. Methods Appl. Mech. Eng.*, vol. 169, pp. 407-424, 1999.

[47] Z. Badics, J. Pv, H. Komatsu, Y. Matsumoto, S. Kojima, and K. Aoki, "Fast flaw reconstruction from 3D eddy current data," *IEEE Trans. Magn.*, vol. 34, no. 5, pp. 2823-28, 1998.

[48] A. Tamburrino and G. Rubinacci, "A new non-iterative inversion method for electrical resistance tomography", *Inverse Problems*, vol. 18, pp. 1809-29, 2002.

[49] G. Rubinacci, A. Tamburrino, S. Ventre, F. Villone, "Reconstruction of Interacting Cracks in Conductive Materials by a Communications Theory Approach", *Electromagnetic Non-destructive Evaluation (IV), IOS Press*, pp. 151-158, 2000. 39

[50] J. Hansen and N. Thorpe, "Low frequency eddy current inspection", *Conference Proceedings, NDT 2003, Worcester, (UK)*, pp. 147-154, 2003. 45

[51] J. Hansen, "Back to basics: The eddy current inspection method", *Parts 1-4, Insight - Non-Destructive Testing and Condition Monitoring*, vol. 46, no. 5-8, 2004. 45

[52] M. Cheney, D. Isaacson and J.C. Newell, "Electrical Resistance Tomography", *SIAM Review 41*, pp. 85-101, 1999. 55, 56, 65

[53] A. Ramirez, W. Daily, B. Binley, D. LaBreque and D. Roelant, "Detection of leaks in underground storage tanks using electrical resistance methods", *J. Environ. Eng. Geophys.*, vol. 1, pp. 189-203, 1996. 55

[54] M.R. Eggleston, R.J. Schwabe, D. Isaacson, and J.C. Newell, "The application of electric current computed tomography to defect imaging in metals", in *Review of Progress in Quantitative NDE,* vol. 9A, 1989. 55

[55] G. Rubinacci, A. Tamburrino, S. Ventre, F. Villone, "Shape identification in conductive materials by Electrical Resistance Tomography", *in Electromagnetic Non-destructive Evaluation (VI), IOS Press*, pp. 13-20, 2002. 55

[56] R.A. Williams and M.S. Beck, "Process Tomography-Principles, Techniques, and Applications", *Butterworth-Heinemann, Oxford, UK*, 1995. 55

[57] A.P. Calderón, "On an inverse boundary value problem", *Seminar on Numerical Analysis and its Applications to Continuum Physics (Society Brasileira de Matematica)*, pp. 65-73, 1980. 55

[58] R. Kohn and M. Vogelius, "Determining conductivity by boundary measurements", *Commun. Pure Appl.Math.* , pp. 289-298, 1984. 56

[59] J. Sylvester and G. Uhlmann, "Global uniqueness theorem for an inverse boundary value problem", *Ann. Math.*, vol. 125, pp.153-69, 1987.

[60] A.I. Nachman, "Reconstruction from boundary measurements", *Ann. Math.* , vol 128, pp.531-576, 1998.

[61] A.I. Nachman, "Global uniqueness for a two-dimensional inverse boundary value problem", *Ann. Math.*, vol. 142, pp. 71-96, 1995.

[62] V. Isakov, "Uniqueness and stability in multi-dimensional inverse problems", *Inverse Problems*, vol 9, pp. 579-621, 1993. 56

[63] A. Tamburrino and G. Rubinacci, "Fast Methods for Quantitative Eddy-Current Tomography of Conductive Materials", *IEEE Trans. Magn.*, vol. 42, pp. 2017-2028, 2006. 57, 75, 77, 79

[64] G. Rubinacci, A. Tamburrino, S. Ventre, "Eddy current imaging of surface breaking defects by using monotonicity based methods", *ACES Journal*, vol.23, no. 1, pp. 46-52, 2008. 57, 75

[65] A. Tamburrino, S. Ventre, G. Rubinacci, "Recent developments of a Monotonicity Imaging Method for Magnetic Induction Tomography", *Inverse Problems*, vol. 26, no. 7, pp. 074016, 2010. 57, 75

[66] M. Hanke and M. Brühl, "Recent progress in electrical Resistance tomography", *Inverse Problems*, pp. S65-S90, 2003. 59, 61, 65

[67] D. Colton and A. Kirsch, "A simple method for solving inverse scattering problems in the resonance region" *Inverse Problems*, vol. 12, pp. 383-393, 1996. 59

[68] A. Kirsch, "Characterization of the shape of the scattering obstacle using the spectral data of the far field operator", *Inverse Problems* **14** 1489–512, 1998. 59

[69] M. Brühl, M. Hanke and M. S. Vogelius, "A direct impedance tomography algorithm for locating small inhomogeneities", *Numer. Math.*, vol. 93, pp. 635-54, 2003. 65

[70] M. Cheney, "The linear sampling method and the MUSIC algorithm", *Inverse Problems*, vol. 17, pp. 591-6, 2001.

[71] A. Friedman, and M.S. Vogelius, "Identification of small inhomogeneities of extreme conductivity by boundary measurements: a theorem on continuous dependence", *Arch. Ration. Mech. Anal.*, vol 105, pp. 299-326, 1989. 65

[72] A Kirsch, "The MUSIC algorithm and the factorization method in inverse scattering theory for inhomogeneous media", *Inverse Problems*, vol 18, pp. 1025-1040, 2002. 65

[73] P.A.T. Pinheiro, W.W. Loh and F.J. Dickin, "Three-dimensional reconstruction algorithm for electrical resistance tomography", *IEE Proc. Sci. Meas. Technol*, vol. 145, pp. 85-93, 1998. 71

[74] W.Q. Yang (Guest Editor), "Special feature: Electrical Tomography - Industrial and Medical, Measurement", *Science and Technology*, vol. 21, 2001.

[75] M. Soleimani and A. Tamburrino, "Shape reconstruction in magnetic induction tomography using multifrequency data", *Int. Jour. of Information and System Sciences.*, vol. 2, pp. 343-353, 2006.

[76] W. Yin and A.J. Peyton, "A planar EMT system for the detection of faults on thin metallic plates", *Measurement Science and Technology*, vol 17, pp. 2130- 2135, 2006.

[77] A. Pirani, M. Ricci, R. Specogna, A. Tamburrino and F. Trevisan, "Multifrequency identification of defects in conducting media", *Inverse Problems*, vol. 24, 2008.

[78] A. Tamburrino, S. Ventre and G. Rubinacci, "Electrical resistance tomography: complementarity and quadratic models", *Inverse Problem*, vol. 16, pp. 1585-1618, 2000.

[79] R. Pierri and A. Tamburrino, "On the local minima problem in conductivity imaging via a quadratic approach", *Inverse Problems*, vol. 13, pp. 1547-68, 1997.

[80] G. Rubinacci, A. Tamburrino and S. Ventre, "A differential formulation based on a perturbative approach to solve the ECT inverse problem", *Comput. Methods Appl. Mech. Eng.*, vol. 169, pp. 407-24, 1999.

[81] D. Dos Reis, M. Lambert and D. Lesselier, "Non-destructive evaluation of 3-D voids in a metal plate", *Inverse Problems*, vol. 18, pp. 1857-71, 2002.

[82] D. Premel and A. Baussard, "Eddy-current evaluation of three dimensional flaws in flat conductive materials using a Bayesian approach", *Inverse Problems*, vol. 18, pp. 1873-89, 2002.

[83] J.R. Bowler, "Thin-skin eddy current inversion for the determination of crack shapes", *Inverse Problems*, vol. 18, pp. 1891-905, 2002.

[84] B. Luong and F. Santosa, "Quantitative imaging of corrosion in plates by eddy current methods", *SIAM J. Appl. Math.*, vol. 58, pp. 1509-31, 1998.

[85] V. Monebhurrun, B. Duchne and D. Lesselier, "Three-dimensional inversion of eddy current data for nondestructive evaluation of steam generator tubes", *Inverse Problems*, vol. 14, pp. 707-24, 1998.

[86] Z. Badics, J. Pv, H. Komatsu, S. Kojima, Y. Matsumoto and K. Aoki, "Fast flaw reconstruction from 3D eddy current data", *IEEE Trans. Magn.*, vol. 34, pp. 2823-2828, 1998.

[87] L. Yue, L. Udpa and S.S. Udpa, "Three-dimensional defect reconstruction from eddy-current NDE signals using a genetic local search algorithm", *IEEE Trans. Magn.*, vol. 40, pp. 410-417, 2004.

[88] W. Yin, S. J. Dickinson and A. J. Peyton, "Imaging the continuous conductivity profile within layered metal structures using inductance spectroscopy", *IEEE Sensors J.*, vol 5, pp. 161-166, 2005.

[89] S. M. Nair and J. H. Rose, "Reconstruction of three-dimensional conductivity variations from eddy current (electromagnetic induction) data", *Inverse Problems*, vol. 6, pp. 1007-30, 1990.

[90] O. Dorn and D. Lesselier, "Level set methods for inverse scattering-some recent developments", *Inverse Problems*, vol. 25, pp. 67-131.

[91] Q.N. Jin, "On the iteratively regularized Gauss-Newton method for solving nonlinear ill-posed problems", *Math. Comput.*, vol. 69, pp. 1603-1623, 2000.

[92] G.H. Golub and C.F. Van Loan, "Matrix Computations", *Sciences 3rd Edition, Johns Hopkins University Press, Baltimore, USA*, 1996. 80

[93] G. Rubinacci, A. Tamburrino, S. Ventre, "An efficient numerical model for a magnetic core eddy current probe", *IEEE Trans. on Magnetic*, vol. 44, pp. 1306-1309, 2008. 90

[94] R. Albanese, G. Rubinacci, F. Villone, "Crack simulation in the presence of linear ferromagnetic materials using an integral formulation", *Electromagnetic Nondestructive Evaluation (V), IOS press*, pp. 16-21, 2001. 90

[95] G. Rubinacci, A. Tamburrino, S. Ventre, and F. Villone, "Numerical modeling of volumetric cracks," *Int. J. Appl. Electromagn. Mech.*, vol. 19, pp. 345-349, 2004. 90, 97

[96] R. Albanese, G. Rubinacci, "Treatment of multiply connected regions in two component electric vector potential formulations", *IEEE Trans. Mag.*, Vol. 26, No. 2, 1990. 92

[97] G. Rubinacci, A. Tamburrino, S. Ventre, F. Villone, "Circuits/Fields Coupling and Multiply Connected Domains in Integral Formulations", *IEEE Trans. Mag.*, vol. 38, no. 2, pp. 581-584, 2002. 92